Bio-fluid engineering study in human and mammal respiratory system

Nguyen, Dang KHOA
九州大学総合理工学府環境エネルギー工学専攻

BIO-FLUID ENGINEERING STUDY IN HUMAN AND MAMMAL RESPIRATORY SYSTEM

A Thesis

by

Nguyen Dang KHOA

Supervisor

Prof. Kazuhide ITO

Master of Engineering

Building Environmental Engineering Laboratory

Department of Energy and Environmental Engineering

Interdisciplinary Graduate School of Engineering Sciences

Kyushu University

Fukuoka·Japan

August 2021

This page intentionally left blank

ACKNOWLEDGEMENTS

First of all, I would love to express my sincere gratitude to Prof. Kazuhide Ito, my supervisor, for his immense knowledge, helpful advice, and most importantly, his great support and belief in me during my two-year master's period. Without his guidance and suggestion, the completion of this thesis and all of my achievements would not have been reached. I also very much appreciate all of the precious time he spent on discussing, supervisory, and above all, reviewing and providing thoughtful comments that improve the results and the manuscript of this thesis. Besides, I am grateful for all the opportunities he offered me to gain experience and knowledge from the international conferences and the great opportunity to be a member of his research group.

My endless gratitude is also most respectfully sent to Dr. Nguyen Lu Phuong, my co-supervisor, for all his precious time for discussions and wonderful, timely support during the most challenging moments. This thesis would not be finished without his thoughtful review and enlightening commentaries. The experience, knowledge, and passion he has conveyed to me on the research journey are permanently imprinted in me. I always cherish all of his guidance since I was an undergraduate student when I spent my efforts to be a recipient of the MEXT (Ministry of Education, Culture, Sports, Science, and Technology – Japan) scholarship. I also would like to acknowledge my thankfulness to him for his support during my first time in Japan.

My sincere thanks to Assoc. Prof. Sung-Jun Yoo and Dr. Kazuki Kuga, for their comments and advice, helped me to improve my research results.

My master's program would not have been possible without the financial supports providing tuition and stipend by MEXT scholarship. I am very grateful for the valuable opportunity offered by the Japanese government.

My special thanks approve to my beloved family for their endless love, care, and encouragement

throughout my whole life. They have always believed, supported, and motivated me to continue my chosen journey in the most challenging times.

Last but not least, my profound thanks to Linh – my girlfriend, for her love, thoughtfulness, and sympathy during my master's program. Special thanks to all of my friends in my home country, Japan, and my lab members for their shares and the memorable time we have spent together.

ABSTRACT

The respiratory system is an air-conditioning system for humans and mammals, in which the ambient air is inhaled, filtered, and conditioned to achieve an appropriate status before entering the lungs. This function of the airway system can prevent the lungs from respiratory-related diseases, i.e., lung cancer, asthma, chronic obstructive pulmonary disease (COPD). Also, the airway system contributes as a ventilation system, which exchanges inhaled air (oxygen) and exhaled air (carbon dioxide). Due to the essential role of breathing patterns, the respiratory is the primary portal for foreign toxic substances to enter the human body. Besides, any deformation of the airway structure can consequently lead to a poor welfare life. Therefore, it is no exaggeration to state that the studies involving the fluid characteristics and pollutant/pathogen exposure in human and mammal airways have are essential. The computational Fluid Dynamics (CFD) technique has been widely adopted as the powerful method that applies numerical analysis and data structures to address the fluid flows in complex geometry, such as respiratory systems. Thus, in this thesis, the *in silico*-based CFD technique was applied to simulate the airflow characteristic and the ultrafine particle transportation/deposition in human and monkey airways. Furthermore, this study also applied the CFD method in the field of biomedical engineering, in which the effects of brachycephalic obstructive airway syndrome (BOAS) on the breathing function by quantitatively describing the airflow characteristics and airflow resistance in French bulldogs and examining the improvement of a postoperative bulldog to elucidate the efficacy of surgery.

The computational fluid dynamics (CFD) method was applied to analyze the steady flow rates under light and moderate conditions (Eulerian method); then, the discrete phase was tracked using the Lagrangian method. The ultrafine particles, ranging from 5 to 100 nm in diameter, were used to predict the total and regional deposition fraction in both models. The airflow distribution in the monkey airway model was found to vary from region to region, compared to the human airway model. A higher deposition efficiency was observed in the monkey model at the particle size of less than 25 nm.

Nonetheless, on applying the geometric factors for combined diffusion term parameters, the total deposition fraction of both models converged into a single curve. The site-specific deposition of the particles of size 5 nm in the vestibule, valve, and nasal turbinate regions of the monkey model was greater than the human model. A study of the deposition curves of the diameter of the particle ranging from 2 nm to 10 μm showed that the highest deposition rates were associated with particles of size 2 nm and 10 μm. The results of this study can contribute to the research involving extrapolation of inhalation toxicology studies, from monkeys to humans.

This study involved the CFD technique to simulate the effects of different stenosis intensities, i.e., open, mild, moderate, and severe, on airflow patterns in a total of eight French bulldog upper airways. A bulldog with severe stenosis after surgery was included to examine the efficacy of the surgical intervention. The upper airways of investigated French bulldogs were reconstructed based on the computed tomography (CT) images. The geometric features of 3D numerical models exhibited serious malformation of airway passages in moderately and severely affected bulldogs. The simulation results showed homogeneous airflow distributions in healthy and mild stenosis cases and due to the malformation of the airway, significantly accelerated airstreams at the constricted positions were observed in moderate and severe stenosis bulldogs. The airflow resistance was recorded to be over 20-fold greater in severe stenosis cases than the healthy cases. After surgery, a decrease in airflow velocity was observed in the surgical region, and the percentage of reduced airflow resistance was approximately 4% and 0.3% in light and moderate breathing, respectively. These findings suggest impaired breathing function in brachycephalic dogs with moderate and severe stenosis. The CFD quantitative results also contribute to surgery doctors' surgery plan-making and monitoring patient bulldogs' recuperation after surgery.

KEYWORDS: Computational fluid dynamics (CFD), Computed tomography (CT), Brachycephalic obstructive airway syndrome (BOAS), Ultrafine deposition, *In-silico* airway model, Human, Monkey, French bulldogs.

TABLE OF CONTENTS

LIST OF FIGURES

LIST OF TABLES

NOMENCLATURE

a	model coefficient
A	surface area
ACR	American college of radiology
A_i	the surface area of region i
A_{min}	minimum cross-sectional area
A_{noise}	root-square amplitude of noise
A_{signal}	root-square amplitude of signal
$ANOT$	adult-nasal-oral-tracheal
b	model coefficient
$BOAS$	brachycephalic obstructive airway syndrome
BPP	bits per pixel
$BWBP$	barometric whole-body plethysmography
BW	body weight
c	model coefficient
C	particle concentration
CAD	computer-aided diagnosis
C_c	Cunningham correction factor
C_D	drag coefficient
C_{dep}	number of particles deposited in the airways

C_{in} number of particles entering through the inlet of the airways

C_{RDi} number of particles deposited in region *i*

CFD computational fluid dynamics

CT computed tomography

CTK common toolkit

c_{μ} dependent parameter

D diffusion coefficient

d model coefficient

d_p particle diameter

dB *decibel*

DICOM digital imaging and communications in medicine

$d_{ij,}$ rate of the deformation tensor

D_k diffusion of *k*

DRW discrete random walk model

ET exercise test

F_B brownian force

F_D drag force

F_G gravitational force

F_S Saffman's lift force

f_{μ} damping functions

GUI	graphical user interface
I_0-I_n	Physical intensity
ITK	insight toolkit
k	turbulent kinetic energy
k_B	Stefan-Boltzmann constant
LSF	line spread function
MV	minute volume
MRI	magnetic resonance imaging
MPPD	multiple-path particle dosimetry
NA-MIC	national alliance for medical image computing
NEMA	national electrical manufacturers association
OTF	optical transfer function
m_p	particle mass
PACS	picture archiving and communication system
PEF	peal exhalation flow
PIF	peak inhalation flow
PIV	particle image velocimetry
p	particle phase
p_g	gas pressure
p'_g	fluctuating pressure
$\overline{p_g}$	mean pressure

P_k production of k

p_p particle penetration

Pr Prandtl number

P_{noise} level of noise

P_{signal} level of signal

PSF point spread function

Q inhalation flow rate

$RANS$ Reynolds-averaged Navier-Stokes

Re airflow Reynolds number

Re_p particle Reynolds number

RMS root mean square

S_f airway shape complexity

S_ϕ general source term

$SIMPLE$ semi-implicit method for pressure-linked equations

SNR signal-to-noise

STL stereolithography

t time

$TBFVL$ tidal breathing flow-volume loop

T_{air} temperature of the inhaled air

T_{wall} temperature of the inner wall of the airways

Te expiratory time

Ti	inspiratory time
$TRBV$	transient receptor potential vanilloid
u	instantaneous velocity
u'	fluctuating velocity
u_{p}	particle velocity
U	inlet air velocity
$\overline{U}$	mean velocity
V	entire model volume
$VGCC$	voltage-gated calcium channel
VTK	visualization toolkit
WSS	wall shear stress
y^+	dimensionless wall distance

Greek symbols

δ_{ij}	Kronecker delta
ε	turbulent dissipation rate
ω	specific dissipation rate
Δt	particle integration time step
λ	mean free path of the fluid
ν	kinematic viscosity
ν_T	eddy viscosity

μ	dynamic viscosity
η	deposition fraction
η_i	regional deposition fraction
ρ_g	gas density
ρ_p	particle density
π	pi constant (Archimedes' constant)
ζ	unit variance independent Gaussian random number
ϕ	fluid property
Γ_ϕ	diffusivity of the scalar
τ	particle relaxation time
τ_{ij}	Reynolds stresses

This page intentionally left blank

CHAPTER 1
BIO-FLUID ENGINEERING TOWARD HUMAN HEALTH AND VETERINARY SCIENCE

1.1. MOTIVATION

Air pollution is a major concern globally and has been revealed that has a close relation to the toxicological impacts on human health (Manisalidis et al. 2020). The respiratory tract is recognized as the predominant pathway for the airborne particles entering the human body. Airborne particulate matter, including dust, soot, smoke, and liquid droplet, is small enough to be suspended in the air. The particular matter particles are classified according to their aerodynamic diameter expressed in micrometer (μm), which consists of coarse (diameter < 10 μm), fine (diameter < 2.5 μm), and ultrafine particle or nanoparticle (diameter < 0.1 μm) (WHO 2006). The outdoor coarse particles normally come from natural sources such as evaporated sea spray, windborne pollen, dust, and volcanic eruptions. Meanwhile, the outdoor sources of fine and ultrafine particles can be attributed to the industry, combustion processes, and automobile emissions. Besides, ultrafine particles are also generated indoor as a consequence of cooking, indoor combustion, or smoking (Wallace 1996; Wallace 2006; Waring & Siegel 2007). Recent epidemiological studies indicate that exposure to particulate air pollution has been associated with an increased risk of lung cancer (Nikić & Stanković 2005), asthma, and chronic disease (Young et al. 2014; Kurt et al. 2016), as well as an increased risk of induced mortality and morbidity in humans (Manisalidis et al. 2020). Moreover, apart from the lung damage, the previous studies have revealed that the deposited ultrafine particles in the olfactory nerves can migrate to the brain through the blood-brain barrier (Oberdörster et al. 2004; Hopkins et al. 2014), which may cause neurodegeneration and brain injury (William Sunderman F. 2001; Calderón-Garcidueña et al. 2003).

Apart from human health, veterinary science has been attracting the attention of the public for the past decades. In modern society, pets such as cats or dogs are gradually becoming popular with humankind

and partly contribute to enriching the spiritual life of their owners. Like humans, respiratory diseases in pets are inevitable, restricting the proper breathing function, consequently lowering their welfare life. One well-known respiratory disease is the brachycephalic obstructive airway syndrome (BOAS), which is defined as a set of abnormalities, which is the most common congenital or known inherited airway disease (Harvey 1989) and is often detected in pug and bulldog breeds. Selective breeding for human-like features has resulted in the unintended deformation of the skull shape, where the skull length development is inversely proportional to the soft tissue, predisposing the breeds to airway obstruction (Aron & Crowe 1985). BOAS-affected dogs may exhibit symptoms including noisy and labored breathing (e.g., snoring and snorting), low blood oxygen concentration, regurgitation/vomiting, heat and exercise intolerance, cyanosis, collapse, and death (Hendricks 1992; Poncet et al. 2005; Packer et al. 2012; Haimel & Dupré 2015; Liu et al. 2015; Dupré & Heidenreich 2016; Ladlow et al. 2018). Stenosis nares is one of the primary BOAS-related abnormalities restricting the functional breathing of affected dogs, and severely affected BOAS dogs are required to experience surgery when the restrictive breathing exceeds acceptable levels (Lodato & Hedlund 2012b). The rhinoplasty treatment aims to increase the nostril opening area by removing the nasal wing and wing fold tissue. Recently, wedge shape resection of the external nostril with suture has become the standard surgery technique because of the good control of bleeding and the relatively good appearance of the surgical wounds. However, no investigations have quantified the specific improvement effect of the surgical operation for external nostril stenosis in brachycephalic dogs (Bernaerts et al. 2010).

Nowadays, computer modeling has been gradually becoming popular in the environmental engineering field. Furthermore, computational fluid dynamics (CFD) is a modeling tool that can provide us with detailed information on air movement, heat and mass transfer, and particle transportation with high accuracy in the enclosed space, as evidenced in previous articles (Ito, 2014; Ito et al., 2015a, 2015b; Ito et al., 2015c; Phuong et al., 2020; Phuong & Ito, 2013, 2015). In addition, medical imaging, which utilizes computed tomography (CT) and magnetic resonance imaging (MRI) images, can propose three-

dimensional numerical models to facilitate applying the CFD methods in bio-fluid engineering. In combining the two techniques (CFD and medical imaging methods), the *in silico* studies have enormous advantages for predicting the airflow characteristic and behavior of pollutants/pathogens in human and mammal respiratory systems due to their flexibility and lack of ethical constraints.

1.2. OBJECTIVES.

The main objectives of this thesis are to develop 3D numerical models of human and animal airways based on the CT images; then, the CFD method is applied to predict the airflow pattern, particle transportation, and deposition in human and mammal upper airway models. The two case studies were comprised in this study, the first one with the human and monkey airways and the second one with the French bulldog airway models.

The first objective – human and monkey airway models: the Eulerian method is applied to predict flow patterns in airway models under different breathing conditions. After analyzing the airflow, ultrafine particle behavior with different size ranges was simulated in the upper airway models by applying the Lagrangian method. The identical simulation processes were applied for both human and monkey airways to investigate the effects of intra-subjects variability on the deposition pattern. The total deposition in the upper airway was proposed to assess the adverse health effects of the ultrafine particle on human health. Meanwhile, the local deposition was identified to locate the preferred sites of the ultrafine particle in human airways.

The second objective – the French bulldog upper airway model: the 3D upper airway of BOAS-affected French bulldogs with different levels of stenosis were reconstructed. A bulldog with severe stenosis after surgery was also included to develop the post-surgery airway models to examine rhinoplasty efficacy. With the application of the CFD technique, the airflow characterizations were simulated to estimate to what extent of the nostril stenosis level that the patient bulldog needs to undergo surgery. The pressure drop and airflow resistance were calculated to show the degradation of breathing function in severe patient bulldogs and to examine the efficacy of the surgery.

1.3. ORGANIZATION OF THE THESIS

In chapter 1, the introduction section clarifies the research background and the objectives of this thesis. The adverse health effects of the long-term exposure to the toxic agents, such as particles under different breathing conditions, are briefly reviewed. Besides, the brachycephalic obstructive disease and its adverse impacts on affected dogs are introduced. The advantage of the CFD-based CT images method is also presented that facilitates the development of *in silico* studies.

In chapter 2, medical image processing is firstly introduced, and then the framework of reconstructing a 3D numerical model from CT data sets is described. After that, the explanation about the governing equations (i.e., Reynolds averaged Navier-Stokes-RANS), which is applied to characterize the airflow inside the upper airway models, was stated (Eulerian method). The transport equation of discrete phase modeling (Lagrangian method) is discussed, along with the properties of particles and the boundary conditions. The outline of 3D numerical of research subjects after the reconstruction is introduced and the detailed mesh design is presented

In chapter 3, the two upper airway models, e.g., human and monkey upper airway models, were included by applying the aforementioned methodology. Firstly, the Eulerian method was applied to simulate the airflow patterns in the upper airway models, then the trajectories of ultrafine particles (diameter ranging from 5-100 nm) were tracked using the Lagrangian method. The discrepancies in airflow distribution between monkey and human airways were characterized. The results of ultrafine particle transportation and deposition in human and monkey airways were obtained and discussed. The impacts of Brownian motion on the acceleration/de-acceleration of ultrafine particles were demonstrated. Next, the total predicted deposition results were compared with previous experimental data to confirm the accuracy. While the quantitative and visualized results of regional deposition were presented. Finally, the deposition curve of the particle from ultrafine to fine particles was recorded and presented in this chapter.

In chapter 4, the upper airway models of eight French bulldogs with different nostrils stenosis were reconstructed based on the CT images. A specific patient with severe stenosis bulldog underwent surgery,

and the post-surgery case was established to examine the efficacy of the surgical intervention. The deformation of airway structure due to the BOAS-disease was compared and discussed. The airflow features in individual upper airway was depicted, and the impacts of nostril stenosis levels on the inhaled airstream were discussed for light and moderate breathing conditions. After that, the pressure drop and airflow resistance were calculated to evaluate the severity of impaired breathing function of severe stenosis bulldogs and to examine the efficacy of the surgery.

The conclusion chapter (Chapter 5) of this thesis will summarize the significant results of each project in Chapters 3 to 4. The limitations of the thesis are clarified, and the final parts of this chapter highlight the potential contribution of this study and provide recommendations for further study.

CHAPTER 2
MEDICAL IMAGE PROCESSING AND NUMERICAL SIMULATION METHODOLOGIES

2.1. INTRODUCTION TO DIGITAL IMAGE

A digital image is defined as a set of rectangular grid points or pixels covered by a gray value (i.e., brightness) or a color (i.e., hue, saturation, and brightness) (Suetens 2009). Quantization is the conversion process from analog samples to discrete-valued samples, and this process directly impacts the observational experience of the image. Within the few gray values, the contouring appears in the figure (as shown in Fig 2.1). This characteristic raises concerns about appropriate gray values are required to produce a continuous-looking image. The simple assumption is that n+1 gray values are displayed corresponding to physical intensities I_0, I_1,…, I_n; in which I_0 and I_n are the minimum and maximum intensity, respectively. The ratio between I_n/I_0 is known as the dynamic range, and the range of 100 the required number of gray values is 463, and the dynamic range of 1,000 needs 694 gray values. Nowadays, most digital images are produced with 4,096 gray values (12bpp).

The term histogram, which contains much information about an image, is a probability distribution on the set of possible gray values. The probability of a gray value *v* is given by its relative frequency in the image, that is,

$$h(v) = \frac{\text{number of pixels having gray value v}}{\text{total number of pixels}} \tag{2.1}$$

The quality of a digital image can be specified based on four factors: resolution, contrast, noise, and artifacts. The imaging processing determines the resolution; the more blurring, the lower is the resolution. The resolution can be affected by (1) the characteristic of the imaging system, (2) the scene characteristics and geometry, and (3) the viewing conditions. In other words, the resolution is also defined as how a small, bright point on a dark background is smoothed after the imaging process. Obviously, the small, bright point will not be sharp as itself; instead, the smoothed blob is generated and

so-called point spread function (PSF), as shown in Fig 2.2. If the resolution is the same in all directions, the line spread function (LSF) may be more practical than PSF. Another form of resolution is the optical transfer function (OTF), which is the Fourier transform of the PSF and LSF.

Contrast is defined as the difference in intensity of adjacent regions of the image; in other words, it is the amplitude of the Fourier transform of the image as a function of spatial frequency. The contrast is influenced by the identical factors to the resolution (imaging process, scene characteristic, and viewing conditions).

Next is the noise of an image, which always appears as the statistical nature of imaging. Noise can eliminate the valuable information of an image if the level itself is sufficiently high. An important measure is a signal-to-noise (SNR or S/N) that compares the desired signal level to the level of background noise expressed at decibels.

$$SNR = \frac{P_{signal}}{P_{noise}} = \left(\frac{A_{signal}}{A_{noise}} \right)^2 \tag{2.2}$$

where A is the root-square amplitude. It can also be addressed as a logarithmic scale:

$$SNR = 10\log_{10}\left(\frac{P_{signal}}{P_{noise}} \right) = 20\log 10\left(\frac{A_{signal}}{A_{noise}} \right) \tag{2.3}$$

A higher ratio than 1:1 denotes more signal than noise; for example, 60 dB means that the root-square amplitude if the signal is 1,000-fold that of noise. An estimate of the noise can be obtained by making a flat-field image, which is an image without an object between the source and the detector. The noise amplitude as a function of spatial frequency can be calculated from the square root of the so-called Wiener spectrum (or noise power spectrum).

Finally, artifacts are artificial features such as dust or scratches in an image; for example, a metal streak artifact in computed tomography (CT) or geometric distortions in magnetic resonance (MR) images. This factor may also be induced during the imaging process, consequently hampering accurate diagnosis

and measurements. These four factors mentioned above are dependent on the imaging modalities; however, this issue is far from the interesting field of this study; therefore, it will not be discussed herein.

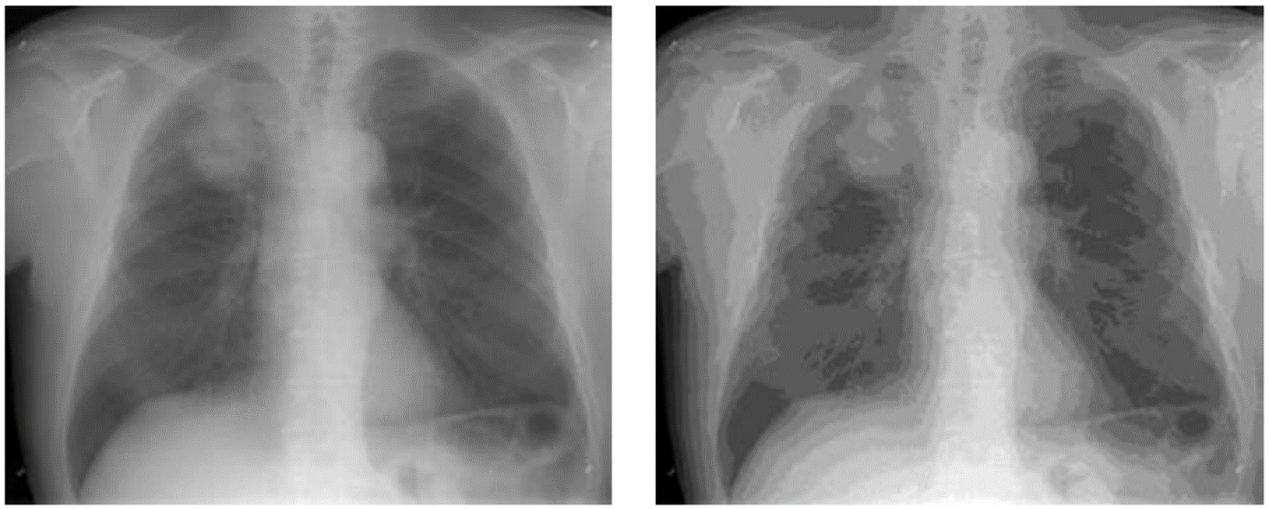

(a) (b)

Figure 2.1: The identical image was quantized with (a) 8 bpp and (b) 4 bpp.

Source: (Suetens 2009)

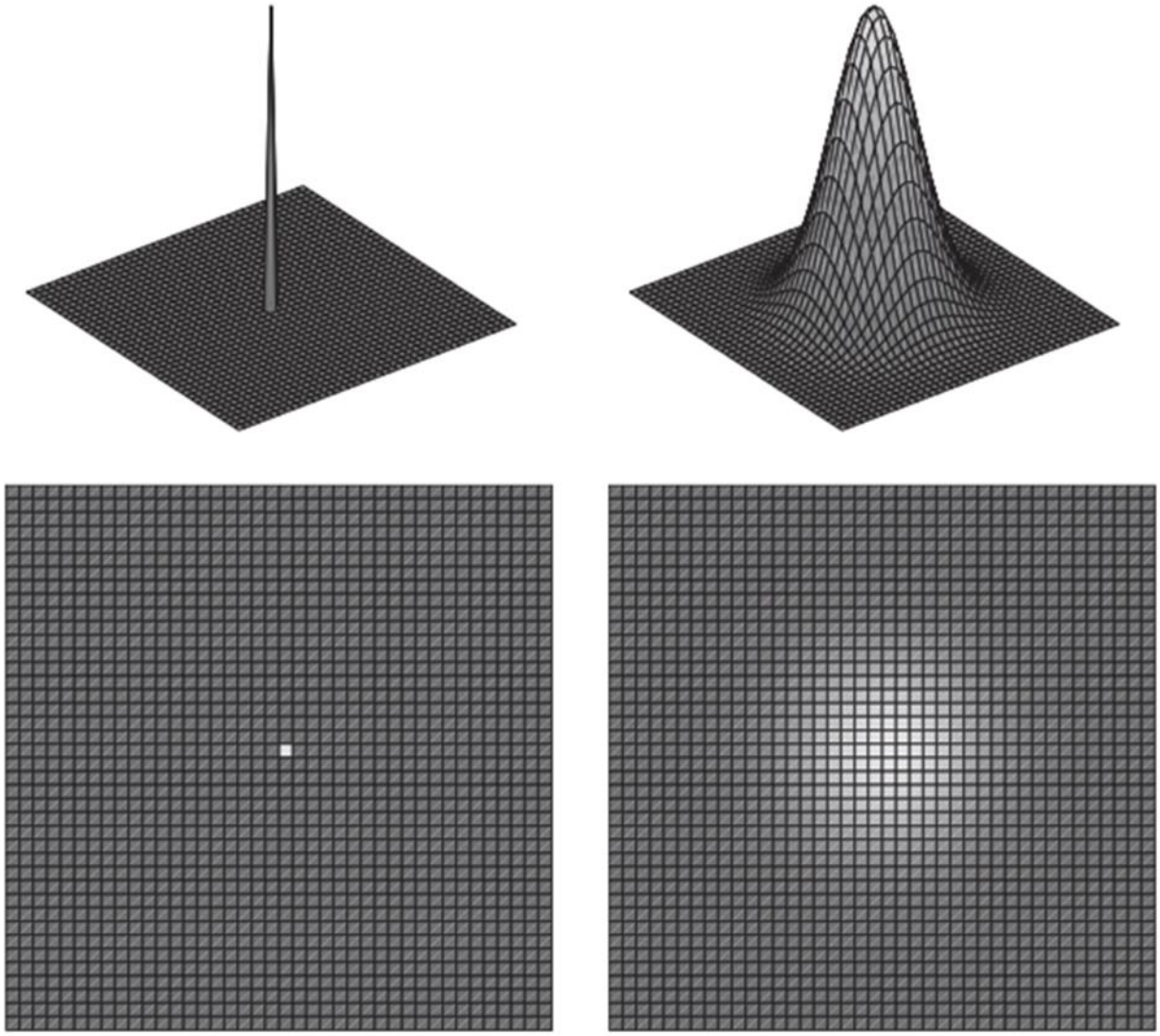

(a) (b)

Figure 2.2: (a) The sharp, bright spot on a dark background and (b) the smoothed blob as the point spread function (PSF).

Source: (Suetens 2009)

2.2. MEDICAL IMAGE PROCESSING

Medical image processing refers to the several available techniques used to discover the inside view of living organisms such as humans, primates, or dogs. Moreover, each type of technology delivers different information about the interesting part being studied or treated, relating to the disease, injury, or the effectiveness of medical treatment (Bakhtiary 2014). These techniques, including the X-ray and Ultrasound imaging invented in the early 20^{th} century, and another two are Computed tomography (CT) and Magnetic resonance imaging (MRI), developed in the late last century, are still utilized today.

2.2.1. Computed tomography (CT)

Computed tomography (CT), which was first developed in 1972 by Godfrey Hounsfield, applies x-rays to create a series of planar cross-sectional images along an axis. During the CT procedure, the patient is placed on a table and then moved to a supine position through a rotating gantry. Multiple x-rays are taken in the region of interest along the patient's body and form the cross-sectional slices. The detector collects the x-ray information and transfers them to a computer that combines them into a single image. There are three different CT scanners, including conventional scanners, spiral scanners, and multi-slice scanners (Fig 2.3). The multi-slice scanner can provide 2D cross-sectional slices, representing a 3D body structure instead of individual 2D images in the conventional scanner.

Meanwhile, the spiral scanner provides quick scans, which are suitable for the procedure requiring quickness, such as the lung, which must be scanned with the patient in one position and within one breath-hold. The set of CT images can be described into various planes of view (sagittal, coronal, and transverse), as shown in Fig 2.4. Notice the difference in the body planes of a four-legged animal and a human.

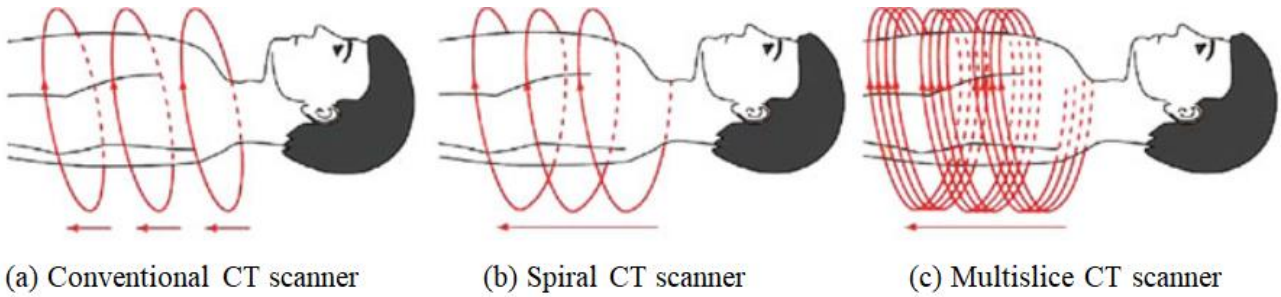

Figure 2.3. Three different types of CT scanners.

Source: (Tu et al. 2013)

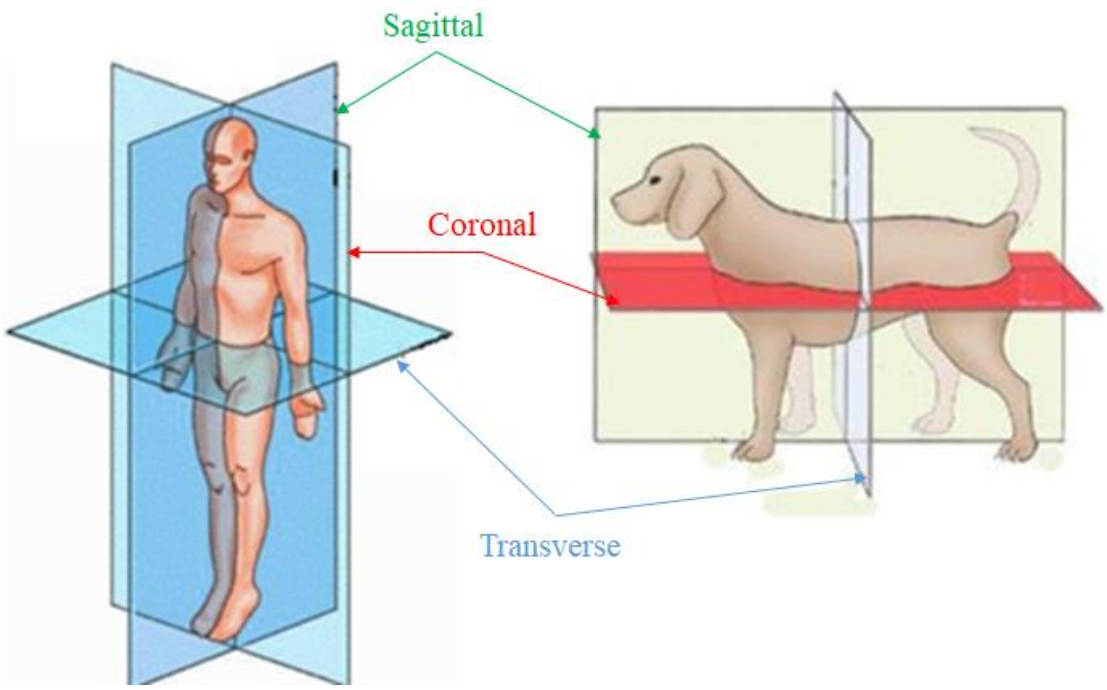

Figure 2.4: The three-plane of views in the body of a human and four-legged animal.

(*Source: Internet)*

2.2.2. Magnetic resonance imaging (MRI)

In contrast with CT, magnetic resonance imaging (MRI) utilizing magnetic fields and radio waves to distribute the hydrogen protons, which are contained in the water covering most of the human body. Based on the distribution of hydrogen protons, cross-sectional images of the human body can be obtained. An MRI scanner consists of a movable table that slides into a large cylinder. Herein, the larger superconducting magnet, made up of many wire coils, will create a magnetic field when the electric current passes through the coils. Then the hydrogen protons that usually spin in random directions will align with the magnetic field gyrating in its position. After that, a short burst of radio waves is sent through that changes the quantum state of the protons. When the radio waves stop, the protons return to their original position; and during this process, their signal will be detected and deciphered into images. In comparison, following the medical imaging point of view, the MRI technique offers much greater detail in soft tissues and can highlight different tissues; meanwhile, CT images produce better detection of bone structure.

2.2.3. Medical imaging technique

Imaging systems generate an output (image) based on the input (signals) arising from different properties of a human body and resulting in the images. Medical imaging comprises specified components such as image acquisition from patients (by using the imaging modalities as discussed above), image processing, image display, image recording and storage, image transmission, and image interpretation, which are primarily included in a picture archiving and communication system (PACS) (Doi 2006). The universal format that supports a PACS is well-known as DICOM (Digital imaging and communications in medicine), which was developed by the cooperation of the American College of Radiology (ACR) and the National Electrical Manufacturers Association (NEMA) in 1983 (Mildenberger et al. 2002). Among the components of the medical imaging process, the image interpretation has been recognized as an essential process in the term of diagnosis and decision making. For assisting this process, computerized analysis of medical images has recently been implemented clinically for detecting the abnormalities or

lesions; this is so-called the computer-aided diagnosis (CAD) involving image processing (Doi 2006).

Furthermore, the vast development of computer resources has facilitated medical image processing in 3D view, allowing radiologists and biomedical engineering researchers to access the detailed anatomy and abnormalities more easily. Therefore, to meet the demand, open-source software applications have been presented as promising alternatives for conventional software that is not always affordable to academic researchers. Among them, the Osirix lite and 3D Slicer are widely adopted in the radiology community (Mujika et al. 2018); however, as also revealed in the previous works (Fedorov et al. 2012; Mujika et al. 2018), the free usage of Osirix lite is limited, and the upgrade to the licensed version is required to explore the restrictive function. Therefore, the 3D Slicer software was determined as the priority tool for image processing in this study.

3D Slicer is a free, open-source software and multi-platform software package widely used for medical, biomedical, and related imaging research (https://www.slicer.org/). In recent years, 3D Slicer has been emerging as a powerful visualization tool allowing exploration of medical image data in two or three dimensions, which is critical at the initial stage of medical image processing. The structure of 3D Slicer obeys a modular and layered approach, as detailed explained in the previous paper (Fedorov et al. 2012); herein, its structure is briefly presented. The structure is divided into three levels, as shown in Fig 2.5; the bottom level contains the fundamental libraries provided by the operating system. This platform is not associated with Slicer; therefore, enhancing the usage of windowing and graphics resources of the user system. The middle comprises the programming languages (C++, Python) and the libraries that provide the higher level functionally and abstractions (Qt-cross platform graphical user interface framework and DICOM Toolkit-DCMTK). Other libraries are parts of the National Alliance for Medical Image Computing (NA-MIC), a collection of software tools. CMake enables cross-platform build system configuration, packaging, and test of 3D Slicer. The Visualization Toolkit (VTK) provides 3D computer graphics and visualization functions. The Insight Toolkit (ITK) delivers medical image registration and segmentation. The Common Toolkit (CTK) is a biomedical image computing library focusing on

application-level DICOM support, plug-in framework, and specialized GUI (graphical user interface) widgets. At the top level, 3D Slicer itself possesses the core, modules, and extensions, in which the core controls the GUI, supports the input/output data and visualization. The extension is a plug-in function allowing the integration of the new functionality that satisfied the research requirements and demands.

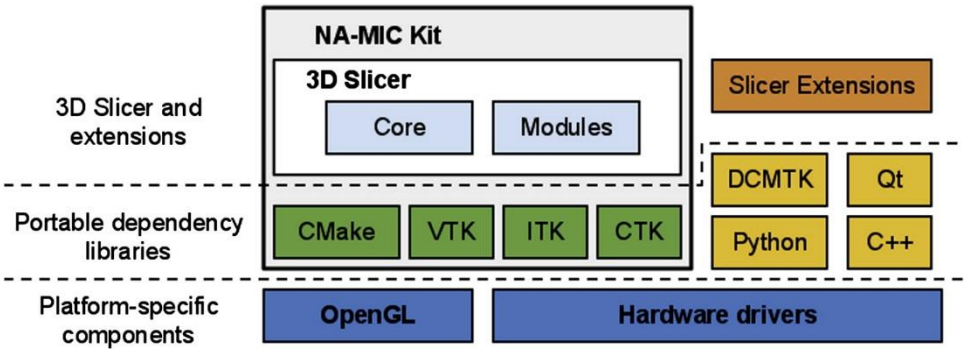

Figure 2.5: The structure of 3D Slicer software.

Source: (Fedorov et al. 2012)

In this thesis, the 3D slicer software was applied to perform the segmentation process mainly. This process can be explained as the partitioning of an image into meaningful regions, mainly distinguish regions of interest (foreground) from the surroundings (background) (Dougherty 2009). Segmentation is widely used to detect organs such as the brain, heart, lungs, tumor, and in this thesis, it is the upper airway of humans and mammals. The process of generating a 3D numerical airway model in 3D Slicer is straightforward. Firstly, the 3D Slicer can be freely downloaded and installed from the homepage (https://www.slicer.org/). The medical image data sets, which were transformed to DICOM format, can be directly loaded into the GUI, and the three different 2D views, including transverse, sagittal, and coronal, are displayed (Fig 2.6). The "Volume rendering" tool facilitates the 3D visualization originated from the 2D images; herein, the preset types can be actively selected to create the purpose-related 3D image, which is shown in the remaining panel (Fig 2.7). The 3D Slicer also enables the use of gray-level transformations; in which, for a given digital image distributing a gray value to each of the pixels (i, j),

and the gray value transformations is a function *g* that converts each gray value I(*i, j*) to another value I'(*i ,j*). Hence, for all pixels (*i, j*).

$$I'(i,j) = g\left(I(i,j)\right) \tag{2.4}$$

The main use of this function is to increase the contrast in some regions of the image, consequently highlighting the region of interest. For example, in this study, the interesting region is the upper airway of a bulldog; therefore, the gray value transformation was applied to explicitly describe this region (black area), as shown in Fig 2.8. Then the segmentation process is initialized with the "Editor" function that provides the various available methods to precisely extract the desired morphometric properties and geometric features from the medical image. The simplest method is the low-level method relying on the local image operator and a heuristic grouping of pixels with similar local photometric characteristics. The two tools of this method are available in 3D Slicer software, including the region growing and edge detection. Basically, these two tools are similar, but region growing partitions an image into regions by grouping the adjacent pixels with similar gray values, thus creating boundaries between contrast regions.

Meanwhile, edge detection applies the linking or tracking boundary points, which can be found by a local differential operator, i.e., the gradient or Laplacian. Due to the user-friendly characteristics, these two methods are widely applied in most commercial and non-commercial image analysis tools. However, they can only show the usefulness in analyzing the simple image data rather than the complex image data, such as medical images; therefore, they are not utilized in this study.

The more sophisticated methods, so-called model-based methods, are also integrated into the 3D Slicer to segment the complex image data, and these methods require prior knowledge about the geometry and photometry of the concerned region structure. Among them, thresholding, the most straightforward segmentation algorithm based on the greyscale levels of pixels, is most effective for images containing uniform regions with clear differentiation from a background or other objects in terms of pixel intensity values (Tu et al. 2013). This tool requires the apparent boundaries of each region in the 2D feature space;

therefore, few structures in the medical image can satisfy this condition despite its wide application. However, this method is robust in segmenting the bony structure in the CT images. Following the CT images, the upper airway is surrounded by a bony structure; thus, the delineation of bony structure around the upper airway region can facilitate the segmentation of this region, as described in Fig 2.9. Therefore, this tool was applied in this study to extract the upper airway region.

Once the digital model of the preferred structure has been generated, the user can then save the model into stereolithography (STL) format, which can be used for further processes such as 3D printing or clinical investigations. Despite the straightforward and user-friendly interface of 3D Slicer, the medical imaging process must be carried out by radiologists who specialize in diagnosing and treating injuries using medical imaging procedures (Mujika et al. 2018). Therefore, to offer better accessibility to the clinical information of medical images, the medical image-based computational fluid dynamics (CFD) method has been extensively applied in clinical research, biomedical engineering, and others.

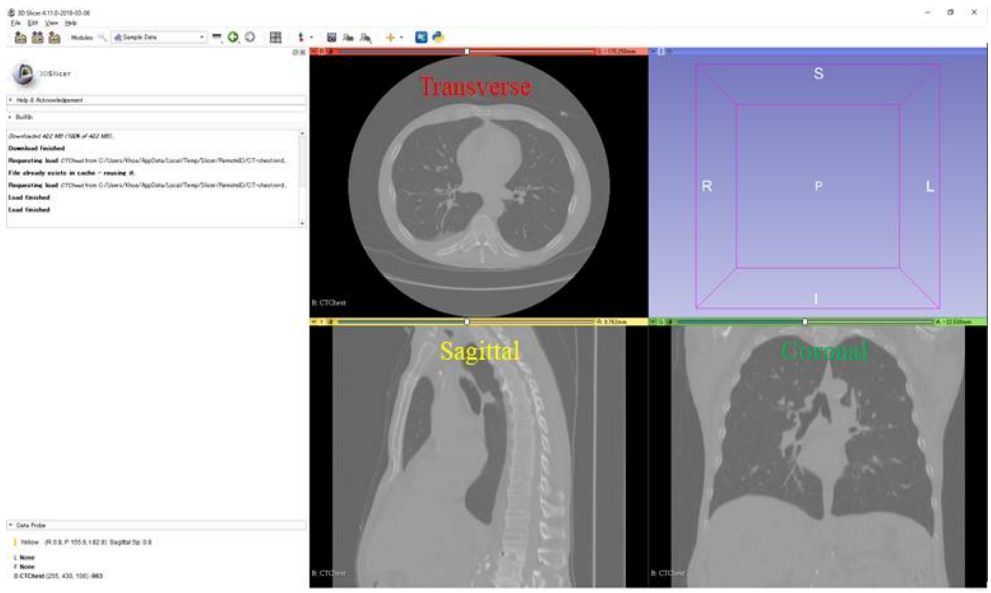

Figure 2.6: The graphic user interface of 3D Slicer software after loading the medical images.

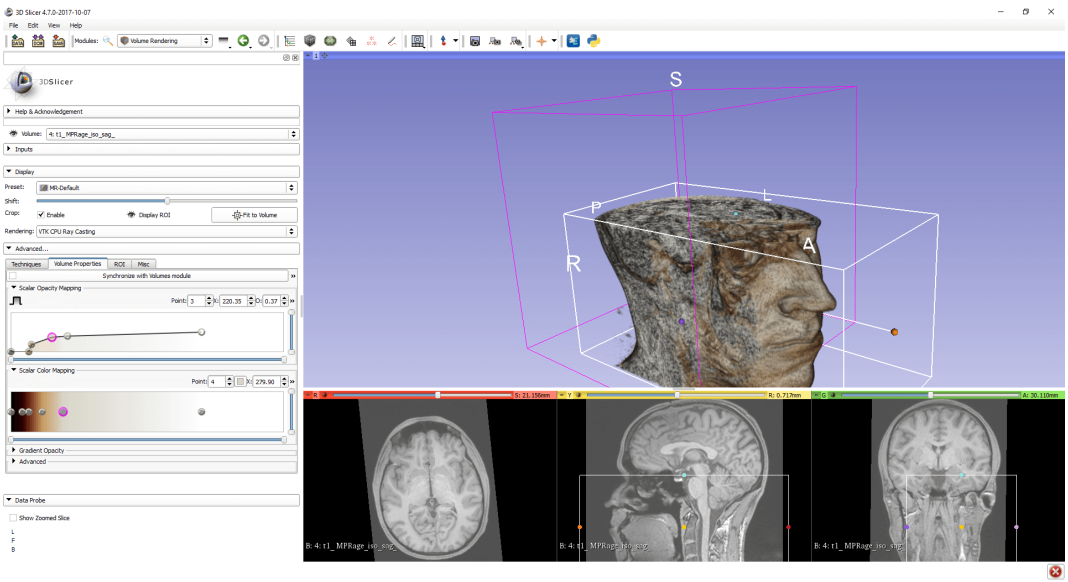

Figure 2.7: The 3D view is producing by the Volume rendering function based on the set of 2D images. Herein describes the example of a human head.

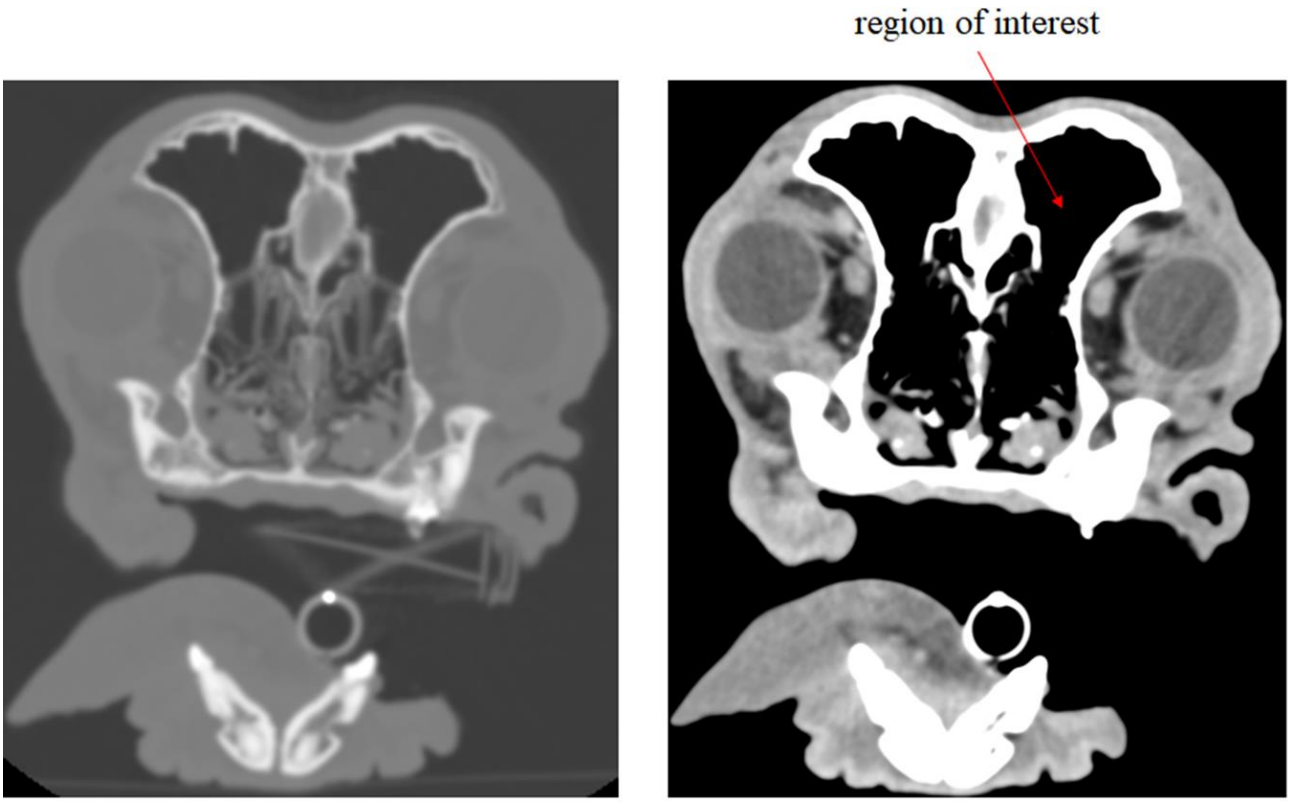

(a) (b)

Figure 2.8: (a) The original CT image of a bulldog, (b) the transformed CT image offered by the gray value transformation function of 3D Slicer.

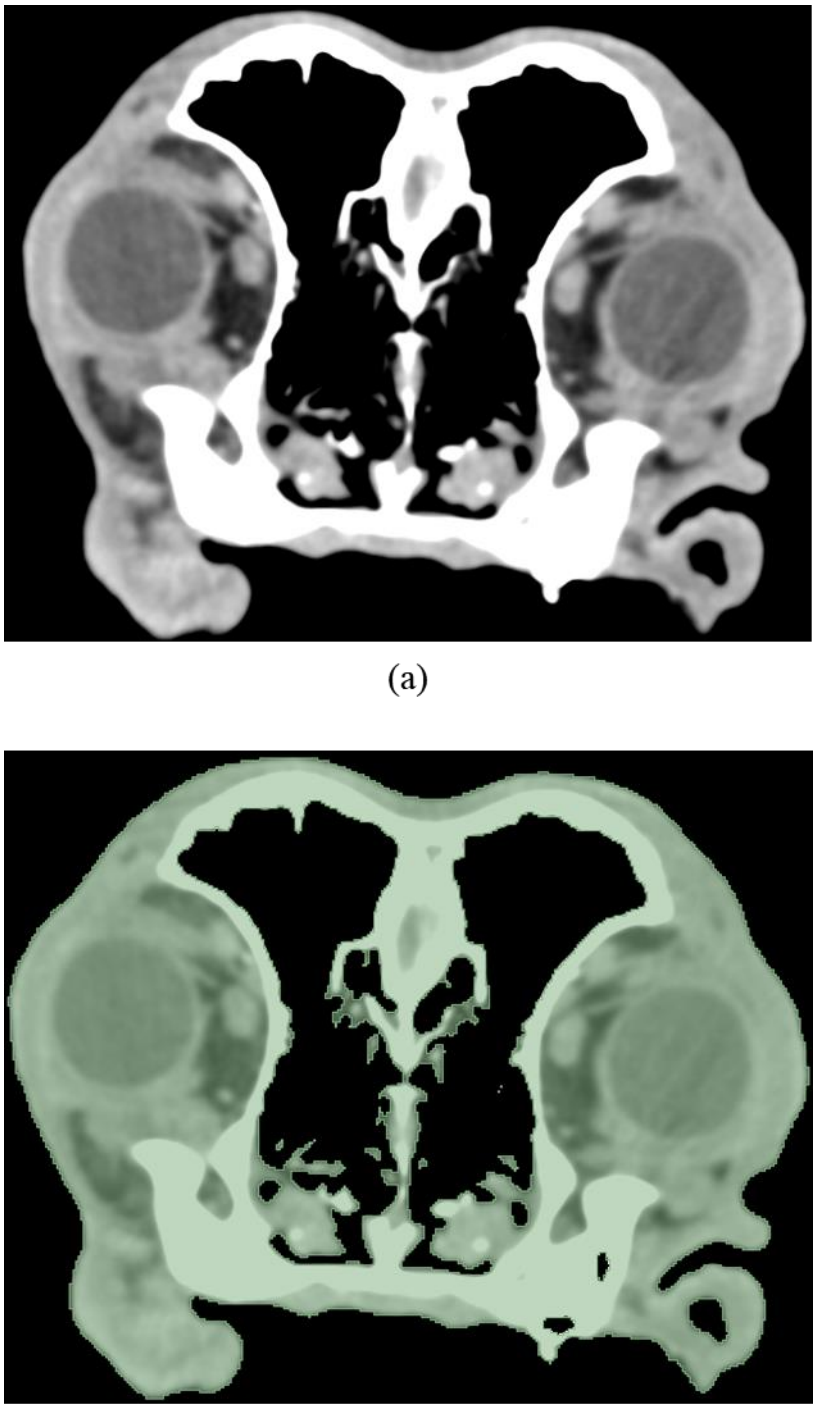

(a)

(b)

Figure 2.9: (a) The original CT image of a bulldog, (b) Result with a threshold range from -116 to 2,026. The bony structure and the region outside are represented in the green color, and the region of interest (upper airway) can be separated.

2.3. COMPUTATIONAL FLUID DYNAMICS (CFD)

2.3.1. Gas-phase modeling

Computational fluid dynamics (CFD) is the analysis system involving the fluid flow, heat transfer, and associated phenomena such as chemical substances transportation and reactions employing computer-based simulation (Versteeg & Malalasekera 2007). CFD is based on the vital governing equations of fluid mechanics and thermal sciences, including continuity equations, Navier-Stokes equations, and energy equations (Wah-Yen et al. 2017).

The airflow in the respiratory system is regarded as a continuum where the effects on a molecular scale may be ignored. The characteristic of the air is then described by velocity, pressure, density, temperature, space, and time derivatives. For a general fluid property defined by ϕ, the governing equations of fluid flow for an incompressible fluid, such as the airflow in the respiratory system, can be cast into the so-called transport equation form as:

$$\frac{\partial(\rho_g \phi)}{\partial t} + \frac{\partial(\rho_g \phi u)}{\partial x_j} = \frac{\partial}{\partial x_j}(\Gamma_\phi \frac{\partial \phi}{\partial x_j}) + S_\phi \tag{2.5}$$

where t is time, ρ_g denotes the gas density, u represents gas velocity, Γ_ϕ is the diffusivity of the scalar, S_ϕ is a general source term. The first and second terms on the left-hand side in Equation (2.5) describe the local acceleration and advection. On the right-hand side, the third term is the diffusion term, and the remaining one is the source term that may represent external variables. The source terms may include pressure and non-pressure gradient terms, which influence the fluid motion and heat sources or sinks within the flow domain.

Equations 2.6, 2.7, 2.8 lists the set of governing equations for incompressible fluid flow. These conservation laws of physics governing fluid flow behavior include continuity equation (conservation of mass), the balance of momentum (Newton's second law, the rate of change of momentum equals the sum of forces acting on the fluid), and the energy equation (first law of thermodynamics, the rate of

change of energy equals the sum of the rate of heat addition to, and the rate of work done on, the fluid).

Continuity equation for incompressible flow (ϕ=1):

$$\frac{\partial(\rho_g u_i)}{\partial x_i} = 0 \tag{2.6}$$

Momentum equation (ϕ=u):

$$\frac{\partial(\rho_g u_i)}{\partial t} + \frac{\partial(\rho_g u_i u_j)}{\partial x_j} = -\frac{\partial p_g}{\partial x_i} + \frac{\partial}{\partial x_j}\left(\mu_g \frac{\partial u_i}{\partial x_j}\right) \tag{2.7}$$

Energy equation (ϕ=T):

$$\frac{\partial(\rho_g T_g)}{\partial t} + \frac{\partial(\rho_g u_j T_g)}{\partial x_j} = \frac{\partial}{\partial x_j}\left(\frac{\mu_g}{\mathrm{Pr}} \frac{\partial T_g}{\partial x_j}\right) \tag{2.8}$$

The fluid behavior can be characterized in terms of the fluid properties velocity vector u (with components u, v, and w in the x, y, and z directions), pressure (p_g), density (ρ_g), viscosity (μ_g), Prandtl number (Pr) and temperature (T_g). The changes in these fluid properties can occur over space and time.

The Eulerian approach analyzed flow fields, and a finite-volume-based commercial CFD code discretized the Navier-Stokes governing equations. The numerical modeling of the airflow through the respiratory tracts of humans and animals involves the solution of the Navier–Stokes equations, which are based on the assumptions of conservation of mass and momentum within a moving fluid. In nature, most of the flow characteristics are recognized as turbulent, and the turbulent-flow calculation attempts to solve a number of partial differential equations based on the exact Navier-Stokes equation. The starting point is the Reynolds decomposition of the flow variables in the Navier-Stokes equation into mean and fluctuating parts, which is followed by an averaging of the equations themselves and then gives rise to the new Equation so-called Reynolds-averaged Navier-Stokes (RANS) equation.

In Fig 2.10, there are a series of fluctuations occurring in a turbulent flow. The fluctuations are due to turbulent motions, which create intense mixing and momentum exchange that causes acceleration of

slower-moving layers and deceleration of faster-moving layers.

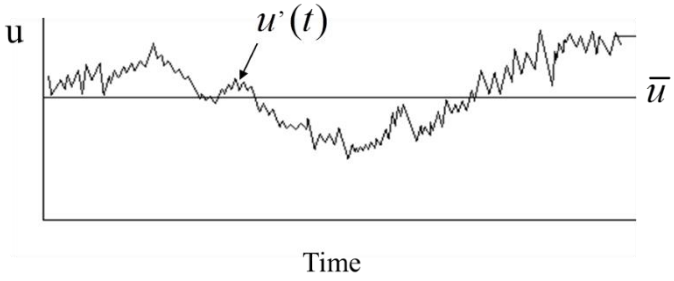

Figure 2.10: Velocity fluctuating at a given time.

The fluctuating velocity fields are the characteristics of the turbulent flows, resulting in fluctuations for transported quantities of momentum, energy, and species concentrations. The fluctuations can be of small scale and high frequency; they are computationally expensive to simulate directly in practical calculations. Therefore, time-averaged properties of the flow are typically used for making calculations. In this case, velocity is characterized using the time-averaged value for velocity *u*, expressed as a mean component $\overline{U}$, while the fluctuating component is expressed as u'. However, in turbulent flow, the other flow properties (i.e., pressure, temperature, density, other velocity components, etc.) also have fluctuations. Therefore, the variables can be decomposed as a steady mean component and fluctuating parts as below:

$$u_i = \overline{U}_i + u_i' \tag{2.9}$$

$$u_j = \overline{U}_j + u_j' \tag{2.10}$$

$$p_g = \overline{p_g} + p_g' \tag{2.11}$$

Substituting the decomposed variables into the continuity and Navier-Stokes equation (Equations 2.6 and 2.7) yields:

$$\frac{\partial(\overline{U}_i + u_i^{'})}{\partial x_i} = 0 \tag{2.12}$$

$$\frac{\partial\left(\overline{U}_i + u_i^{'}\right)}{\partial t} + \frac{\partial}{\partial x_j}\left[\left(\overline{U}_i + u_i^{'}\right)\left(\overline{U}_j + u_j^{'}\right)\right] = -\frac{1}{\rho_g}\frac{\partial\left(\overline{p_g} + p_g^{'}\right)}{\partial x_i} + \nu\frac{\partial^2\left(\overline{U}_i + u_i^{'}\right)}{\partial x_j{}^2} \tag{2.13}$$

Taking the Reynolds averaging for Equations 2.12 and 2.13; and obeying the rules of Reynolds averaging we can obtain RANS equations:

$$\frac{\partial\overline{U}_i}{\partial x_i} = 0 \tag{2.14}$$

$$\frac{\partial\overline{U_i}}{\partial t} + \frac{\partial}{\partial x_j}\left(\overline{U_i}\,\overline{U_j}\right) = -\frac{1}{\rho_g}\frac{\partial\overline{p_g}}{\partial x_i} + \nu\frac{\partial^2\overline{U}_i}{\partial x_j{}^2} - \frac{\partial}{\partial x_j}\left(\overline{u_i^{'}u_j^{'}}\right) \tag{2.15}$$

The appearance of the new term, so-called Reynolds stresses $\tau_{ij} = \overline{u'_i\, u'_j}$, states the closure problem to the RANS equation. Therefore, the RANS equation can be solved if the unknown Reynolds stresses are modeled.

Boussinesq (well-known as Boussinesq approximation) introduced the earliest and simplest turbulent model, which suggested that the Reynolds stresses are proportional to the mean rates of deformation, similar to how viscous stress is related to the deformation rate. That is,

$$\tau_{ij} = \frac{2}{3}k\delta_{ij} - \nu_T\left(\frac{\partial\overline{U}_i}{\partial x_j} + \frac{\partial\overline{U_j}}{\partial x_i}\right) \tag{2.16}$$

where k is average kinetic energy; the Kronecker delta, δ_{ij}, has its standard definition, i.e., equal to 0 when i ≠ j, equal to 1 when i = j, and eddy viscosity ν_T.

In fact, there is no universal turbulence model accepted predicting for all kinds of problems. Instead, the choice of turbulence model depends on considerations such as the physics encompassed in the flow, the established practice for a specific class of problem, the level of accuracy required, the available

computational resources, and the amount of time available for the simulation.

Among the linear eddy-viscosity models, the *k-ε* family has been evidenced to have better agreement with experimental data than the *k-ω* family in the swirling pipe-flow (Díaz & Hinz 2015). The general problem of the standard *k-ε* model is the near-wall treatment; therefore, it is inconsonant with the purpose of this study. Another RANS turbulence model, i.e., the Low Reynolds $k-\varepsilon$ proposed by Abe et al. (Abe et al. 1994; Abe et al. 1995) introduced the damping functions of this model introduce the Kolmogorov velocity instead of friction velocity as the velocity scale to account for the near-wall and low-Reynolds number effects. In addition, the Low Reynolds $k-\varepsilon$ proposed by Abe et al. has been adopted to achieve the high accurate prediction of heat transfer in the turbulent flow by avoiding the assumption of constant Prandtl number. Besides, the target flow in upper airway models is relatively low Reynolds numbers and within the flow regime from laminar to transitional. The previous study has evidenced the relatively accurate results in human and monkey airways compared with experimental data using the Low Reynolds $k-\varepsilon$ (Abe Kondoh Nagano) model (Phuong & Ito 2015; Phuong et al. 2020). Therefore, the Low Reynolds type $k-\varepsilon$ model was adopted to predict airflow in human and animal respiratory systems.

The models are extended from the high-Reynolds-number model by introducing various wall damping functions expressed in terms of the turbulent Reynolds number and the normal wall distance. Based on the Boussinesq approximation, the Reynolds stress is related to the local velocity gradients by an eddy viscosity ν_T.

$$\nu_T = C_\mu \times f_\mu \times \frac{k^2}{\varepsilon} \tag{2.17}$$

where *k* is the turbulent kinetic energy, ε is the dissipation rate, f_μ is damping functions in velocity field turbulence model, and c_μ is a parameter that depends on the *k-ε* turbulence model.

Transport Equation for k

Here, the turbulent kinetic energy for three dimensional flows is given by:

$$k = \frac{1}{2}\left(\overline{u'}_i \cdot \overline{u'}_i\right) \tag{2.18}$$

The Equation for turbulent kinetic energy k is obtained by multiplying the Navier-Stokes equations (Equation 2.7) with u'_i and performing the decomposition. Then taking the Reynolds averaging and following the rules of Reynolds averaging yields. Finally, introducing the transformation as $\overline{u_i' \frac{\partial u_i'}{\partial x_j}} = \frac{\partial\left(\frac{1}{2}\overline{u_i' u_i'}\right)}{\partial x_j} = \frac{\partial k}{\partial x_j}$ we achieve the transport equation of k:

$$\frac{\partial k}{\partial t} + \overline{U}_j \frac{\partial k}{\partial t} = -\overline{u_i' u_j'} \frac{\partial \overline{U}_i}{\partial x_j} - \frac{\partial}{\partial x_j}\left(\frac{\overline{p_g' u_i'}}{\rho_g} + \frac{1}{2}\overline{u_i' u_i' u_j'}\right) + \nu \overline{u_i' \frac{\partial^2 u_i'}{\partial x_j^2}} \tag{2.19}$$

The first term on the right side of Equation 2.19 denotes the production of k $\left(P_k\right)$, and the second term is interpreted as the diffusion of $k\left(D_k\right)$, and the last term is the effect of the molecular viscosity$\left(\nu_k\right)$. Thus, by applying the complex mathematical transformation, we finally achieve the transport equation of k.

$$\frac{\partial k}{\partial t} + \overline{U}_j \frac{\partial k}{\partial t} = \nu_T \left(\frac{\partial \overline{U}_i}{\partial x_j} + \frac{\partial \overline{U}_j}{\partial x_i}\right)\frac{\partial \overline{U}_i}{\partial x_j} + \frac{\partial}{\partial x_j}\left[\left(\frac{\nu_T}{\sigma_k} + \nu\right)\frac{\partial k}{\partial x_j}\right] - \varepsilon \tag{2.20}$$

In the Equation 2.20, ε is defined as the dissipation rate of the turbulent kinetic energy.

Transport Equation for ε

The dissipation of turbulent kinetic energy is defined as $\varepsilon = \nu \overline{\frac{\partial u_i'}{\partial x_j}\frac{\partial u_i'}{\partial x_j}}$. Applying the operator $\nu \frac{\partial u_i'}{\partial x_j}\frac{\partial}{\partial x_j}$ to the Navier-Stokes equation and again performing the decomposition and the Reynolds averaging. The complex individual term in the Equation of ε can be derived, and the final form of transport equation of ε can be obtained as follow.

$$\frac{D\varepsilon}{Dt} = C_{\varepsilon 1} f_1 \frac{\varepsilon}{k}\left(-\overline{u_i' u_j'}\right)\frac{\partial \overline{U}_i}{\partial x_j} + \frac{\partial}{\partial x_j}\left[\left(\frac{\nu_T}{\sigma_\varepsilon} + \nu\right)\frac{\partial \varepsilon}{\partial x_j}\right] - C_{\varepsilon 2} f_2 \frac{\varepsilon^2}{k} \tag{2.21}$$

The first term on the right-hand side of Equation 2.21 denotes the production of ε; the second one is the diffusion term of ε and the remaining term represents the rate of destruction ε.

2.3.2. Discrete phase modeling

In the Lagrangian approach, the particles are treated as a discrete phase made of spherical particles dispersed in the continuous phase. The particle volume loading is usually assumed negligible so that particles have no feedback effect on the carrier gas, and particle-particle interactions are neglected. In the Lagrangian framework, the controlling phenomena for particle dispersion in the field are assessed using a rigorous treatment of the forces acting on the particle. In general, the detailed flow field is computed first, then a representatively large number of particles are injected in the field, and their trajectories are determined by following individual particles until they are removed from the gas stream or leave the computational domain. Particle motion is extracted from the time integration of Newton's second law, in which all the relevant forces can be incorporated (drag, gravity, lift, etc.). The Lagrangian approach is computationally intensive because it entails tracking a large number of particles until stationary statistics are achieved. On the other hand, the results of Lagrangian particle tracking are physically easier to interpret.

2.3.2.1. Aerodynamic transportation

The Lagrangian method is applied to predict the trajectory of discrete phase particles. The Lagrangian approach starts from solving the transient momentum equation for each particle:

$$\frac{d\vec{u}_p}{dt} = \frac{1}{\tau} \cdot \frac{C_D \cdot Re_p}{24} \left(\vec{u} - \vec{u}_p \right) + \frac{\left(\rho_p - \rho \right)}{\rho_p} \cdot \vec{g} + \vec{F}_B + \vec{F}_S \tag{2.22}$$

The left-hand side of the Equation represents the acceleration of particle per unit particle mass (ms^{-2}), where $\vec{u}_p$ is the particle velocity. The first term on the right-hand side is the drag force where τ is the particle relaxation time

$$\tau = \frac{\rho_p d_p^2}{18\mu} \tag{2.23}$$

where d_p is the particle diameter, μ is fluid viscosity, and Re_p is the relative Reynolds number defined as follows,

$$Re_p = \frac{\rho\left|\vec{u}_p - \vec{u}\right| d_p}{\mu} \tag{2.24}$$

C_D in Equation 2.22 denotes the drag coefficient on particles. Herein, the expression of drag coefficient is defined corresponding to the shape of the particle. For spherical particles, the general correlation was defined as:

$$\begin{aligned} C_D &= \frac{24}{18}\mathrm{Re}_p\left(18 + 2.367\,\mathrm{Re}_p^{\omega}\right) \\ \omega &= 0.82 - 0.05\left(\log_{10}\mathrm{Re}_p\right) \quad \text{for } \mathrm{Re}_p < 20 \end{aligned} \tag{2.25}$$

The $\vec{F}_B$ and $\vec{F}_S$ are the Brownian force and the Saffman's lift force on a unit mass basis, respectively. These forces are included and modeled as follows:

$$\vec{F}_B = \xi\sqrt{\frac{216\mu\sigma T}{\pi d_p^5 \rho_p^2 C_c \Delta t}} \tag{2.26}$$

$$\vec{F}_S = 5.188\frac{\nu^{1/2}\rho d_{ij}\left(\vec{u} - \vec{u}_p\right)}{\rho_p d_p\left(d_{lk}d_{kl}\right)^{1/4}} \tag{2.27}$$

where, ξ is a Gaussian random number with zero mean and unit variance, σ is the Stefan–Boltzmann constant, Δt is the time step for particle tracking, C_c is the Cunningham correction factor for fine particles, and d_{ij} is the rate of deformation tensor. The expression for the Saffman's lift force is restricted to a small particle Reynolds number. In addition, the particle Reynolds number based on the particle-fluid velocity difference must also be smaller than the square root of the particle Reynolds number based on the shear field.

2.3.2.2. Discrete Random Walk Model

In order to reproduce the turbulent particle dispersion due to turbulent fluctuations in the flow, a discrete random walk (DRW) model is adopted. This method is also called the Eddy Interaction Model (EIM). Fluctuations airflow velocity were represented as follow:

$$\vec{u_i} = \overline{U_i} + u_i^{'} \tag{2.28}$$

where $\overline{U_i}$ is mean fluid phase velocity and $\vec{u_i}$ is instantaneous fluid velocity. The turbulence eddies are assumed to be isotropy, and the fluctuating component of instantaneous flow velocity is obtained by:

$$u_i^{'} = \varsigma\sqrt{\overline{u'^2}} \tag{2.29}$$

Here, ζ is a normally distributed random number; k is the turbulent kinetic energy, and the remaining right-hand side is the local root mean square (RMS) velocity fluctuation can be obtained (assuming isotropy) by

$$\sqrt{\overline{u'^2}} = \sqrt{\overline{v'^2}} = \sqrt{\overline{w'^2}} = \sqrt{\frac{2k}{3}} \tag{2.30}$$

2.4. NUMERICAL MODELS OF RESEARCH SUBJECTS

2.4.1. Model information and reconstruction

The upper airway models of three species, i.e., monkey, human, and bulldog, were recruited to describe the airflow characteristic and particle transportation/deposition. The 3D numerical models were reconstructed based on the CT data of a 1.2 kg, 6-month-old cynomolgus monkey, a healthy non-smoking male (Fig 2.11), and eight French bulldogs with ages ranging from 3-13 years old and 8.7 – 13 kg weigh. Herein, the geometries of monkey and human upper airways are inherited from previous research, which were obtained using a Toshiba 64 multi-detector row CT scanner and reconstructed by Mimics software (Materialise NV) (Ito et al. 2017). Meanwhile, the manual segmentation process was performed for each French bulldog to generate the numerical models from the CT images provided by

the Veterinary Medical Centre clients at Yamaguchi University, and the segmentation workflow is presented in Fig 2.12a. Note that a single severe patient French bulldog experienced a surgery; therefore, nine CT data sets were used to reconstruct the upper airway models. The CT data was first converted to the DICOM format and then was directly loaded into the 3D Slicer software via the graphic user interface. The 3D visualization of the CT data set and the gray-level transformation function (as discussed in section 2.2.3) facilitate the determination of the region of interest, for example, the upper airway region in this study. In the segmentation process, the threshold tool, which allowed an intensity range to specify an editable masked region as discussed in section 2.2.3, was applied. The threshold fill was defined as that which covered the dogs' facial features (green area) and separated the air-filled region from the surrounding border instead of merely filling the airway cavities, shown in Fig 2.12b. This method provided a smooth connection between the face and the dogs' upper airway at the external nostril inlet and replicated the nostril shape as accurately as possible. The masked area was then converted into a 3D model and exported to a solid geometric model (Fig 2.12c). The solid model was smoothed using the median smoothing function in 3D Slicer. This tool smooths the boundary surface by removing small extrusions and filling small gaps. The specified kernel size was adjusted to 1.0 mm to fit the current models, which means details larger than 1.0 mm were retained to describe the airway and facial features' original morphometry. The external domain was generated to allow continuous airflow into the nostrils (Fig 2.12d). After the segmentation, nine French bulldog upper airway models, including two open cases, three mild stenosis, one moderate stenosis, two severe stenosis bulldogs, and one postoperative were shown in Fig 2.13. The surgery/veterinary doctor determined the classification of the nostril stenosis levels was determined by the surgery/veterinary doctor based on the outer shape of external nostrils. A detailed discussion about the morphometric features of the upper airway models and the pre- and post-surgery is presented in the following chapters.

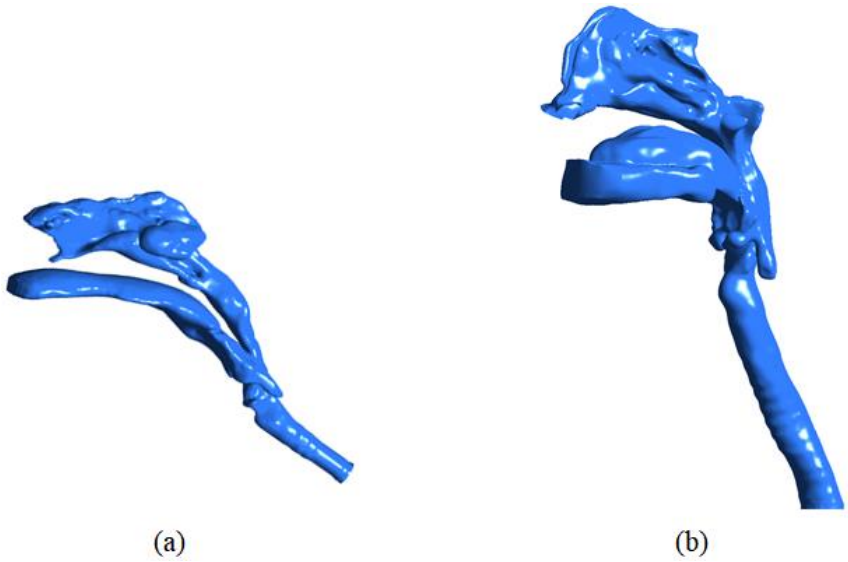

Figure 2.11: The outline of (a) a 6-month-old cynomolgus monkey and (b) a healthy non-smoking male.

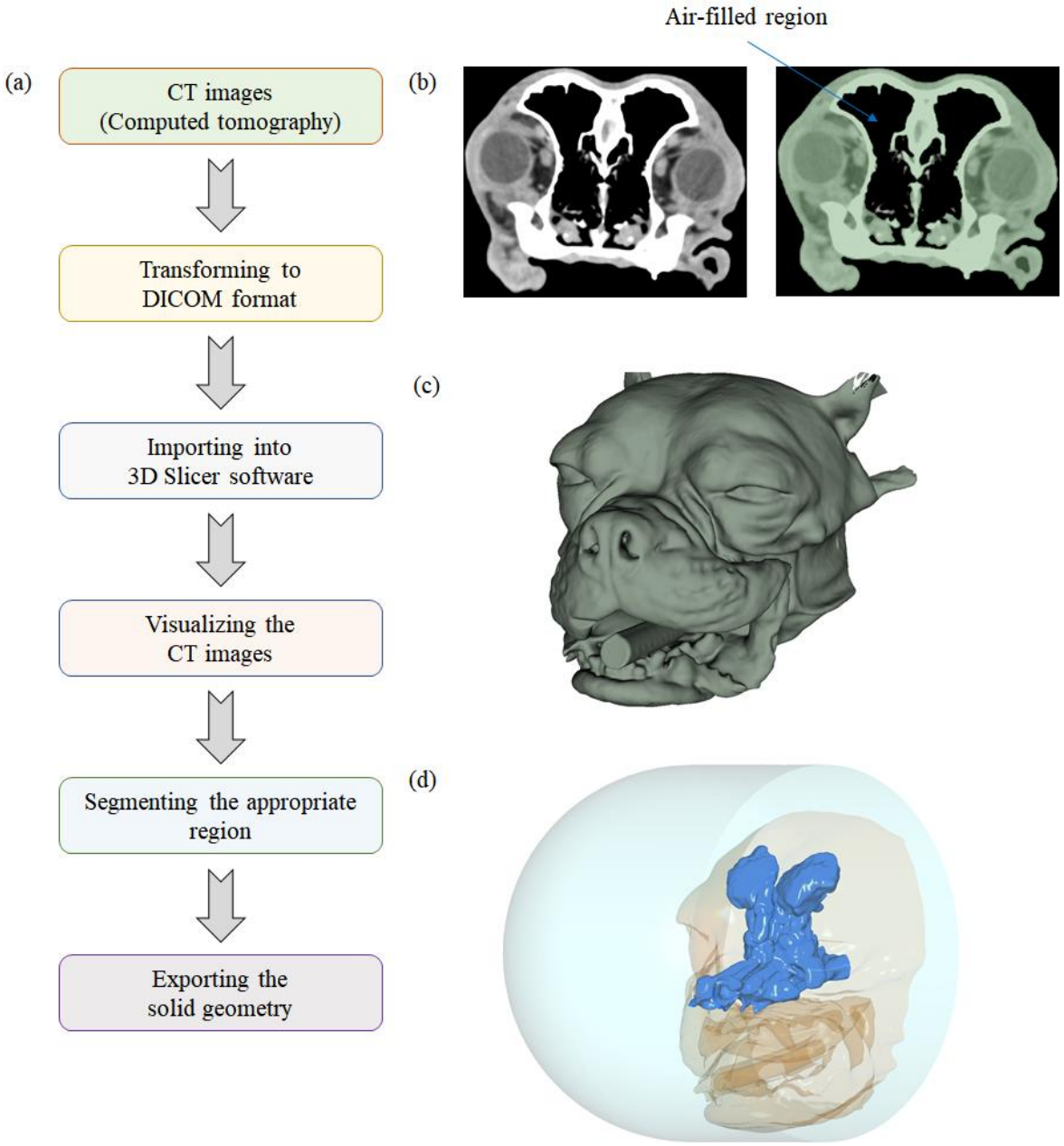

Figure 2.12: The process for reconstruction of three-dimensional (3D) geometry. (a) The diagram describes the essential stages to create the geometry from the computed tomography (CT). (b) A representative CT image was acquired in a transverse plane using a CT scanning machine and threshold segmentation in the 3D slicer software to isolate the air-filled region. (c) The solid geometry model obtained from the threshold tool includes the upper airway and facial features. (d) The complete model with the external domain confirms the actual breathing condition.

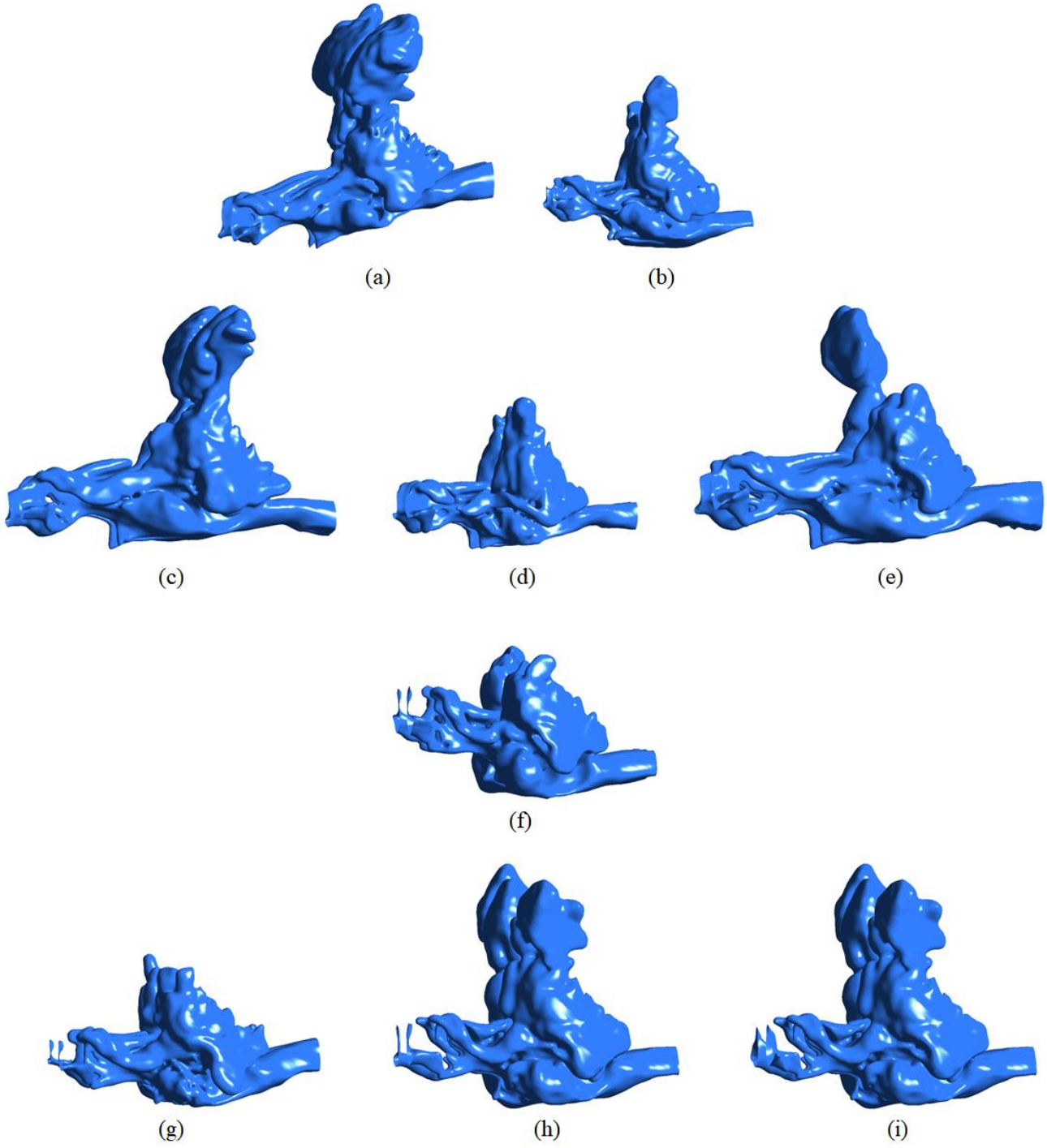

Figure 2.13: The upper airway outline of (a, b) open nose, (b, c, d) mild stenosis, (f) moderate, (g, h) severe stenosis French bulldogs, and (i) post-surgery model of model h.

2.4.2. Computational grid information

After obtaining the 3D geometry models, the discretization process (or well-known as the meshing process) was conducted. Geometries encountered in the upper airway are more likely to be considered complex geometries, which cannot apply the structured mesh type (hexahedral elements). As an alternative, unstructured mesh (tetrahedral or polyhedral elements) was widely used to fill the inside volume of an interesting domain, and the current status of CFD unstructured mesh has become popular in engineering. Many grid generation software is available, including open source and licensed codes, and the commercial software (ANSYS ICEM) was used to perform the meshing process. Generally, the 2D triangles will be automatically created on the geometry surface based on the maximum and minimum mesh size, which can be modified by users. Then, the interior volume will be filled from the surface mesh with a specified growth rate, and all the elements are reconnected again (Delauney method). Nowadays, polyhedral cells are gradually becoming popular and widely used instead of tetrahedral cells and can be built directly or converted from the available tetrahedral elements. The application of polyhedral mesh offers better accuracy and efficiency compared to tetrahedral. Nonetheless, the use of these two mesh types should be considered upon the complex geometry domain of interest.

As discussed above, the unstructured elements are typically used for complex geometry, whereas the structured ones are solely applied for the block-structured geometry that delivered higher accuracy than the unstructured type. Based on the needs of modern engineering disciplines, the solution is usually conducted in complex geometries but requiring an acceptable accuracy. Against this background, a mesh with a combination of two different elements, called hybrid mesh, is developed to meet the requirement of an engineering solution. The unstructured elements are allocated in the complex parts of the flow region; meanwhile, the structured cells are generated adjacent to the boundary walls, in other words, known as prismatic cells. In this study, the solution mainly focuses on the airflow distribution in both laminar and turbulent regimes and the deposition of particles onto the airway wall, which requires a highly accurate calculation in the near-wall region. Therefore, the hybrid mesh was preferred to use in

this study (Fig 2.14). The details of each mesh are discussed in the following chapters.

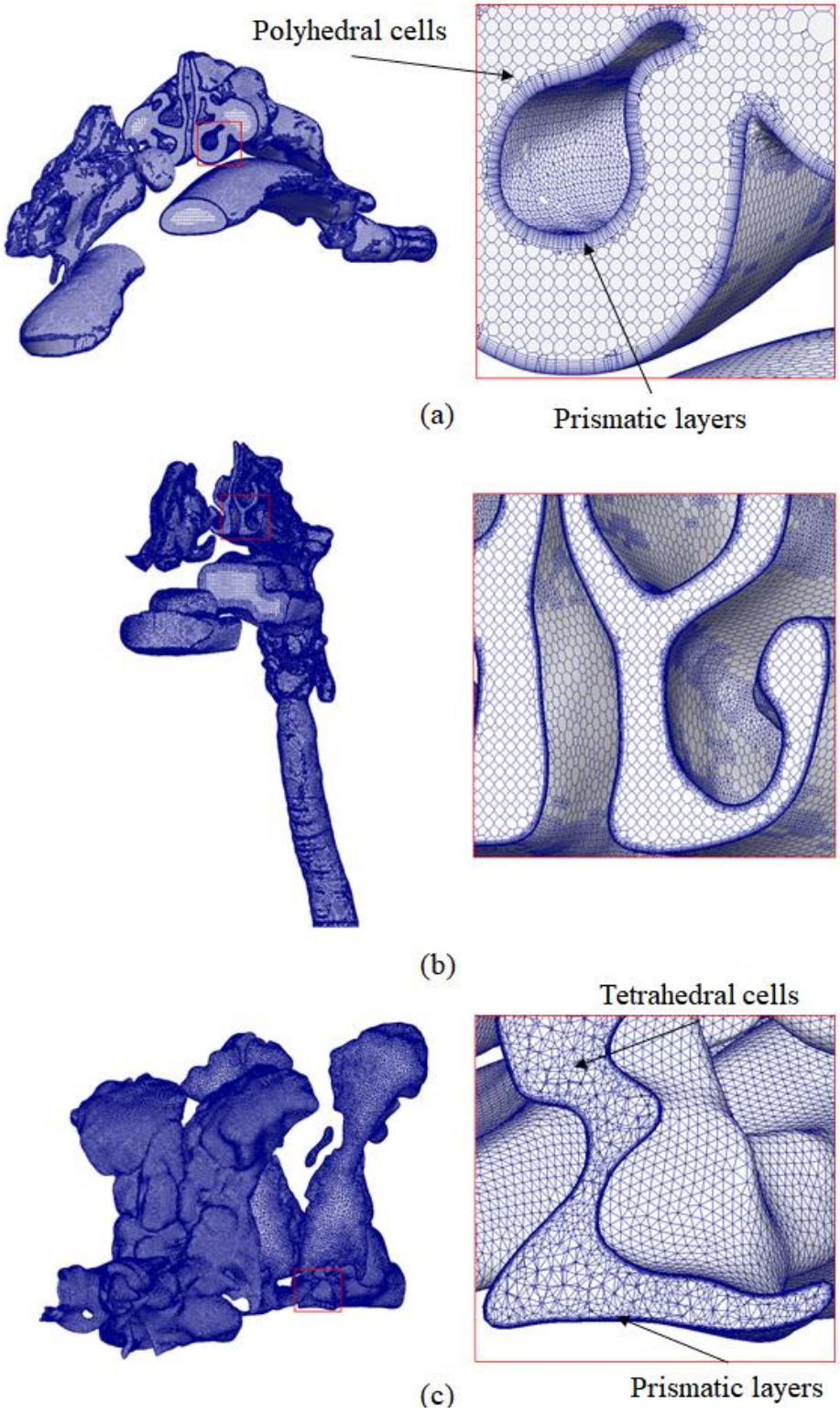

Figure 2.14: The hybrid mesh was applied for (a) monkey airway, (b) human airway, and (c) representative French bulldog airway.

CHAPTER 3

NUMERICAL COMPARISON OF AIRFLOW PATTERN AND ULTRAFINE PARTICLE DEPOSITION IN REALISTIC MONKEY AND HUMAN AIRWAYS

3.1. INTRODUCTION

There are rising concerns regarding the more adverse effects of human exposure to ultrafine particles than fine particles, owing to their higher number concentration and effective surface area (Frampton 2001). The inhaled ultrafine particles were characterized by the high particle number concentration, which is more important than their mass (Donaldson et al. 1998, Saha et al. 2018). The high particle number concentration data was recorded in the indoor space of high-rise buildings in China varied from 2,800 to 2.91×10^4 cm^{-3} (Mullen et al. 2011). The adverse health effects of inhaled ultrafine particles include lung cancer, asthma, chronic disease, neurodegeneration, and brain injury, as mentioned in Chapter 1. In addition, radon progeny, emitted from the rocks and soils, was ubiquitous in indoor space and outdoor air, with the activity-weighted particle size widely varying from 0.5 nm to 1 μm (NRC 1991). As entering the human lungs, the radon elements release the α-ray that adversely impacts lung tissues, consequently causing lung cancer after long-term exposure (Yoon et al. 2016). Recent morphologic and morphometric studies indicate that the nasal structure of nonhuman primates most closely resembles that of humans (Harkema et al. 1987; Yeh et al. 1992). Therefore, macaque monkeys have often been selected as laboratory animals in research involving toxicological infections and therapy related to infectious agents (Cheng et al. 2008; Asgharian et al. 2012). Data regarding the aerosol deposition in monkey airways are helpful to understand the dosimetry of the inhaled materials and provide information to support the extrapolation of animal results to humans. Therefore, in this chapter, the author performed a CFD simulation of the inhaled airflow and ultrafine particle deposition within the macaque monkey and human upper airway models in the current study. The current study presents total and regional deposition fractions of the inhaled ultrafine particles (ranging from 5 nm to 100 nm) in the macaque monkey and human upper airway models. The ultrafine particle deposition curves in

both monkey and human models are presented. The present study can provide a comparison of the ultrafine particle deposition fractions between the upper airways of monkeys and humans and aid in the extrapolation from nonhuman primate exposure to human exposure scenarios.

3.2. LITERATURE REVIEW

Several experimental studies have been conducted to measure micro and sub-micrometer-sized particles in the monkey upper airways (Yeh et al. 1992; Yeh et al. 1997; Kelly et al. 2005; Cheng et al. 2008). Kelly et al. (2005) conducted an *in vitro* experiment on a rhesus monkey model and found that the deposition efficiency increased proportionally with the increase in micro-particle diameter and the inlet flow rate. Cheng et al. (2008) performed *in vivo* measurements in the respiratory tract of six cynomolgus monkeys, using aerosol droplets of size ranging from 2 μm to 5 μm, and observed greater extra thoracic deposition concentration was associated with the larger particles of size 5 μm. Yeh et al. (1997) conducted an *in vivo* experiment on the deposition of ultrafine particles in rhesus monkey airways, using particles of size ranging from 5 nm to 100 nm, and the results showed that the deposition efficiency increased as the size of the ultrafine particles decreased.

The whole-lung deposition models have been widely used to predict the whole lung deposition based on the available simulation data and semi-empirical equations. The multiple-path particle dosimetry (MPPD) model, developed by Applied Research Associates Inc, has been broadly utilized due to its user-friendly, open-source, and time-saving. This model can provide numeric data and graphs regarding the total deposition, regional deposition, and lobar deposition per generation in human and laboratory animal lung models. Due to its undoubted advantages, quantitative deposition studies, which implemented the MPPD model, have been conducted for human and laboratory animals (Anjilvel & Asgharian 1995; Asgharian et al. 2001; Asgharian et al. 2012; Manojkumar et al. 2019). Nevertheless, in the current works of literature, only the dose-depositions of the tracheobronchial and pulmonary regions were thoroughly investigated; this can be attributed to the fact that the MPPD model calculates the deposition fraction in the lower airway based on the reconstructed mathematical models; meanwhile,

the deposition fraction in the upper airway region is determined using the semi-empirical functions based experimental data (Asgharian et al. 2014). This may exert uncertainties in predicting the deposition fraction in the upper airway due to the discrepancies in the airway morphometry among intra – or inter – species. In addition, the site-specific visualization and the deposition fraction of each section in the upper airway, e.g., the vestibule and the valve, the nasal turbinate, the nasopharynx - larynx and trachea, are currently unattainable by using the MPPD model.

Several CFD studies have been conducted on the deposition of micro and sub-micrometer-sized particles in the human upper airway region (Zhang and Kleinstreuer 2004; Longest and Xi 2007; Xi and Longest 2008; Zhang and Kleinstreuer 2011; Ge et al. 2012; Tian et al. 2017). However, there have been a few studies on the deposition of inhaled particles in the respiratory system in monkeys (Schroeter et al. 2013). The first attempt to simulate particle deposition, using particles of size 0.01 μm to 5 μm, in the lower respiratory tract of rhesus monkeys was reported by Martonen et al. (2001). They reported significant differences between the deposition patterns in the lung models of monkeys and humans. Subsequently, Asgharian et al. (2012) made an effort to demonstrate the deposition of 0.01 μm to 10 μm inhaled particles in the lungs of rhesus monkeys. Compared to humans, the deposition fraction of respirable size particles were reported to be higher in the respiratory tract of rhesus monkeys. Schroeter et al. (2013) performed a study on the numerical prediction of the deposition of inhaled fine- and ultrafine particles nasal passages in the infant and adult rhesus monkey airway models. The author found that the variability in particle deposition fractions between the monkey models was substantially reduced when plotted against the non-dimensional parameters (Stokes number and diffusion parameter ($Sc^{-0.08}\Delta^{0.25}$) corresponding to fine- and ultrafine particles, respectively). Dong et al. (2018) numerically detailed the final destination of inhaled ultrafine particles varied with the initial releasing locations in the human nasal cavity. Their results indicated that the ultrafine particles that entered the airway through the superior corner of the nostril were deposited in the olfactory region, while the particles deposited in the middle meatus region were recorded as releasing from the top third of the nostrils. The particles

deposited in the inferior meatus were initialized from the bottom of the nostrils, and most of the particles released from the center of the nostrils were deposited in the rest of the nasal cavity. Phuong et al. (2019) investigated the effect of flow patterns on micro-size particle deposition in the upper airways of the macaque monkeys and humans by means of the application of the CFD technique. The study results suggested that geometric factors greatly contributed to the dominance of the local deposition fraction in the central nasal passages of the human airway and in the vestibule region of the monkey airway. To the best of our knowledge, no previous numerical or analytical studies have performed a comparison between the ultrafine particle transport and deposition in monkey and human upper airways.

3.3. METHODOLOGY

3.3.1. Upper airway models

Computational geometries of the human and monkey upper airways were used in this chapter, the outline of the models was shown in Chapter 2 (section 2.4.1). Herein, the upper airway models were divided into four regions, based on the anatomical features, namely: (1) the vestibule and the valve, (2) the nasal turbinate, (3) the nasopharynx - larynx, and (4) the trachea, as shown in Fig 3.1. In this study, the human and monkey upper airway models were re-meshed using the hybrid mesh, with the combination of polyhedral elements and prismatic layers, as shown in Chapter 2 (section 2.4.2). The number of meshes used for the monkey and human airway models was 6.4 and 6.7 million, respectively. In order to better represent the flow conditions through the nostril inlets, external cylindrical analytical domains were included in each model (Doorly et al. 2008; Inthavong et al. 2013).

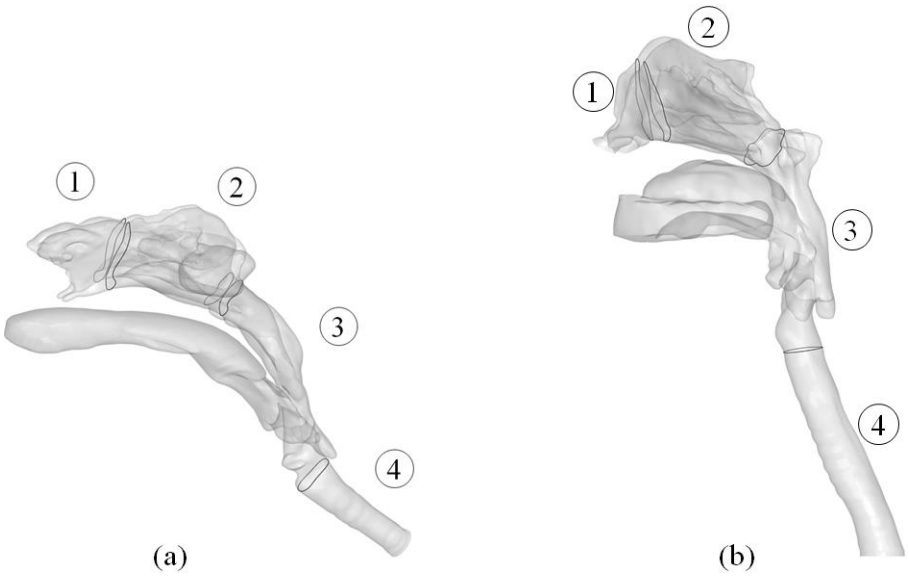

Figure 3.1: Schematic diagram of the computational domain of monkey airway model (a) and human airway model (b); labeled with four major airway regions, (1) the vestibule and the valve, (2) the nasal turbinate, (3) the nasopharynx-larynx and (4) the trachea.

3.3.2. Numerical boundary conditions for airflow simulation

In the current study, the inhaled flow patterns in human and monkey geometries were analyzed using a low Reynolds number (LRN) *k-ε* model, as described in Chapter 2, section 2.3.1. The turbulent kinetic energy at the inlet was assumed with 10% turbulence intensity, and the inner surfaces of the upper airway models were assumed solid, with a no-slip boundary condition. Inhaled airflow simulations were conducted in a physiologically steady-state, using Ansys-Fluent 19 (ANSYS, Inc., Canonsburg, PA) to solve the viscous, incompressible Navier-Stokes equations. The airflow conditions were specified at the trachea opening with the constant negative velocity, which is perpendicular to the cross-section of the trachea opening. A zero-gauge pressure condition was set at the external cylinder domain in front of the nostril region to confirm the fully developed airflow entered the nostrils. The hydraulic diameters of the trachea opening were defined as the characteristic length scale of the model. The wall treatment was assumed a no-slip condition for airflow simulation. A second-order upwind scheme was used for the convection term, and the SIMPLE algorithm was employed. Airflow simulations were conducted with

the inhalation of air at room temperature (20°C), while air density and viscosity values were 1.225 kg/m^3 and 1.789 × 10^{-5}kg/m-s, respectively. In the human airway models, the inhalation flow rates of 10 L/min and 20 L/min were used in accordance with the light and moderate activity conditions, respectively.

In order to calculate the minute volume under rest conditions, Guyton's formula (Guyton 1947) was applied to estimate the respiratory minute volume of the monkey airway. The equation (3.1) is stated as follows:

$$MV = 2.35 \times BW^{3/4} \tag{3.1}$$

where MV is the minute volume (mL/min), 2.35 is a constant value obtained from six monkey subjects, and $B.W.$ is the body weight (g) of the monkey. In a monkey with a bodyweight of 1,200 g, the MV was estimated to be 480 mL/min (0.48 L/min) under the specified inhalation conditions. Assuming an equal duration of the inhalation and exhalation processes, the inspiratory flow rate of 0.96 L/min was selected, corresponding to twice the minute volume. Inhalation airflow simulations were conducted at the flow rates of 0.96 L/min and 1.92 L/min to span a range of physiologic breathing rates in both monkey and human models, as listed in Table 3.1. Table 3.2 summarizes the numerical and boundary conditions of the two upper airway models. All the predictions for airflow patterns and particle transportation and depositions were conducted for the inhalation process in this study only.

Table 3.1. Respiratory parameters in monkey and human airway models

	Monkey airway model		Human airway model	
	Light	Moderate	Light	Moderate
Q (L/min)	0.96	1.92	10	20
U (m/s)	0.5	1.0	0.8	1.6
Re	187	374	759	1,518

Table 3.2. Numerical and boundary conditions

	Monkey airway model	Human airway model
Turbulent model	Low-Reynolds type k-ε model (Abe Kondoh Nagano)	
Grid style	6.4 million mesh (Unstructured, Hybrid mesh)	6.7 million mesh (Unstructured, Hybrid mesh)
Outflow boundary (Trachea opening)	Case 1: *Q*= 0.96 L/min Case 2: *Q*= 1.92 L/min TI= 10%	Case 1: *Q*= 10 L/min Case 2: *Q*= 20 L/min TI= 10%
Inflow boundary	Gradient zero condition at the nasal opening, T_{air} = 293^{o}K	
Wall treatment	Velocity: no slip Temperature: Monkey (T_{wall} = 311^{o}K); Human (T_{wall} = 310^{o}K) Particle: Trap (discrete phase)	

3.3.3. Ultrafine particle properties and boundary conditions for discrete phase modeling

Particle trajectories were calculated using the discrete phase model in the Ansys-Fluent software to solve the Lagrangian equation. Previous studies have utilized this method to predict the deposition of ultrafine particles ranging from 1 nm to 100 nm in size in realistic human airway models (Wang et al. 2009; Dong et al. 2018). Several acting forces were employed to predict the ultrafine particle transport and deposition characteristics of the airway models, as discussed in Chapter 2 (section 2.3.2). The Eulerian continuous phase (airflow field) was solved first; subsequently, the Lagrangian discrete phase for particle trajectories was computed. The monodisperse ultrafine particles were introduced into the flow field through the nostril area at an initial velocity, which was assumed to be the same as the entering flow velocity. Ultrafine particles were assigned a density equal to pure water, i.e., 1,000 kg/m^3, and the diameters (d_p) ranged from 2 nm to 100 nm. Altogether, 10,000 particles were generated and tracked in each case for each separate particle diameter. In this analysis, a perfect trap condition was applied as the wall boundary condition for Lagrangian particle tracking.

Deposition fractions for the whole model and specific regions within the model were computed by dividing the number of particles deposited by the number of particles injected. Airway walls were defined to be perfectly sink during the discrete phase. In other words, the ultrafine particles were considered deposited on the surfaces, with no possibility of rebounding into the flow.

The effective diffusivity of the particle (D) can be calculated from the Stokes-Einstein equation provided by Hinds (1999), as shown in Equation (3.2).

$$D = \frac{k_B T C_c}{3\pi\mu d_p} \tag{3.2}$$

where k_B is the Stefan–Boltzmann constant, T is the absolute temperature (K), μ is the air viscosity, d_p is the particle diameter, C_c is the Cunningham correction factor.

3.3.4. Deposition fraction

In the current study, the deposition fraction (η) was computed, based on the ratio of the number of particles deposited, to the total number of particles inhaled, as shown in Equation (3.3).

$$\eta = \frac{C_{dep}}{C_{in}} \tag{3.3}$$

where C_{dep} is the number of particles deposited in the airways and C_{in} is the number of particles inhaled through the inlet of the airways.

The regional deposition fraction (η_i) was also defined as the ratio of the number of particles deposited within a region to the total number of particles entering through the nostril. The deposition fraction for region i can be expressed as shown in Equation (3.4):

$$\eta_i = \frac{C_{RDi}}{C_{in}} \tag{3.4}$$

where C_{RDi} is the number of particles deposited in region i, reflecting the anatomical structures of the monkey and human airways.

Here, the particle concentration (C) was determined as the ratio between the number of particles deposited within a region and the corresponding regional surface area as described in Equation (3.5):

$$C = \frac{C_{RDi}}{A_i} \tag{3.5}$$

where A_i is the surface area of region i, the regional surface area data of both monkey and human airways, as listed in the Table 3.3.

Table 3.3. Regional surface area of monkey and human airways

	Surface area, A_i (cm^2)	
Anatomical structure	Monkey	Human
Vestibule and valve	11.21	28.29
Nasal turbinate	31.66	107.72
Nasopharynx-larynx	18.33	74.38
Trachea	5.48	47.24
Total	**66.68**	**257.63**

3.4. RESULTS AND DISCUSSION

3.4.1. Airway structure of monkey and human

Figure 3.2 describes the size distribution of cross-sectional planes along the upper airways of monkey and human. The red dash-dot lines indicate the area of cross-sectional planes in the left nasal passage, and the blue dash lines denote the right nasal passage. The solid green lines represent the total area of the nasal passages; meanwhile, the solid brown lines imply the cross-sectional area where the two airway passages are confluent into a single airway. As defined in Fig 3.1, the four separated regions are partitioned by the vertical black dash line, from left to right, including the vestibule and valve, the nasal turbinate, the nasopharynx-larynx, and trachea regions, respectively. As can be seen from Fig 3.2, the right nasal passage shows a higher area than that of left nasal passage in both monkey and human airways, which evidences the homogeneity in nasal cavity morphometric features of monkey and human. However, the total size of the human airway is obviously larger than that of a monkey. Besides, the total area data also presents the significant expansion of airway structure in the nasal turbinate region in both investigated models. In nasopharynx-larynx and trachea regions, the fluctuated trend of cross-sectional planes area is observed to be consistent between monkey and human. These results imply the potential comparison and extrapolation between monkey and human involving the investigation about the adverse health effects of inhaled toxic substances. Nonetheless, the discrepancies in local geometric features are inevitable; therefore, the geometric parameter should be taken into account to minimize the intra-subject variability and then facilitate the extrapolation between two species.

Based on this background, the geometric parameter so-called minimum cross-sectional area (A_{min}) was proposed. It has been suggested that the effects of intra-subject variability might be minimized by applying the A_{min} for the anterior region, which has been evidenced as the preferred site of particle deposition; therefore, the morphometric features of the posterior region could be eliminated from the calculation of A_{min} (Kelly et al. 2005). Thus, the minimum cross-sectional area in this study was calculated by averaging the three cross-sectional area in the vestibule and valve region (as marked at

positions 1, 2, and 3 in Figs 3.2a-b). The A_{min} of the monkey was 0.32 cm^2, which is smaller than the reported value of Kelly et al. (A_{min} = 0.43 cm^2); this is attributed to the size of the monkey subject used in their study. Kelly et al.'s (2005) monkey model was created from a postmortem cast of the nasal airway of a 12 kg monkey, while our a mon was an infant monkey weighing 1.2 kg. In the case of human airway, the A_{min} = 2.1 cm^2, which is consistent with the reported data of Cheng (2003) (A_{min} = 2.16 cm^2). The results of A_{min} are applied in the further comparison of this study.

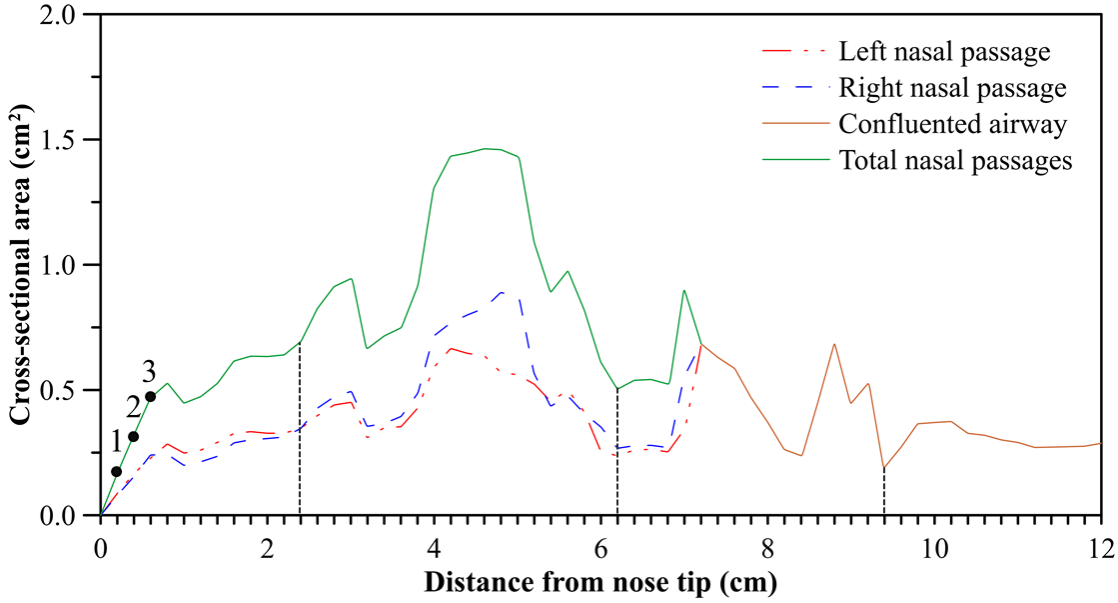

(a)

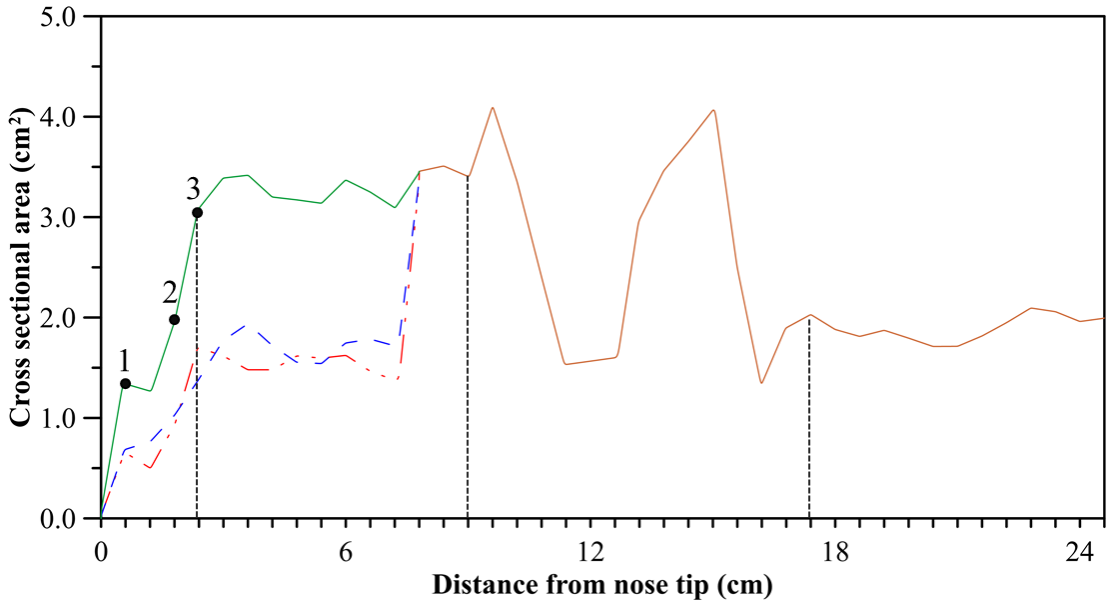

(b)

Figure 3.2: Area of cross-sectional planes from the nose tip to the end of trachea out of (a) monkey airway and (b) human airway.

3.4.2. Inhaled airflow distribution

The flow patterns within human and monkey airway models have been validated using the particle image velocimetry (PIV) method. The CFD simulation results in both monkey and human airways were confirmed to be reasonably consistent with the *in vitro* experiment (Phuong & Ito 2015; Kim et al. 2018; Phuong et al. 2020). Furthermore, the standard test guidelines for applying the CFD technique in enclosed spaces and grid independence were followed and checked carefully to ensure quality control (Ito 2014; Ito, Inthavong, Kurabuchi, Ueda, Endo, Omori, Ono, Kato, Sakai, Suwa, et al. 2015a; Ito, Inthavong, Kurabuchi, Ueda, Endo, Omori, Ono, Kato, Sakai, Suwa, et al. 2015b; Ito, Inthavong, Kurabuchi, Ueda, Endo, Omori, Ono, Kato, Sakai, Suwa, et al. 2015c).

The distribution of airstream is described in Fig 3.3 by the 50 representative streamlines for both light and moderate breathing conditions in monkey and human upper airway models. The highest velocity magnitude is denoted by the red, and the blue represents the lowest one. Generally, the flow was accelerated in the vestibule region due to the narrowing of this region in both human and monkey airways (almost reached the highest velocity around 2.4 and 4.8 m/s in case of light and moderate breathing conditions, respectively). Besides, the swirling flow (or known as the secondary flow) is also observed in the vestibule and the valve region, which is consistent with the observation proposed by Morgan et al. 1991. The sudden decrease of airstream velocity was recorded in the nasal turbinate region of both monkey and human models, attributed to the dramatic enlargement and the complexity of the geometric structure in this region, as discussed in the previous section. After leaving the nasal turbinate region, the airstream is bent around 90^{o} to the nasopharynx-larynx region. The larynx jet is observed at the glottis region in monkey and human airway models due to the reduction of the airway's cross-sectional area. Also, the larynx jet is titled toward the anterior wall of the trachea region. The distribution of inhaled air seems to be independent of the inlet flow rate.

Figure 3.4 shows the velocity contours in four cross-sections of the airway models, at the inspiratory flow rates of 0.96 L/min and 10 L/min, in monkey and human airway models, respectively. The current

study observed that in certain significant regions, the airflow direction in the monkey airway differs from that in the human models. The inhaled airflows attained the highest velocity after entering through the nostril and moving upwards through the nasal vestibule and the valve region (Figs 3.4a-b, cross-sections 1A and 1B). In the monkey airway model, the airflow velocities were observed to be reduced in the region of the nasal turbinate (Fig 3.4c, cross-section 2A). Most of the air in the monkey airway passed through the middle meatus and a part of the inferior meatus (Fig 3.4c, cross-section 2A). In the human airway model, most of the air passed evenly through the inferior, middle, and superior meatuses, while low velocities were observed at the topmost regions of the superior meatus (Fig 3.4d, cross-section 2B). As the airflow reached the nasopharynx, the flow is mainly concentrated in the airway center, as shown in the cross-sections 3A and 3B (see Figs 3.4e-f). High velocity was observed in the cross-sections 4A and 4B (Figs 3.4g-h) and along the anterior regions of the trachea in both the airway models.

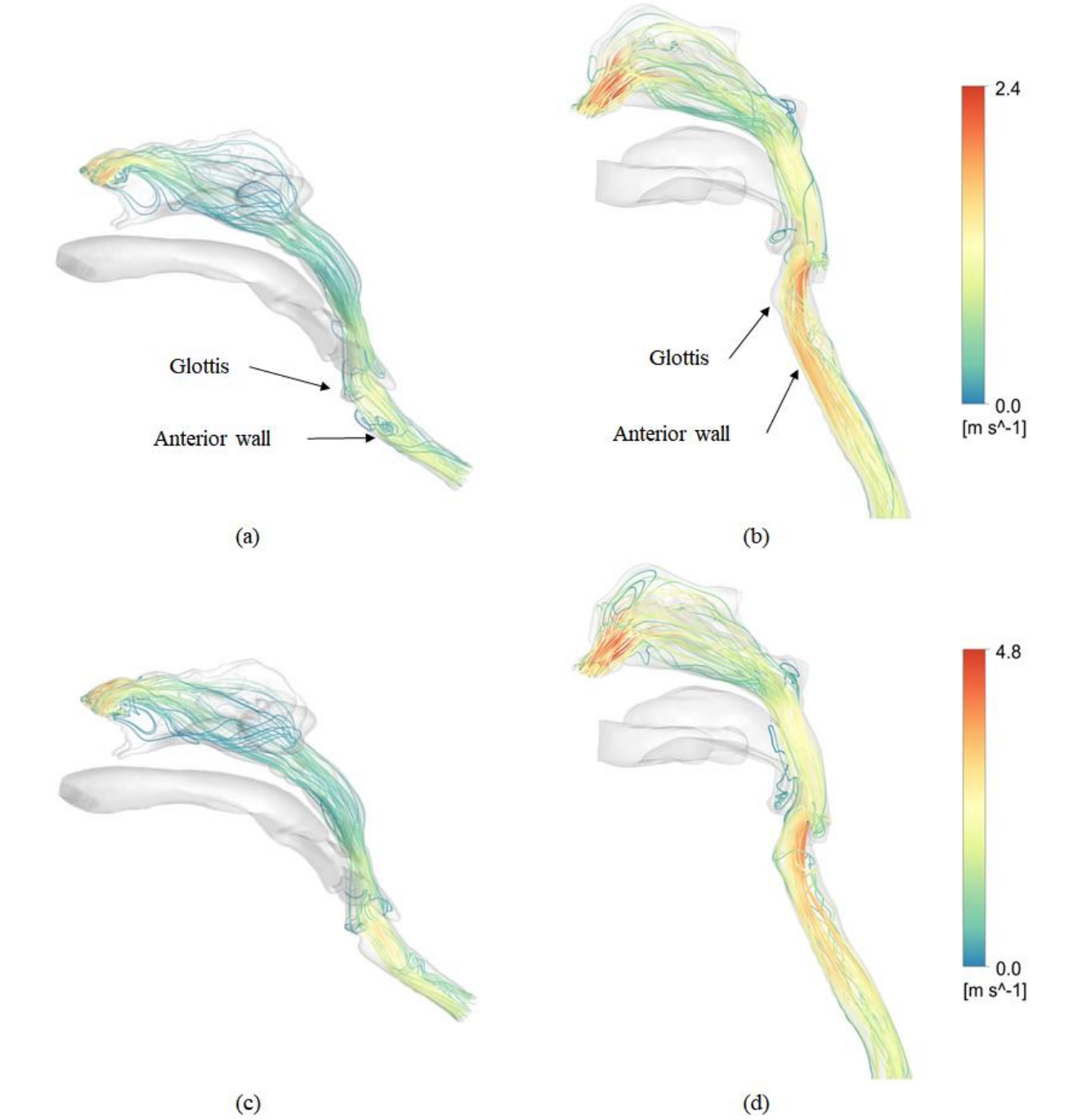

Figure 3.3: The distribution of 50 representative streamlines at light breathing (a) Q_{in} = 0.96 L/min – monkey airway, (b) Q_{in} = 10 L/min – human airway, and at moderate breathing (a) Q_{in} = 1.92 L/min – monkey airway, (b) Q_{in} = 20 L/min – human airway.

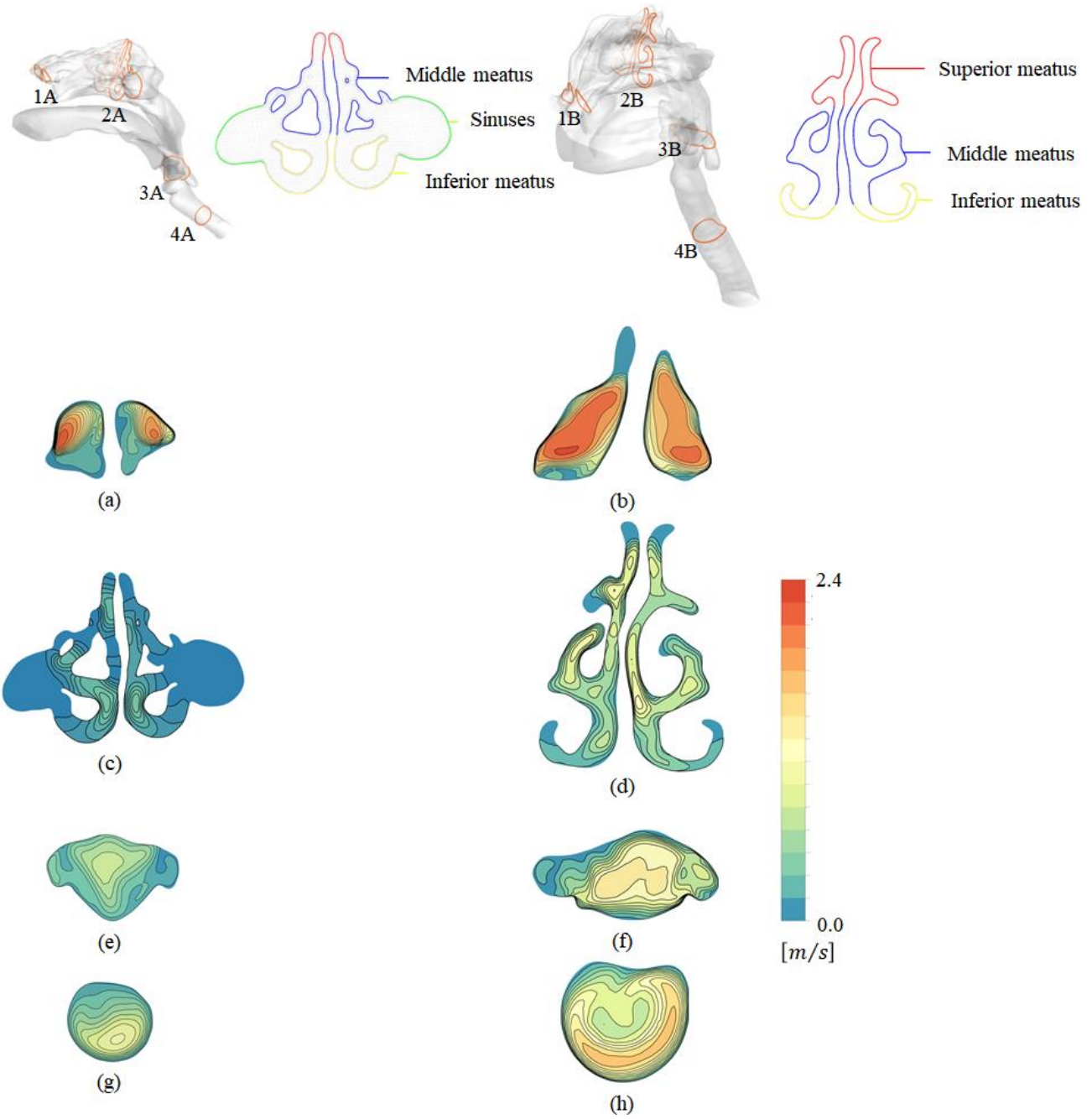

Figure 3.4: 2D velocity contours in different sections at the inhalation rate of 0.96 L/min in the monkey airway model and 10 L/min in the human airway model.

3.4.3. Brownian force influence on single-particle migration

Due to the very low mass of ultrafine particles, the inertia effect can be ignored as it does not have a noticeable effect on particle motion; instead, Brownian motion becomes the dominant mechanism. The Brownian motion of a single ultrafine particle, which was released at the center of the left nostril in both the models, is schematically displayed in Fig 3.5, showing the acceleration of the particle against time. The effect of the Brownian force on the particle trajectories was computed in both the cases: one, which was calculated after considering the forces in Equation (2.22) (Chapter 2, section 2.3.2.1) but without the Brownian force, and one with the calculation involving all the forces, including the Brownian force. As shown in Fig 3.5a, the effect of the Brownian motions was observed clearly in the case of ultrafine particles with d_p = 5 nm due to the fluctuating acceleration. The ultrafine particles with d_p = 100 nm showed steady acceleration, as depicted in Fig 3.5b, compared to the particles with d_p = 5 nm even when the Brownian force was taken into consideration. The elapsed time of 100 nm particle was recorded greater than that compared to the particle with d_p = 5 nm. Moreover, the ultrafine particle with d_p = 5 nm was also observed to have higher fluctuating acceleration, compared to the ultrafine particle with d_p = 100 nm, while passing through the human airway model (see Figs 3.5c-d). Similarly, in the human airway model, the elapsed time for passing through the model of ultrafine particle with d_p = 100 nm was longer compared to the ultrafine particle with d_p = 5 nm.

The current study observed that the acceleration of the particles oscillated rapidly with time in a solid line (representing the involvement of Brownian force), which proved that the Brownian force is the dominant force in the case of the ultrafine particles with d_p = 5 nm. In this scenario, it can be suggested that the Brownian force is an essential factor, which has profound influences on 5 nm particles and gradually declines as the d_p increases to 100 nm. The different impacts of Brownian force may exert the variation on the deposition fraction of 5 and 100 nm particles.

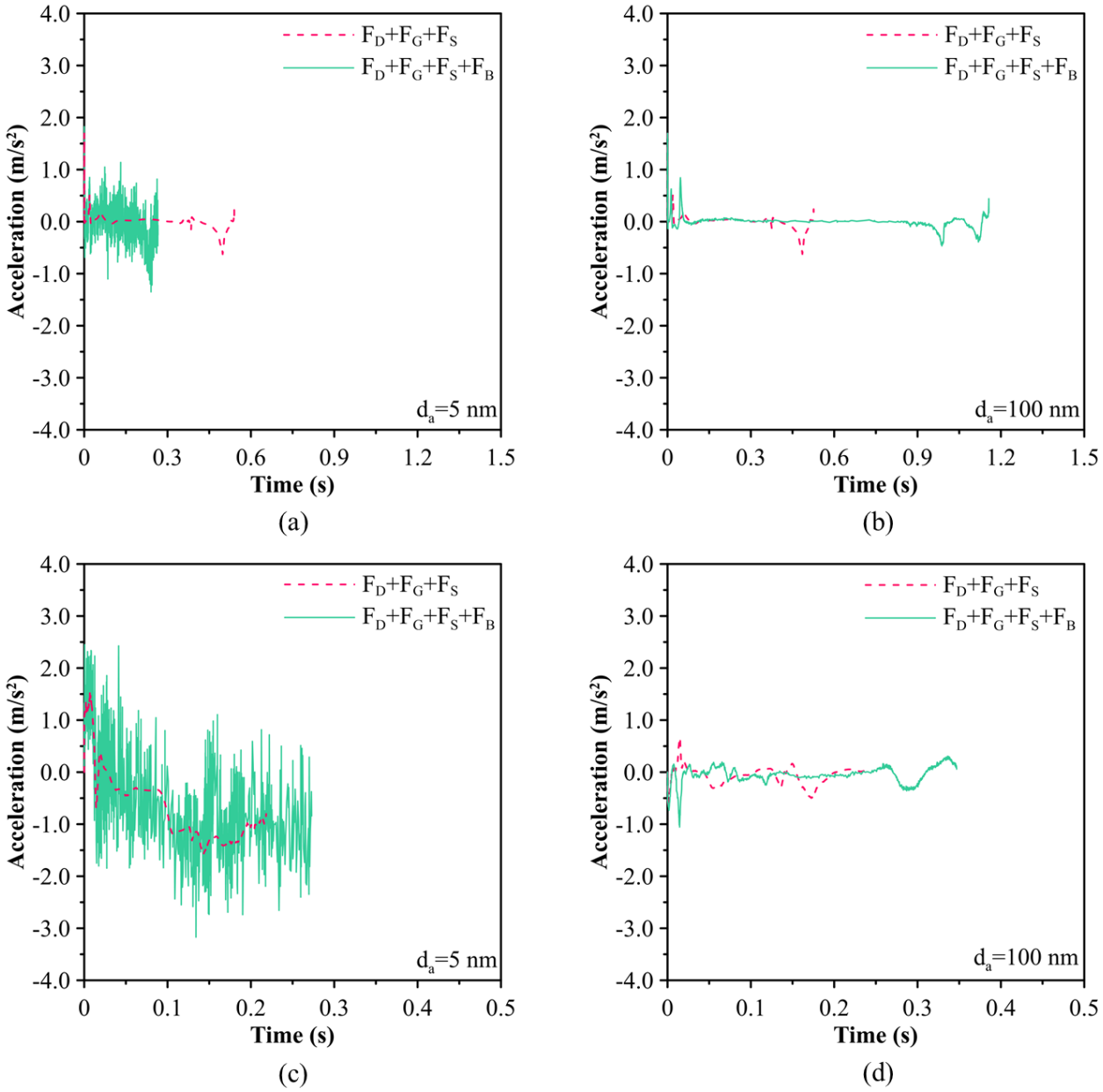

Figure 3.5: Time series of single-particle migration in the (a, b) monkey airway model (Q_{in} = 0.96 L/min) and (c, d) the human airway model (Q_{in} = 10 L/min).

3.4.4. Comparison of the ultrafine particle deposition in the monkey and human upper airway models with experimental data

The simulation of particle deposition involving the ultrafine particles used in the current study was compared with experimental results to confirm the accuracy of the particle tracking method. Deposition efficiencies of the monkey airway model were plotted against the particle diameters in both in vivo (Fig 3.6a) and in vitro experiments (Fig 3.6b). Figure 3.6a shows the deposition fraction of each particle size in the monkey airway model plotted against the particle diameter and compared with the in vivo experimental data of Yeh et al. (1997). The experiment was conducted using eight adult male monkeys with ages ranging from five years to eight years. In the in vivo and in vitro experiments of monkey airway, only the deposition results of the inhalation process were collected and discussed at the end of the exposure process. In the present study, the inhalation flow rate at 0.96 L/min was used for the comparison, which was in accordance with the anesthetized experimental conditions of the aforementioned study. In general, the simulated results had a good correlation with the experimental data, although there were some differences between simulation and experimental results. These discrepancies can be attributed to the differences in geometry, including the morphological parameters and anatomical details. Deposition fractions in both simulated and experimental data shared the same downward trend as the particle diameter increased. In the case of Q_{in} = 0.96 L/min, the simulated airway deposition fraction was observed to be 0.054 (5.4%) for the ultrafine particles with d_p = 100 nm, compared to the simulated airway deposition fraction of 0.48 (48%) for the ultrafine particles with d_p = 5 nm; indicating that the particles with smaller size displayed the higher deposition fraction. The simulation results were observed to be comparable to the experimental results for the deposition fraction. As shown in Fig 3.6b, the current study results were analogous with the in vitro experimental data reported by Yeh et al. (1992). As the inlet flow rate increased to 1.92 L/min, a lower deposition fraction for the particles in the size range of 5 nm to 25 nm was recorded in both studies.

Figure 3.7a shows the variation in deposition fraction of the human airway model, according to the variation in particle sizes and flow rates. In this analysis, the predicted deposition results were conducted under the inhalation process corresponding to the experimental condition of both *in vivo* and *in vitro* measurement. Two healthy subjects (subject C and D) were selected for comparison with the present study results, owing to the similarities in weight and height (Cheng et al. 1996). Data were obtained with the breathing patterns of nose-in/mouth-out, at constant inspiratory flow rate 10 L/min and 20 L/min. It was observed that for given particle size, the particle deposition decreased with an increase in the flow rate, as diffusion had more chances to disperse the ultrafine particles at lower volume flow rates. Fig 3.7b shows a comparison of the numerical results of the current study with the experimental data reported by Kelly et al. (2004), at the inhalation flow rates of 10 L/min and 20 L/min. The *in vitro* experimental data was conducted using three-dimensional replicas built using MRI (Magnetic resonance imaging) data, but with different 3D printers; the SLA and the Viper. Due to the absence of deposition data regarding the particles of size ranging from 30 nm to 150 nm in the Viper model, only the deposition data from the SLA model were taken into account in this comparison. Similar to the study done by Cheng et al. (1995), the two replicas of the upper airway, extending from the nostrils to upper trachea, were included. The ANOT1 (Adult-Nasal-Oral-Tracheal) model was reconstructed completely, based on the postmortem cast of a male adult. Meanwhile, the anterior parts (vestibule, oral and nasal cavity region) of the ANOT2 model was based on a cast from a living male and the posterior parts (oropharynx, larynx, and upper trachea) were based on the postmortem model of an adult. The numerical results of present study and experimental data of both previous studies were compared using a scatter chart. It was observed that the deposition fraction rates were inversely proportional to the particle's diameter and inlet flow rate.

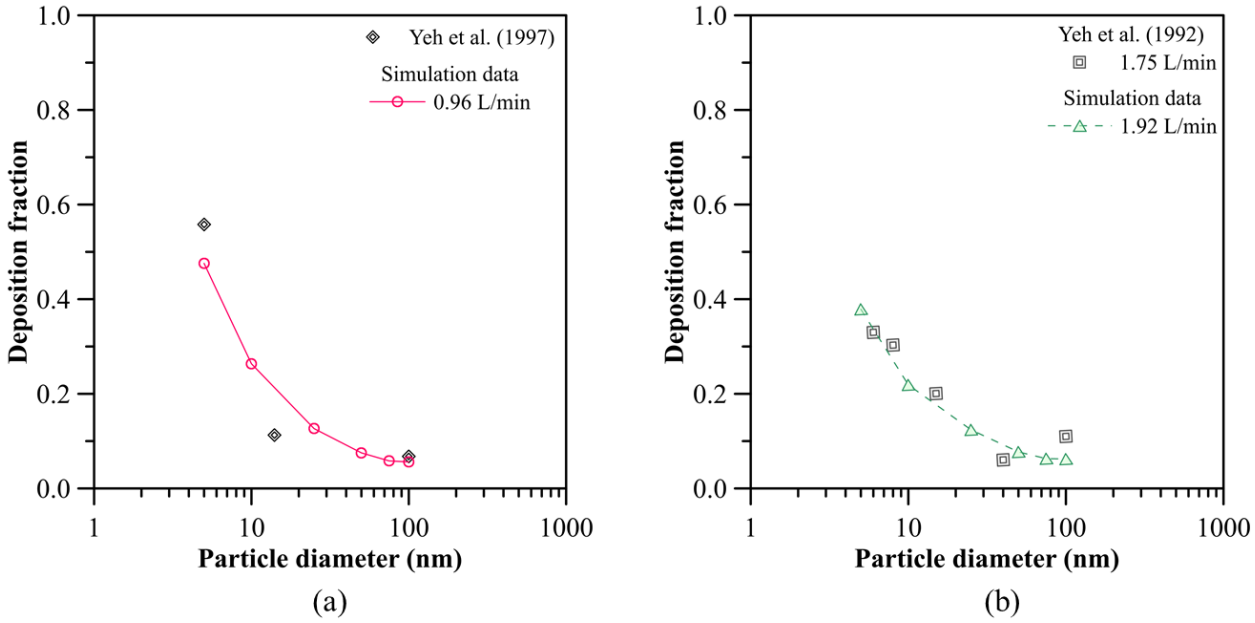

Figure 3.6: Deposition fraction in the monkey airway model versus the ultrafine particle diameter, at inhalation flow rates 0.96 L/min and 1.92 L/min; compared with (a) the *in vivo* experimental data from a study done by Yeh et al. (1997) and (b) *in vitro* experimental data from Yeh et al. (1992).

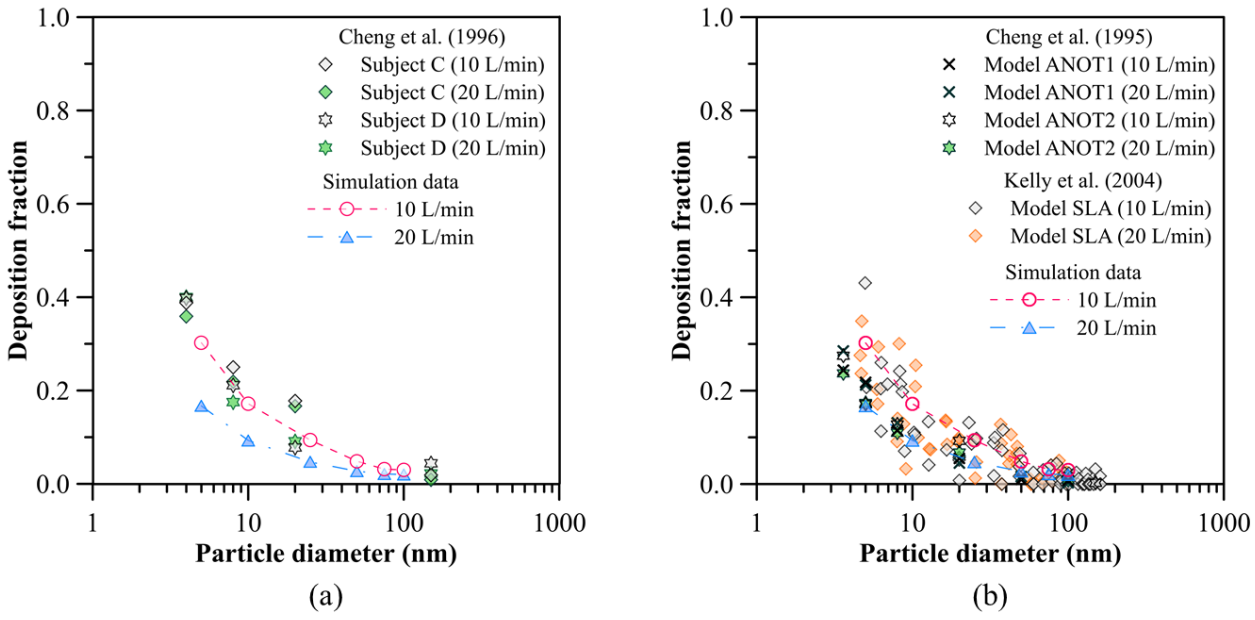

Figure 3.7: Deposition fraction in the human airway model versus the ultrafine particle diameter, at the inhalation flow rates of 10 L/min and 20 L/min; compared to (a) the *in vivo* experimental data of Cheng et al. (1996) and (b) *in vitro* experimental data of Cheng et al. (1995) and Kelly et al. (2004).

3.4.5. Comparison of the deposition fraction between monkey and human airway models

The deposition fractions pertaining to a wide range of particle sizes, ranging from 2 nm to 100 nm, were plotted to perform the comparison between monkey and human airway models (Fig 3.8a). The particle removal efficiency in the monkey airway model was observed to be much greater than the human airway model; particularly in particles with diameters of less than 25 nm. In the current study, the deposition rates of the smallest particles (d_p = 2 nm) under the light condition were observed to be about 0.85 (85%) and 0.63 (63%) in the monkey and human airway models, respectively. Under moderate conditions, the differential deposition fraction between the two models increased to 0.35 (35%), and higher values were observed in the monkey model, compared to the human model (0.76 (76%) in the monkey model and 0.41 (41%) in the human model). As the size of the ultrafine particles increased, the deposition gap between the monkey and human airway models was observed to decrease and was almost insignificant for particles of size 100 nm. Additionally, the deposition fraction was observed to decrease with the increase in the inlet flow rate and particles size in each model. These results indicate that the diffusion term relating to the airflow (Q) and particle diffusion coefficient (D) have a significant influence on particle deposition. Cheng et al. (1995) and Swift et al. (1992) successfully mitigated the impact of the diffusion term by using the $D^{1/2}Q^{-1/8}$ parameter. Furthermore, Cheng et al. (1996) included the ratio A_s/A_{min} and S_f (airway shape complexity) in the diffusion term to fit the deposition data of ten subjects. Asgharian et al. (2012) proposed using the ratio of surface area to nasal passages volume (A/V) to extrapolate the deposition efficiency in monkeys of different ages. Therefore, in the current study, we introduced the diffusion term with geometric factor ratios comprising of $\left[(A_{\text{Human}}/V_{\text{Human}})/(A_{\text{Monkey}}/V_{\text{Monkey}})\right]$ in Equation 3.10 and $\left[A_{\text{min - human}}/A_{\text{min - monkey}}\right]$ in Equation 3.11 to generate the deposition fitting curves for the monkey and human airway models. The values of $A_{\text{min - monkey}}$, A_{Monkey}, V_{Monkey} (monkey airway model) and $A_{\text{min - human}}$, A_{Human}, V_{Human} (human airway model) were calculated as follow and listed in Table 3.4.

Table 3.4. Geometric factors in monkey and human airway models

	Surface area, A (cm^2)	Volume, V (cm^3)	A/V	A_{min} (cm^2)
Monkey airway model	66.68	11.49	5.80	0.32
Human airway model	257.63	86.75	2.97	2.10
Ratio			0.51	6.56

Introducing these geometric parameters with the diffusion term may contribute to the mitigation of interspecific morphological differences onto the features of ultrafine particle deposition. The exponential factors of geometric factor ratios, D and Q were determined by following the theoretical basis of turbulent diffusion in a circular, straight pipe, as discussed by Cheng et al. (1988). Based on this theory, the correlation between the particle penetration (p_p) and diffusion term in the straight pipe can be defined as shown in Equation (3.6):

$$\ln\left(\frac{1}{p_p}\right) = aQ^{-1/8}D^{2/3} \tag{3.6}$$

Due to the complicated structure of the monkey and human airways, it was necessary to redefine the power value of D and Q. Firstly, the power function of diffusion coefficient (D) was calculated by means of the relation shown in Equation (3.7):

$$\ln\left(\frac{1}{p_p}\right) = bD^h \tag{3.7}$$

After obtaining the h value, the power value of flow rate (Q) could be derived from the relation shown in Equation (3.8):

$$\ln\left(\frac{1}{p_p}\right)/bD^{0.545} = cQ^k \tag{3.8}$$

Based on these calculations, the power value of D and Q were estimated to be 0.545 and -0.298, respectively. The relation of the nano-sized deposition fraction and the diffusion term can be determined by means of Equation (3.9):

$$\eta = \left\{1 - \exp\left(-d \times D^{0.545} \times Q^{-0.298}\right)\right\} \tag{3.9}$$

As discussed above, in the current study, the geometric factors were integrated with the diffusion term to alleviate the differences in the structure of monkey and human airways. Therefore, equation 3.9 can be extended to include the geometric parameters. The model parameters were calculated based on the least square regression using Golden Grapher (Golden Software, LLC). The developed semi-empirical equations are shown below in Equations (3.10) and (3.11):

$$\eta_{\text{A/V-ratio}} = \left\{1 - \exp\left(-15.01 \times \left(\frac{A_{\text{Human}}/V_{\text{Human}}}{A_{\text{Monkey}}/V_{\text{Monkey}}}\right)^{-0.298} \times D^{0.545} \times Q^{-0.298}\right)\right\} \tag{3.10}$$

$$\eta_{\text{Amin-ratio}} = \left\{1 - \exp\left(-32.02 \times \left(\frac{A_{\text{min - human}}}{A_{\text{min - monkey}}}\right)^{-0.298} \times D^{0.545} \times Q^{-0.298}\right)\right\} \tag{3.11}$$

As shown in Figs 3.8b-c, the deposition fraction between the monkey and human airway models converged into a single S-shaped curve by adopting the new modified parameter. Following the two ratios of A_{min} and A/V, the deposition fraction displayed a similar shift, while the variation range was slightly different. This indicates that the two modified parameters can effectively reduce the impaction of diffusion term and the discrepancies in the structure of the airways. Based on these results, the deposition fraction in the human airway can be estimated from the structural factor ratios between the human and the monkey airways under study, along with the given inlet flow rate and the particle diameter. A reasonable integration of the geometric parameters with the diffusion term may aid in the research involving the extrapolation from monkeys to humans.

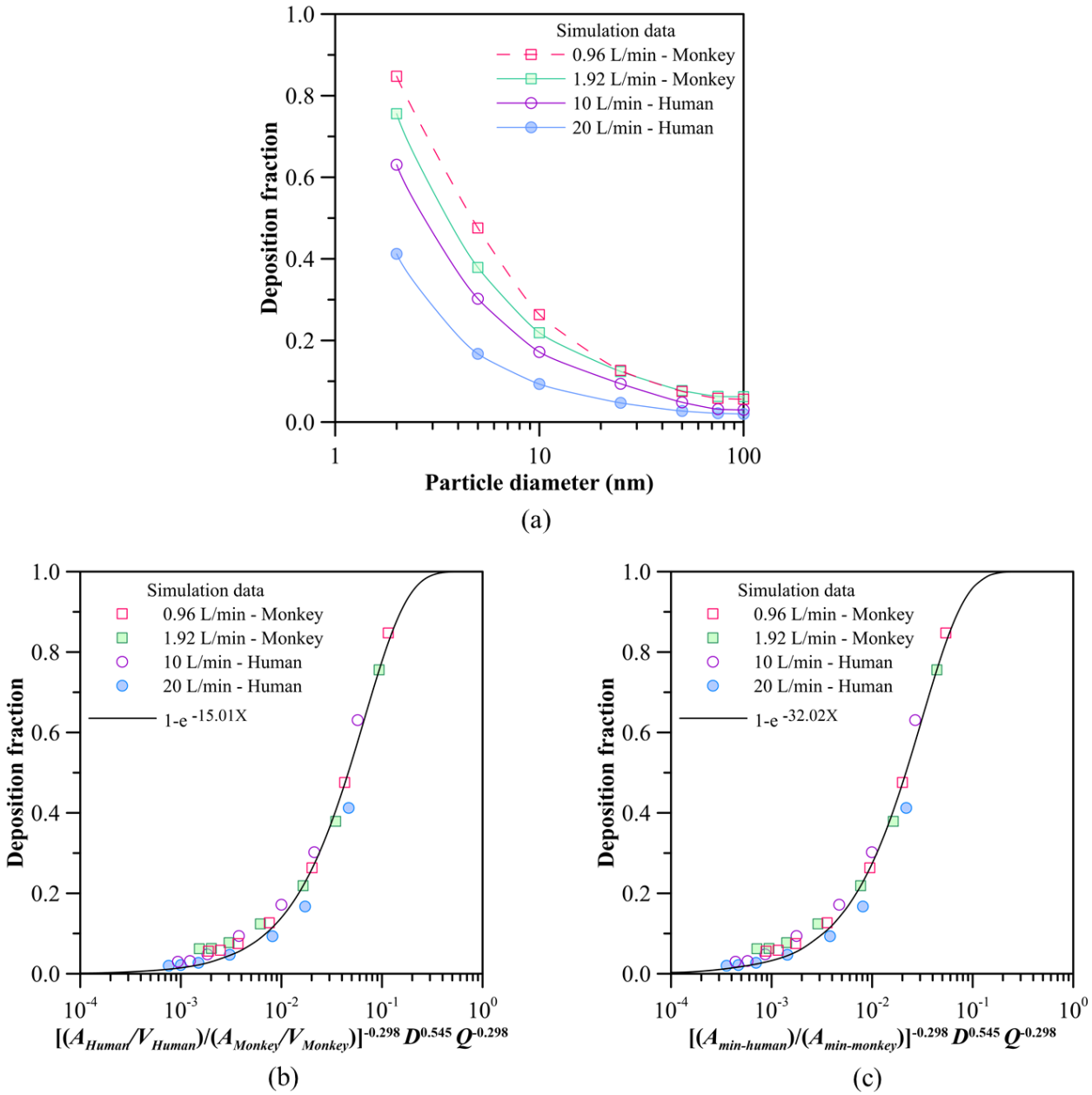

Figure 3.8: A comparison of the ultrafine particle deposition in the monkey and human airway models, as per the particle diameter (a) and modified parameters (b, c).

3.4.6. Regional deposition fraction and dispersion

The location of particle deposition in the airway might provide an overview of the potential sites of tumor formation and the penetration of ultrafine particles into the blood vessels or through the blood-brain barrier. Figure 3.9 shows the visualization of the deposition pattern of ultrafine particles at 5 nm and 100 nm, in four corresponding regions in both the airway models. The deposition of ultrafine particles was observed to follow an even distribution pattern in all the regions, especially in the ultrafine particle size of 5 nm. The current study observed that a majority of the ultrafine particles of size 5 nm were deposited in the nasal turbinate region (21%) of the monkey airway model, as shown in Fig 3.9a. The second highest deposition fraction (16%) was observed in the nasal vestibule and the valve region, compared to the other regions (nasopharynx–larynx and trachea region). Similarly, the difference in the deposition fractions among different regions of the airway model was also observed in the case of the ultrafine particle of size 100 nm (see Fig 3.9b). Although, the regional deposition fractions of the ultrafine particle of size 5 nm were observed to be greater than those of the ultrafine particle of size 100 nm. The remaining ultrafine particles of size 100 nm, which were unable to be filtered by the upper airway, were likely to be transported to the lower respiratory tract.

The deposition pattern of the human airway model is shown in Figs 3.9c-d. The Brownian force acting on the ultrafine particles led to the uniform diffusion on the surface of the airways. The current study observed a difference between the concentration of the deposited ultrafine particles of sizes 5 nm and 100 nm. As displayed in Figs 3.9c-d, most of the particles were deposited in the nasal turbinate region. Moreover, in each region of the models, the deposition fractions of the ultrafine particles of size 5 nm were higher than those of the ultrafine particles of 100 nm.

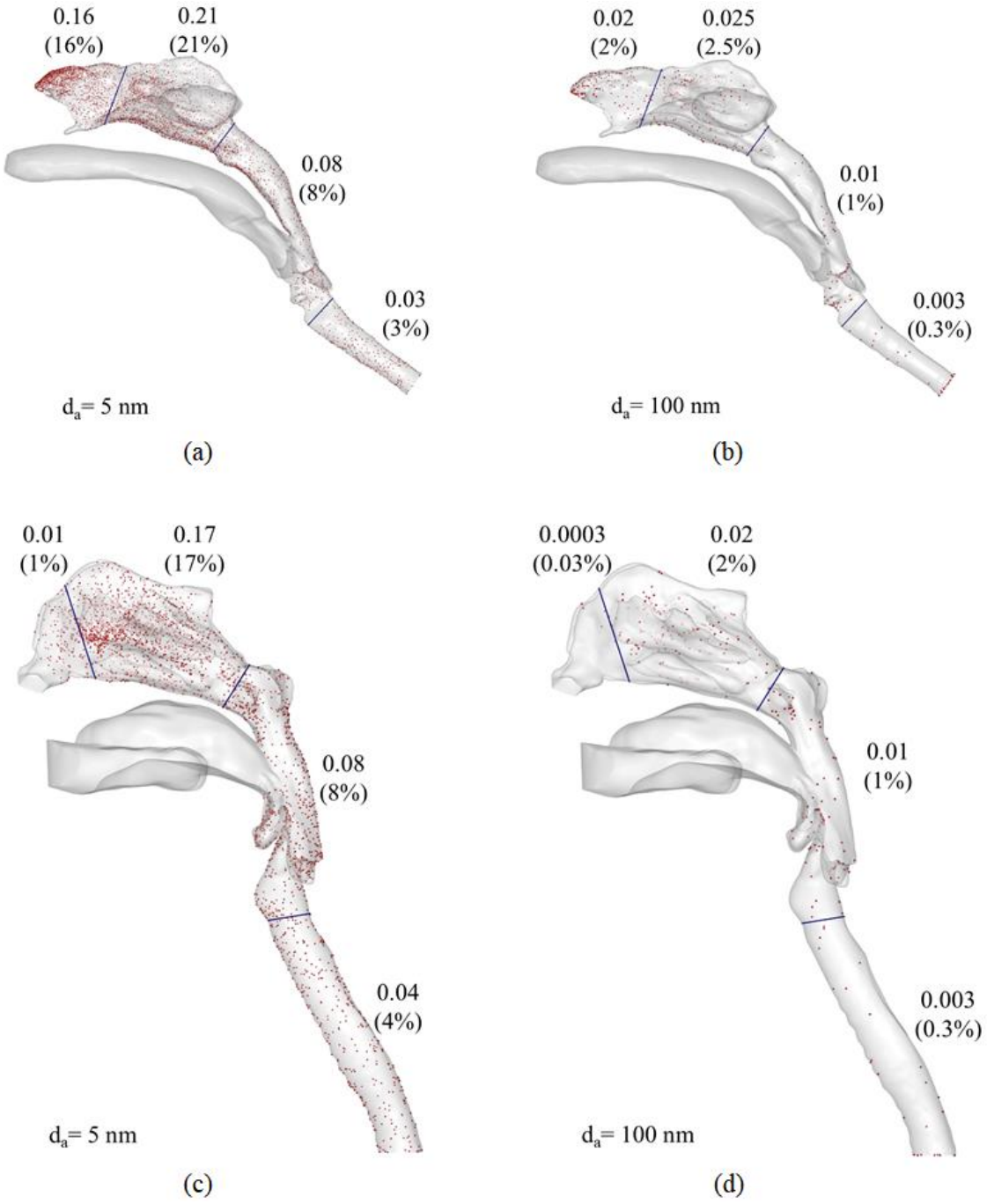

Figure 3.9: Three-dimensional visualization of particle deposition patterns in (a, b) the monkey airway model (Q_{in} = 0.96 L/min) and (c, d) the human airway model (Q_{in} = 10 L/min)

Local deposition fractions in the monkey airway model differed from those of the human airway model (see Fig 3.10). In the monkey airway model, significant deposition of ultrafine particles of size ranging from 5 nm to 100 nm was observed in the nasal vestibule and the valve. This correlates with the anatomy of the monkey model, which shows reverse flow in the vestibules, as described by Phuong et al. (2019); while the fraction of particles deposited in the nasal vestibule and the valve in the human airway model was almost negligible (remained less than 1%). The particle concentrations tended to be more uniform due to the diminished impact of the diffusivity as particle diameter increases (see the Stokes-Einstein equation) for both monkey and human models. Additionally, the current study recorded a reduction in the deposition of ultrafine particles of 5 nm and 25 nm, with an increase in the flow rates, in both models.

The particle concentration is illustrated in Fig 3.11 for both monkey and human airway models, showing the downward shift of particle concentration as particle diameter increases. The results showed that the highest concentration was recorded in the nasal vestibule and valve region of the monkey airway model (Figs 3.11a-b); it is attributed to the small area of this region. The particle concentration in this region at a 1.92 L/min inhalation condition was higher than that of the 0.96 L/min inhalation condition coinciding with the regional deposition fraction as shown in Fig 3.11. Due to the largest area, the particle concentration in the nasal turbinate region was considerably lower than that of the nasal vestibule and valve region for both inlet flow rates. The concentration in the two remained regions (nasopharynx-larynx and trachea) was almost similar at 0.96 L/min, while there were minor discrepancies among these regions in the case of 1.92 L/min. The particle concentration in the human airway model is described in Figs 3.11c-d; the very much larger regional area of the human airway model induces a significantly low concentration compared to the monkey airway model. As can be seen, the nasal turbinate is still the dominant region of particle dispersion at 10 L/min. However, the concentration of this region virtually concurred with the concentration of the nasopharynx-larynx region for the inlet flow rate at 20 L/min. Whereas the concentration in the nasal vestibule and valve was almost trivial since there is devoid of deposited particles in this region, especially in the case of 20 L/min. Beyond the nasal turbinate region,

the particle concentration in the nasopharynx-larynx and trachea region descended in order.

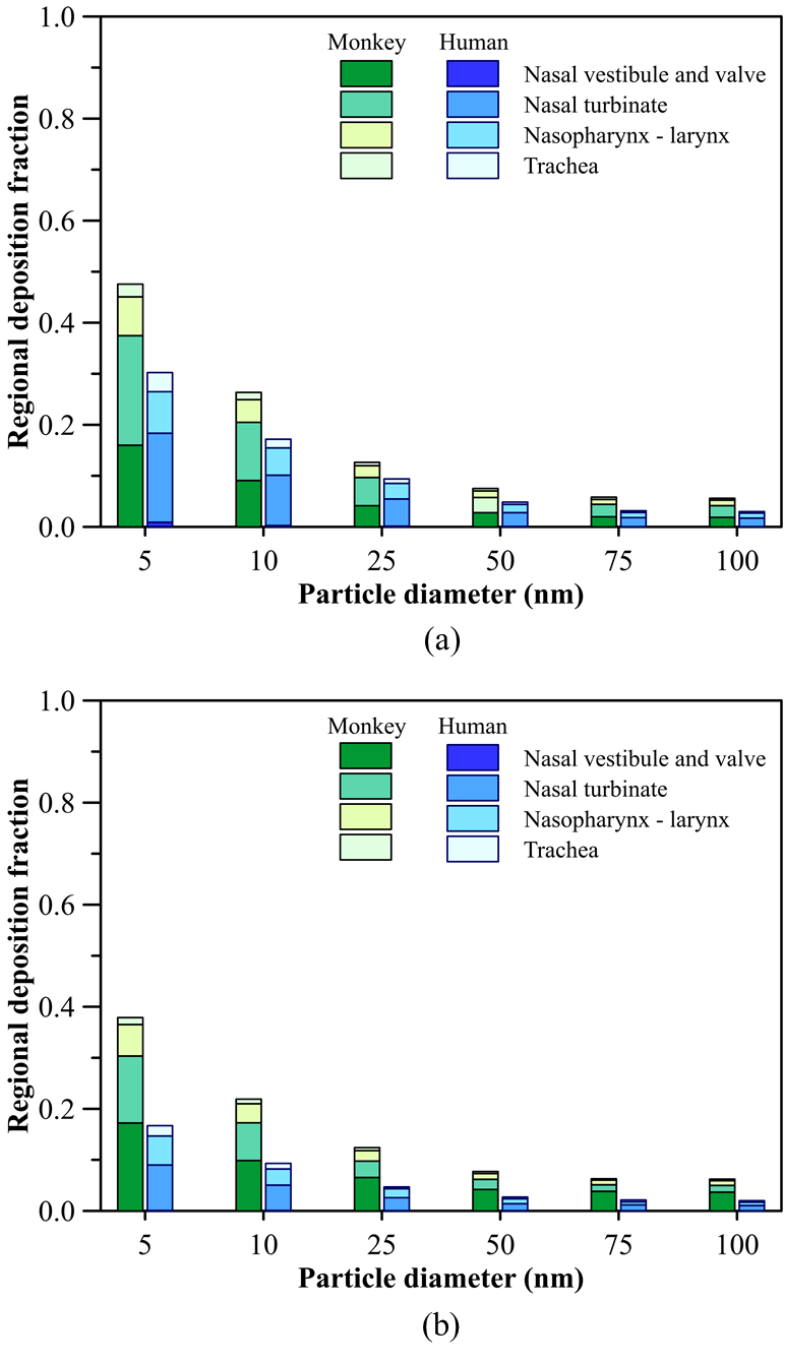

Figure 3.10: Regional deposition fraction in the monkey and human airway models under (a) the light and (b) moderate conditions, respectively.

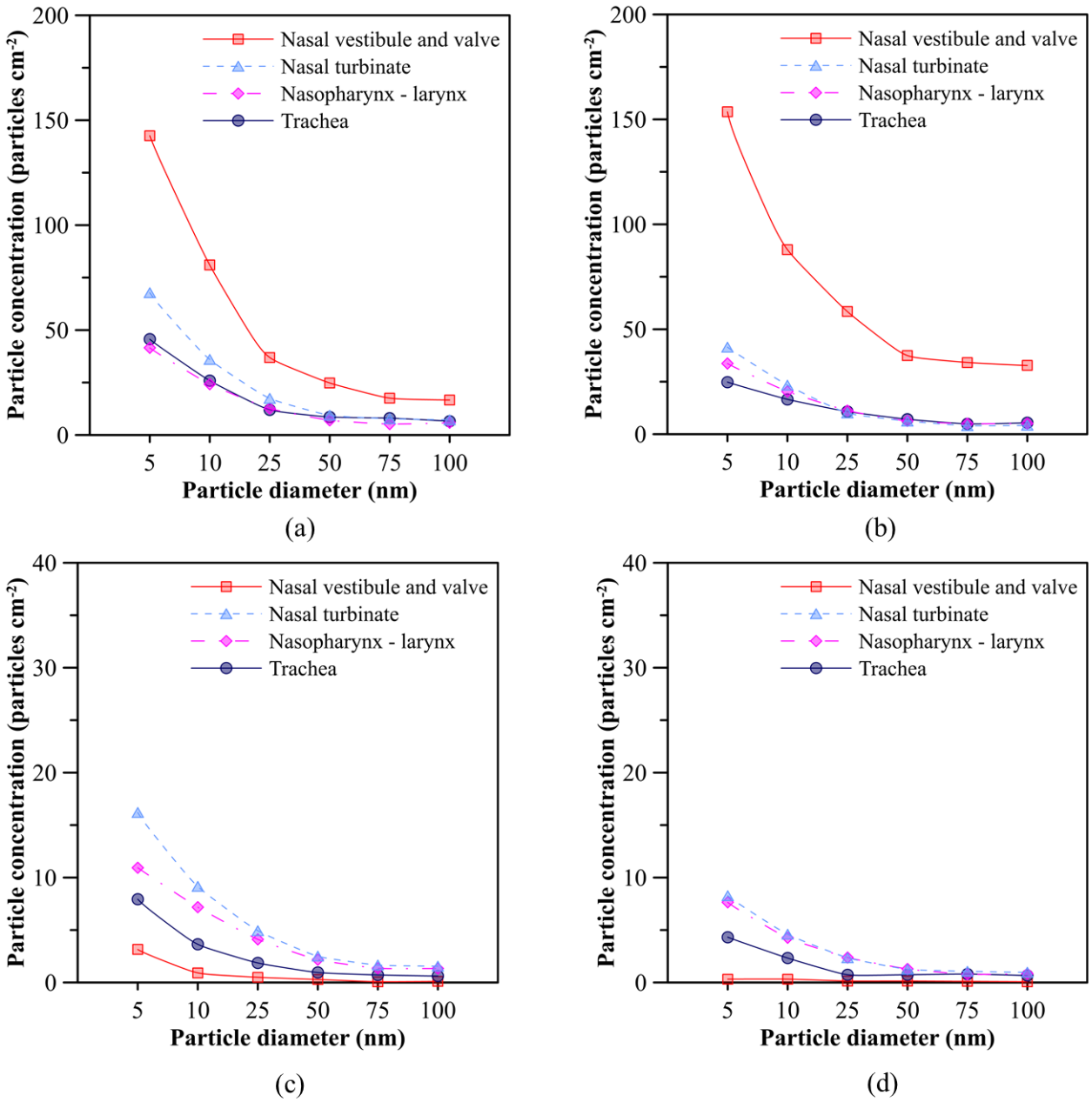

Figure 3.11: Particle concentration in the (a, b) monkey airway model (Q_{in} = 0.96 L/min and 1.92 L/min) and (c, d) human airway model (Q_{in} = 10 L/min and 20 L/min).

3.4.7. A summary of ultrafine to fine particles deposition

Data regarding the deposition of ultrafine particles, with a wide range of particle diameters, in the monkey and human airways may provide a general observation about the effect of deposition mechanism in the monkey and human airway models. Figure 3.12 depicts the deposition fraction curves of the ultrafine particles, with sizes ranging from 2 nm to 10 μm, in the monkey and human airway models. Data regarding the deposition of particles of size 1 μm to 10 μm in the human airway was calculated and validated using experimental data, obtained at inlet flow rate 10 L/min and 20 L/min, in a previous study published by the authors (Phuong et al. 2019). Also, in the aforementioned study, the micro-particle deposition fraction in the monkey airway model, at the inlet flow rate ranging from 2.2 – 6.9 L/min, was successfully estimated, which agreed well with the experimental data. Therefore, in the present study, we applied an identical method and model to perform the study of micro-particle transportation and deposition in the monkey airway for inlet flow rate at 0.96 L/min and 1.92 L/min.

The current study observed that the filter efficiency varied significantly with particle diameter and formed a U-shaped curve, as shown in Fig 3.12. In general, the deposition fraction was observed to attain the peak value with the smallest particle and sharply dropped down with an increase in the particle size. The deposition efficiency stability was observed to be maintained with the particles of size from 100 nm to 2.5 μm and then rapidly increased with particles of size greater than 2.5 μm. The coarse particles (> 2.5 μm) were greatly influenced by the inertial force. With the simultaneous increase in particle diameter and flow rates, the coarse particles were unable to adjust their pathway through the sudden bends and consequently collided with the inner wall of the upper airways rather than following the airstream. In the case of the ultrafine particles (< 100 nm), as discussed in the previous section, the Brownian motion became the dominant deposition mechanism instead of the inertial impaction. The deposition of ultrafine particles shifted and was inversely proportional to the particle size and inlet flow rate. The deposition fraction of the accumulation of particles (size ranging from 100 nm to 2.5 μm) remained under 0.10 (10%) in both models A and B. The mechanism of deposition of particles in the aforementioned size

range is the most difficult to explain. They are too large to be diffused by the Brownian force and still relatively small to be impacted by inertial force.

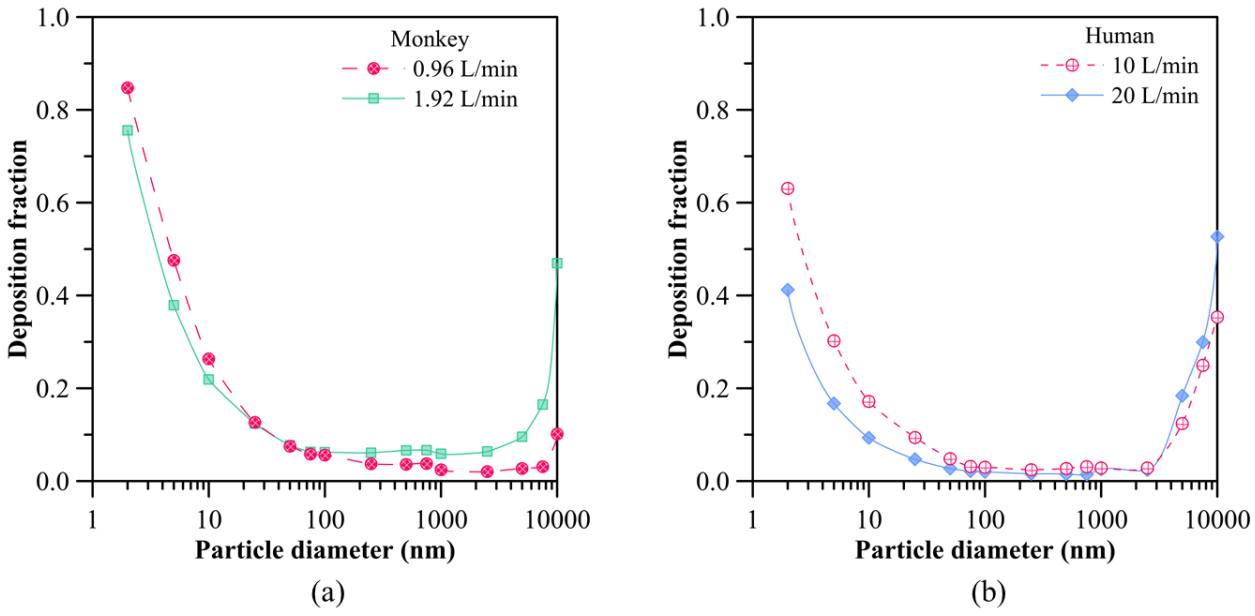

Figure 3.12: The deposition fraction of nano- and microparticles (size ranging from 2 nm to 10 μm) in the monkey airway model (a) and human airway model (b).

The previous published paper related to this chapter

Lu Phuong N, Dang Khoa N, Inthavong K, Ito K. 2018. Particle and inhalation exposure in human and monkey computational airway models. Inhal Toxicol. 30(11–12):416–428.

Dang Khoa N, Lu Phuong N, Ito K. 2020. Numerical modeling of ultrafine particle deposition in realistic monkey airway and human airway models: a comparative study. Inhal Toxicol. 32(7):311-325.

CHAPTER 4

NUMERICAL COMPARISON OF BREATHING FUNCTION IN NOSTRIL STENOSIS FRENCH BULLDOG AND AN EXAMINATION OF THE EFFICACY OF RHINOPLASTY

4.1. INTRODUCTION

Brachycephalic dogs, such as French bulldogs, English bulldogs, and pugs, have become increasingly popular in recent years (Emmerson 2014). The most common manifestations of brachycephalic obstructive airway syndrome (BOAS)-affected dogs are stenotic nares, elongated soft palate, hypoplastic trachea, and nasopharyngeal turbinates. The adverse health effects of BOAS diseases were mentioned in Chapter 1, which can impair the quality of their life. The primary abnormalities also lead to secondary lesions, including mucosal edema, everted laryngeal saccules, laryngeal collapse, and tonsil eversion (Aron & Crowe 1985; Ellison 2004; Riecks et al. 2007; Lodato & Hedlund 2012a; Meola 2013). Thus, BOAS can be considered a severe welfare consequence (Asher et al. 2009; Roedler et al. 2013); due to its symptoms can induce a shortened lifespan in brachycephalic breeds than those in mesocephalic and dolichocephalic breeds (Michell 1999; O'Neill et al. 2013; O'Neill et al. 2015). Indeed, in severe BOAS cases, dogs are almost unable to exercise or participate in heightened activities because they expend greater effort on breathing activities (Wiestner et al. 2007). Any minor aggravations can lead to respiratory distress, sudden fainting, or even death (Packer et al. 2015). Despite increased awareness of BOAS welfare issues among dog owners and the prevalence of brachycephalic breeds, quantifying how severely individual dogs are affected is challenging (Fasanella et al. 2010; Lodato & Hedlund 2012a).

In dogs severely affected by BOAS, surgical intervention is required when the restrictive breathing exceeds acceptable levels (Lodato & Hedlund 2012b). Liu et al. (2017) concluded that clinical signs of BOAS could be improved by surgery at an individual level. Clinically, all nostril stenosis cases that are not in the normal range will be generally judged as surgically indicated. Therefore, surgical treatment is

performed based on the severity of the external nostril stenosis. Nonetheless, the anatomical differences before and after surgical treatment removing the nose wing and winged fold tissue and the subsequent increase in external nostril area have not been fully elucidated in terms of respiratory physiology and fluid dynamics. Therefore, in this chapter, the CFD analysis, as discussed in Chapter 2, was applied to characterize the airflow patterns in dogs with BOAS with different degrees of stenosis. The efficacy of the surgical intervention was examined using models of a single French bulldog with severe stenosis that underwent rhinoplasty.

4.2. LITERATURE REVIEW

Several measurements are currently used to diagnose the clinical signs of BOAS in patient bulldogs, including physical examination, tidal breathing flow-volume loop (TBFVL), and barometric whole-body plethysmography (Bernaerts et al. 2010; Pardali et al. 2010; Liu et al. 2015; Riggs et al. 2019). Barometric whole-body plethysmography (BWBP) has been widely applied among these methods due to its non-invasive nature. Bernaerts et al. (2010) performed the BWBP to assess the respiratory function of eleven BOAS English bulldogs before and six bulldogs after the surgery. Their results indicated the lower expiratory time over inspiratory time ratio (Te/Ti) and higher peak expiratory flow of patient bulldogs than healthy bulldogs. The measured data also showed a significant improvement of respiratory variables after the surgery. Specifically, the peak expiratory and peak inspiratory flow ratio (PEF/PIF) was decreased; nonetheless, the authors generally concluded that some measured parameters, i.e., the ratio of peak expiratory and peak inspiratory flow and pause time, were still higher compared to healthy dogs. Liu et al. 2015 conducted the BWBP to characterize the BOAS clinical signs in French bulldogs with stenotic levels ranging from open to severe. The total number of bulldogs recruited in their study was eighty-nine BOAS bulldogs and 20 non-BOAS bulldogs. Eighty-nine BOAS bulldogs were classified into two groups, including BOAS+ (mild, moderate, and severe stenosis) and BOAS- (no BOAS-related clinical signs). The results obtained from their study suggested that the Te/Ti, PEF/PIF, and MV/BW (minute volume/body weight) parameters were higher than in the case of BOAS+ bulldogs

compared to BOAS- and non-BOAS bulldogs. Riggs et al. 2019 also performed the BWBP measurement to validate the exercise test (ET) for forty-four dogs, which were classified into four grades, including grade 0 or 1 – no or mild clinical signs of BOAS, grade 2 or 3 – moderate or severe stenosis. The ET included the five-minute walk and three-minute-trot; the results obtained from these two tests were compared with pre-ET. The authors concluded that there were fourteen grade 0 dogs out of twenty-three after the three-minute-trot test showing the BOAS-related clinical signs. Meanwhile, five grade 0 dogs had the BOAS-related clinical signs after the five-minute walk test. In grades 2 and 3, there was a potential for acute respiratory distress to develop during the ET. The general conclusion withdrawn from these previous studies suggests that the impaired respiratory functions in moderate and severe stenosis BOAS-affected dogs, while the clinical signs of mild or free stenosis dogs are acceptable, although they are still not comparable with these healthy bogs. Nonetheless, the precautions should be taken into account in case of mild or free nostril stenosis dogs due to the appearance of BOAS-related clinical signs after the exercise test.

To the best of the author's knowledge, the adverse effects of BOAS diseases have never been investigated using *in vitro* replica cast models of patient dogs; thus, resulting in the lack of quantitative experimental data describing the fluid patterns in the current literature.

The CFD technique has been applied to characterize the fluid flow distribution and airflow resistance in BOAS-affected dogs (Hostnik et al. 2017; Fernández-Parra et al. 2019). Hostnik et al. 2017 reconstructed the 3D numerical of twenty-one English bulldogs from their CT data and simulated the airflow patterns. Their results suggest that the high airflow resistance occurred at the third rostral region of the upper airway, and the surgical effort to reduce the airflow resistance would be solely performed in this region. Also, the discrepancies in the airway pressure between the left and right nasal passages were recorded in their study, which may be a consequence of nasal septal deviation. Moreover, their data can be helpful for surgeons, which may minimize the trauma during and after surgery. Recently, Fernández-Parra et al. 2019 included a total of nine different dog breeds. Their results suggest that the airflow resistance in the

case of brachycephalics dog breeds was higher than that of mesocephalic and dolichocephalic dog breeds. Furthermore, the simple resection of the external nares is insufficient to correct the basic problem of BOAS-affected dogs. Another CFD numerical effort was made by Craven et al. (2010) to characterize the sniffing function in canines. The 3D numerical model of a 29.5 kg female Labrador retriever canine was reconstructed from an MRI image. The authors concluded that the olfactory recess played an essential role in odorant deposition, and the olfactory acuity of a dog appears to depend on its nasal airway passage structure mainly. From the literature review, the numerical research work involving the fluid flow in dog breeds is scarce; especially, the quantitative study about the effects of BOAS disease on the breathing function of dogs.

4.3. MATERIALS AND METHODS

4.3.1. Grid design of the upper airways of French bulldogs

The 3D geometry models of French bulldogs were reconstructed based on their CT data sets by using 3D slicer software as discussed in Chapter 2, section 2.4.1. The computational models were discretized and meshed using ICEM-CFD (ANSYS Inc.) with hybrid mesh, including the tetrahedral mesh elements and ten prismatic layers, as shown in Fig 2.14 (Chapter 2, section 2.4.2). A refined mesh of approximately 0.005 mm was used as the height of the first prismatic layer at the wall surface in the nasal passage and nasal cavity to resolve the flow profile inside the viscous sub-layer. The complicated inner geometries of the frontal sinuses were also carefully constructed. The dimensionless wall distance y^+ was controlled, ranging from less than 0.1 to around 1, depending on the morphometric features and flow field of each model. Grid independence was performed with scalar velocities along Line 1 (Fig 4.1). To balance the computational cost and accuracy, a hybrid mesh size of 9.6 million was selected. Due to the heterogeneity of the airway morphometry, the numbers of independent mesh elements for all models ranged from 9.15 to 9.91 million, as shown in Table 4.1. The maximum skewness was less than 0.9, and the minimum orthogonal quality was higher than 0.02 in all airway models. The maximum skewness and minimum orthogonal quality value were controlled to meet the standard of ANSYS Fluent software

(maximum skewness for tetrahedral mesh should be kept below 0.95, and the minimum orthogonal quality should be over 0.01).

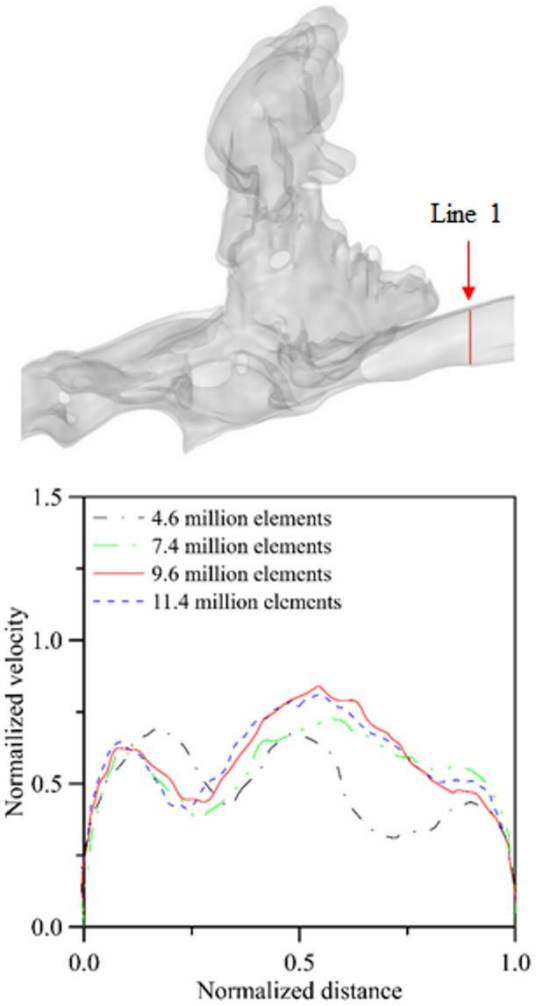

Figure 4.1: Grid independence check in model A under light breathing conditions. A total of four sets of tetrahedral mesh was built with different numbers of elements. The velocity profile was extracted from Line 1 and normalized to the inlet velocity. The distance was normalized to the length of the line.

Table 4.1. Details of the grid design in the French bulldog upper airway models

Model	Maximum mesh size (mm)	Number of prism layers adjacent to the wall	Number of elements (million)
A	0.39	10	9.59
B	0.32		9.51
C	0.35		9.84
D	0.32		9.15
E	0.32		9.91
F	0.31		9.67
G	0.31		9.53
H	0.38		9.68
H1			9.73

4.3.2. Airflow analysis inside the upper airways of French bulldogs

The flow field was modeled using the low-Reynolds type k–ε turbulent model (Abe–Kondoh–Nagano model), as detailed in Chapter 2, section 2.3.1. A steady and constant flow rate was used for the breathing condition as a function of metabolic rate, which was calculated by using the ratio of body weight (BW) and minute volume (MV) described by Liu et al. (Liu et al. 2015). Detailed information is summarized in Table 4.2. A constant negative velocity was set at the end of the trachea outlet of the upper airway model. The hydraulic diameter of the trachea opening was defined as the characteristic length scale of the model. The wall treatment was assumed to be a no-slip condition during the simulation process. The semi-implicit method for pressure-linked equations (SIMPLE) algorithm was used for pressure-velocity coupling; a second-order upwind difference scheme was used for the convection terms; and a central difference scheme was used for the remaining terms. A summary of the numerical conditions is given in Table 4.3.

Table 4.2. Inlet flow rates of the upper airways

Stenosis level	Model	Weight (kg)	MV/BW[a] (L/kg)	Flow (L/min)	
				Light	Moderate
Open	A	13.1	0.2137	5.6	11.2
	B	8.7		3.7	7.4
Mild	C	12	0.2154	5.2	10.4
	D	9.8		4.2	8.4
	E	12.4		5.3	10.6
Moderate	F	13	0.2415	6.3	12.6
Severe	G	10.2	0.2415	4.9	9.8
	H	12.7		6.1	12.2

[a] The ratio between the mean minute volume (MV) and the bulldog body weight (BW), which were defined following Liu et al. (Liu et al. 2015).

Table 4.3. Numerical and boundary conditions

	French bulldog upper airway models
Turbulent model	Low-Reynolds type k-ε model (Abe Kondoh Nagano)
Grid style	9.15-9.91 million elements (Unstructured, Hybrid mesh)
Outflow boundary (Trachea opening)	Case 1: Light breathing: Q = 3.7 – 6.3 L/min Case 2: Moderate breathing: Q = 7.4 – 12.6 L/min TI= 10%
Inflow boundary	Gradient zero condition for all parameters at the nasal opening
Wall treatment	Velocity: no slip

4.4. RESULTS AND DISCUSSIONS

4.4.1. Morphometric features of the upper airways of French bulldogs

The upper airway morphometry of each French bulldog is depicted in Fig 4.2. Models A and B were two different bulldogs without BOAS-related clinical signs or defined as healthy nose cases (Figs 4.2a-b). The geometric characteristics of individual brachycephalic dogs with mild (Model C, D, and E), moderate (Model F), and severe (Model G, H) stenosis are shown in Figs 4.2c-h, respectively. The upper airway models were separated into five main regions based on the morphometric shifts in the transverse planes. These were the external nares, the maxillo-turbinate, the ethmoid-turbinate, the frontal sinuses, and the nasopharynx (Schreider & Raabe 1981). As shown in Fig 4.2, the open and mild stenosis cases exhibited airway features present and clearly described; meanwhile, the geometric features in the external nares and maxillo-turbinate regions were seriously malformed in moderate and severe stenosis bulldogs (as circled in Figs 4.2f-h). This was characterized by a significant occlusion of the airway, resulting in a small tube-like airway formation. From a fluid dynamics point of view, a reduced cross-sectional area for a given flow rate leads to increased flow velocity. Therefore, the significant reduction in the cross-sectional airway from the stenosis impacts the breathing function of the bulldogs. Besides, the lack of frontal sinuses observed in models B, D, E, F, and G due to the available CT image data; nonetheless, this geometric feature did not affect the overall flow behavior.

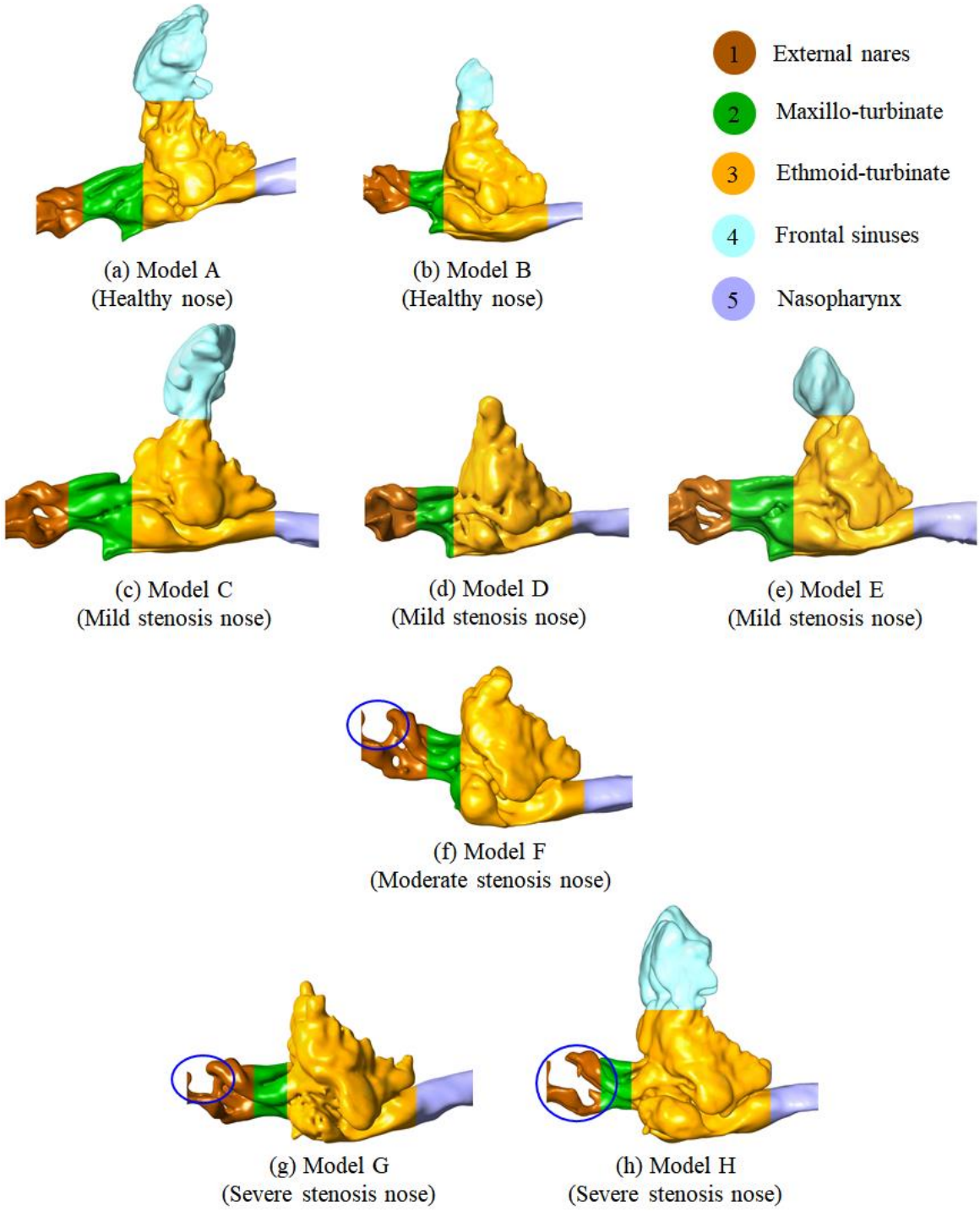

Figure 4.2: Geometry of the reconstructed CT-based geometry of the French bulldog upper airway models. The models were separated into five main regions following Schreider and Raabe (1981), including 1-External nares; 2-Maxillo-turbinate; 3-Ethmoid-turbinate; 4-Frontal sinuses 5-Nasopharynx.

The shape of the external nostrils was preserved close to its realistic form, as depicted in Fig 4.3, a comparison between real and artificial nostrils. The specific characteristics of the external nostril shape were maintained to obtain the results as close to reality as possible. These results evidenced that the serious malformed of the airway structure due to BOAS disease can be detected by physically examining the external shape of the nostrils. As showed in Fig 4.3, the external shape of the nostril in cases of two healthy noses (Model A and B) was fully open, and the external nostril shape of mild stenosis (Model C, D, and E) did not show any significant discrepancies compared to healthy noses. Therefore, the intranasal structure was similar in these cases, as discussed above. However, the external nostril shape of moderate stenosis case (Model F) demonstrated the apparent difference, in which the upper parts of the nostrils were almost closed (as marked by a red circle). The tightness of the external nostrils became more serious in cases of severe stenosis (Model G and H); specifically, almost all the nostrils were closed, and only a small portion in the bottom part was still opened. Therefore, the primary purpose of the surgery is to open the closed external nostrils, as shown in Fig 4.3i. These results can deliver the bulldog's owner, who does not have expertise in the field of veterinary, a general assessment about their dog's health status as early-stage; thus, timely responses can be conducted to avoid further lesions.

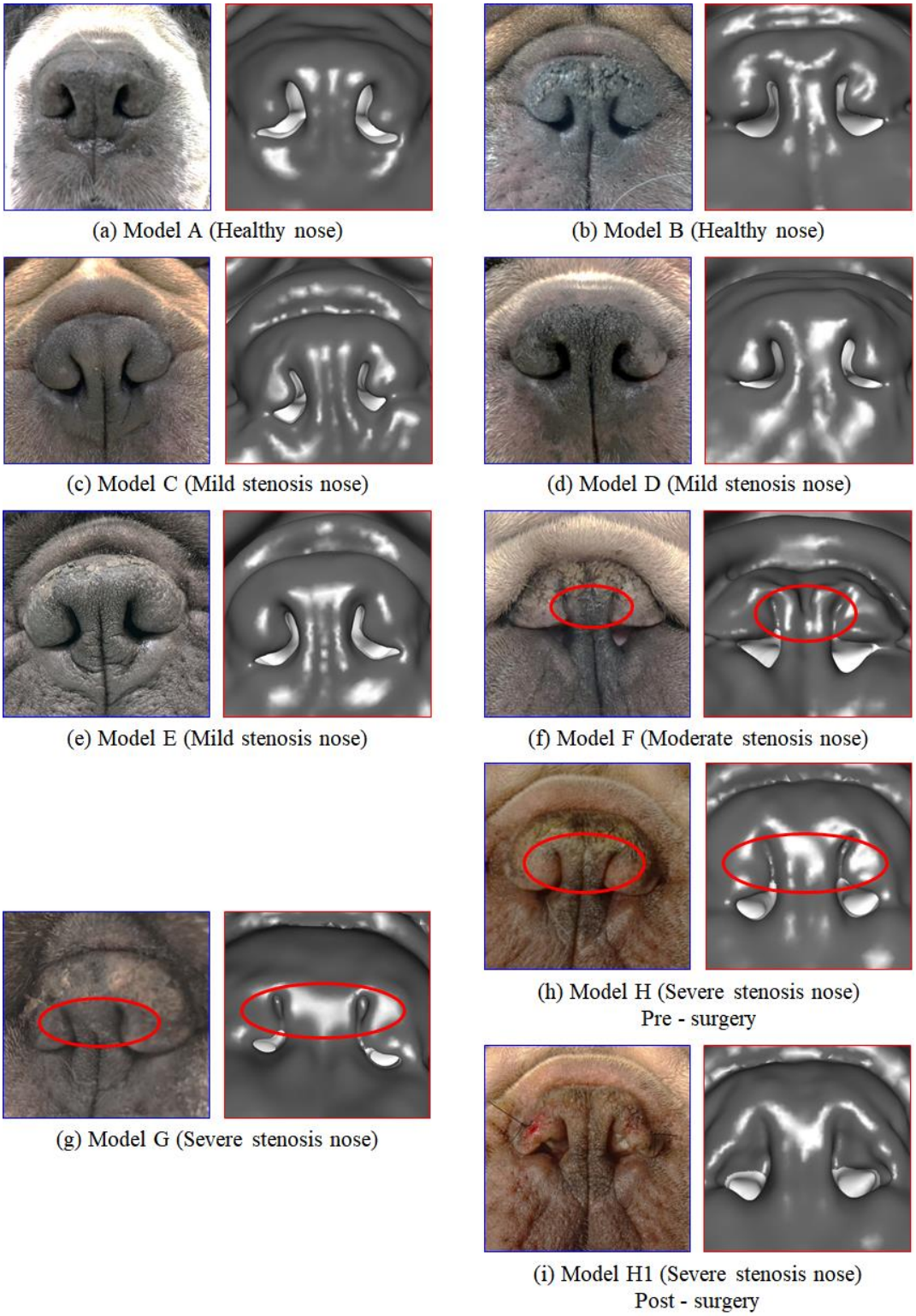

Figure 4.3: The external shape of the inlet nostrils of the reconstructed model compared to the real figures. The nostril shape was adapted from the computed tomography (CT) image to precisely describe the inlet airstream through this region.

Over time, the primary component of BOAS (stenotic nares) weakens more rigid structures nearby and can eventually lead to secondary changes such as the palate and laryngeal edema, saccule, and tonsil eversion, and laryngeal collapse (Meola 2013). Therefore, surgical intervention is necessary to improve ventilation through the nasal route and prevent further negative secondary effects. In this study, the most severe stenotic bulldog case (model H) underwent surgery, and the geometric features of the pre and postoperative cases are shown in Fig 4.4. In this study, the wedge resection was performed in the 5-mm region from the external nostrils. As shown in Fig 4.4a, the six transverse planes were created at the surgical region in both pre-and post-surgery models. The transverse plane 1 describes the shape of external nares; after the surgery, the closed upper part was enlarged. The further inward, the airway enlargement became negligible, and the geometric structure was similar from the transverse plane 6 to the caudal airway in both pre-and postoperative. The area of the transverse planes is depicted in fig 4.4b; the dashed line represents the transverse plane area in the preoperative case, while the solid line denotes that of the postoperative case. From the plotted results, the area of transverse plane 1 was 49 and 90 mm2 in pre-and post-surgery, respectively, which indicates an approximate 84% expansion in the external nostrils region and gradually decreased to around 7% at transverse plane 6. These results confirm that the opening region was affected by the surgery; apart from this region, the rest of the airway between pre-and postoperative was completely homogeneous in morphometric features.

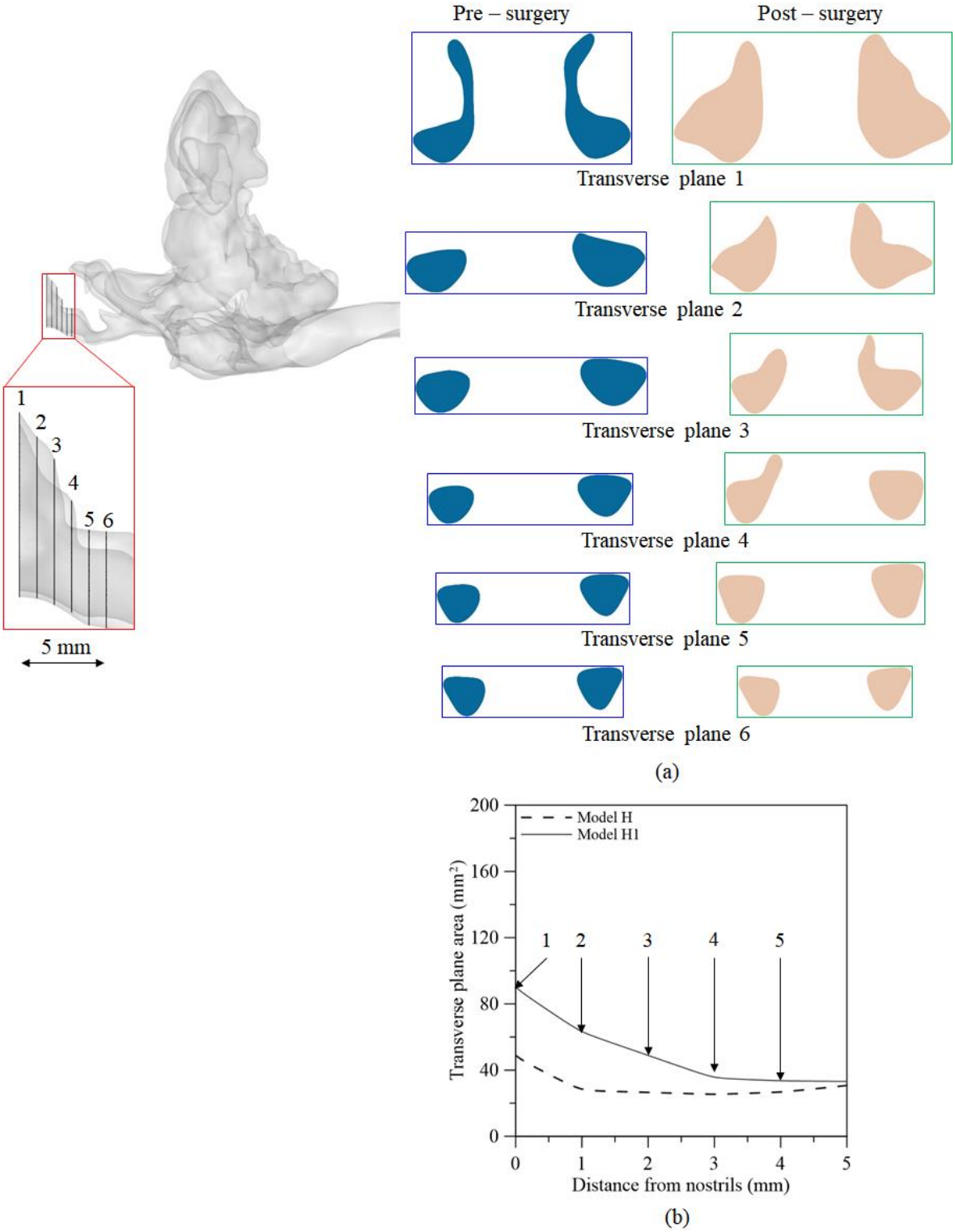

Figure 4.4: Geometric features of the operated region of a pre-(model H) and postoperative bulldog (model H1). (A) The surgery was conducted in the 5-mm region from the nostril inlet. (B) The transverse plane area increased after the surgery.

4.4.2. Characterization of the airstreams in the upper airways of French bulldogs

The velocity streamlines inside the bulldog upper airways are shown in Fig 4.5, representing the airflow distributions during inspiration under light breathing conditions. Normalized velocity was applied to avoid discrepancies in individual inlet flow rates, allowing comparisons between different models. The velocity map describes the key flow regions, where red and blue indicate peak velocity and low-velocity regions. The inhaled air enters the nostril, accelerates significantly in the dorsal meatus, and quickly passes through the external nares and maxillo-turbinate regions (Fig 4.5). The airstream rapidly reaches the ethmoid-turbinate region, where it begins to deaccelerate and swirl, also observed in previous studies (Fig 4.5) (Craven et al. 2010; Rygg et al. 2017; Fernández-Parra et al. 2019). The airstream continuously penetrated the posterior regions of the airway through the nasopharynx region.

After entering the nostril inlet, the velocity magnitude increased slightly in the dorsal meatus in model A (Fig 4.5a); negligible for model B (Fig 4.5b), but significant for the bulldogs with mild stenosis (Figs 4.5c-e), and particularly for model E. However, in general, the simulation results revealed that the airflow characteristics of BOAS dogs with mild stenosis did not differ from those of healthy dogs. The acceleration discrepancies in several specific regions can be attributed to the heterogeneity of the airway structure. Therefore, surgical intervention can be postponed in bulldogs with mild stenosis; however, the owners should keep their dogs lean to avoid exacerbating the clinical symptoms. The abnormalities in the external nares region led to varied flow acceleration due to the airway constriction for the moderate to severe stenosis models (Figs 4.6a-c). The peak velocity magnitude in the moderate and severe stenosis models was almost two to three times higher than that of the bulldogs with none or mild stenosis. In the posterior regions, the velocities were relatively low for the moderate and severe stenosis cases. The high-velocity flow has been associated with the breathing effort of the dogs, indicating insufficient pulmonary ventilation (Mutlu et al. 2015). This hypoxia phenomenon can lead to fainting and overheating during the summer season, especially during motive activities. These dogs would pant (rapid inhalation through the mouth), leading to inadequate saturated air. Consequently, dogs may experience increased metabolic

energy and poor thermal regulation as the nasal mucosa is the primary site for the saturation and humidification, rather than the oral surfaces and the tongue (Schmidt-Nielsen et al. 1970). Therefore, further investigation of impaired air conditioning in BOAS-affected bulldogs is required.

In the post-op case (Fig 4.6d), the surgery did not affect the geometric features of the constricted position; thus, the high-velocity still remained at this position, and the general distribution in the posterior region was similar to that in the pre-surgery case (Fig 4.6c). These results indicate that the recent surgery could not reduce the total peak velocity in the airway of patient bulldogs; in order words, the local lesions that may be exerted by the extreme air-jet still exist after the surgery.

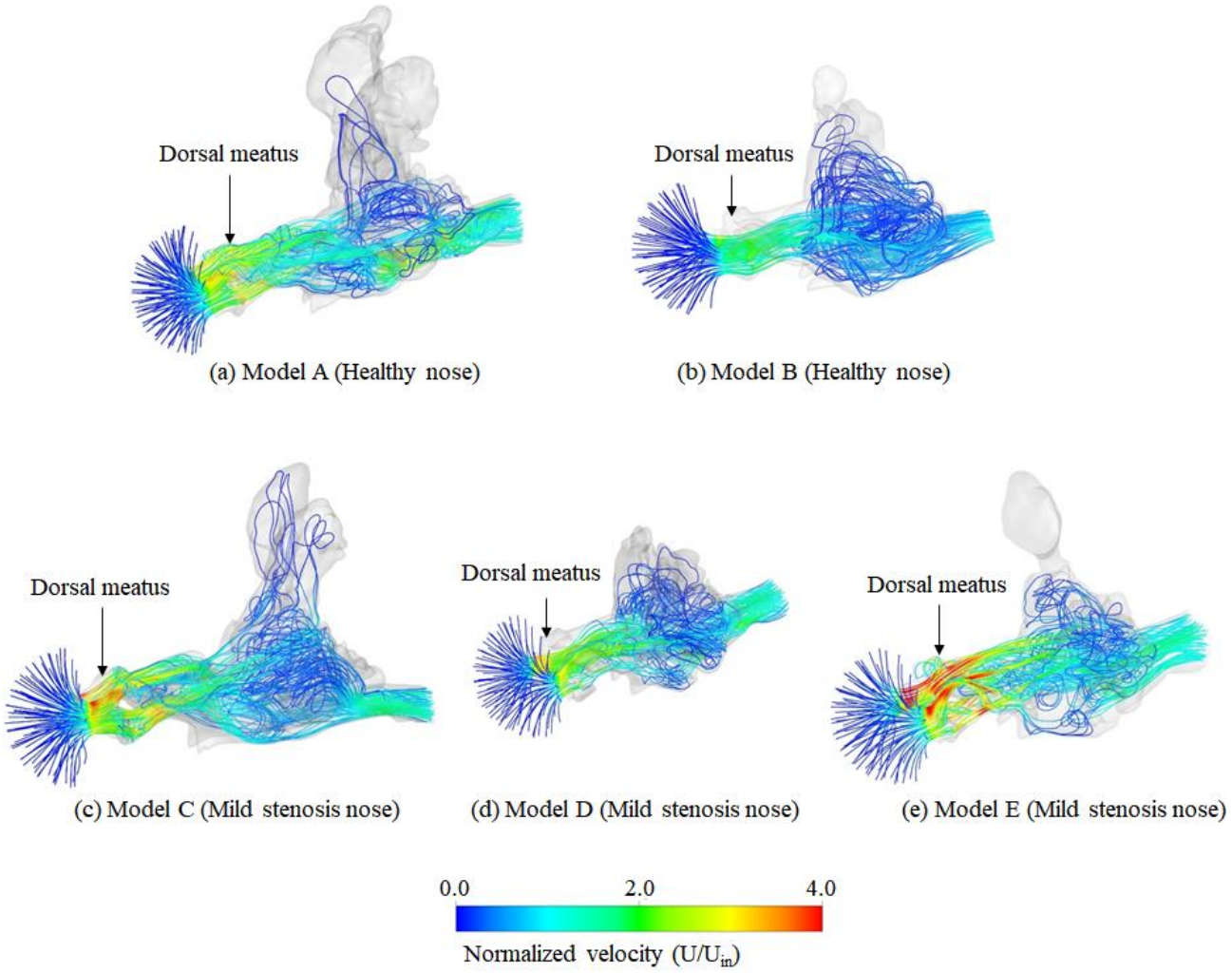

Figure 4.5: Airflow streamlines in the upper airways of French bulldogs. Streamlines depict the relative volume of air passing through the upper airway models. The velocity magnitude was normalized by each model's maximum velocity, where the colormap has red denoting high velocity and blue indicating low velocity.

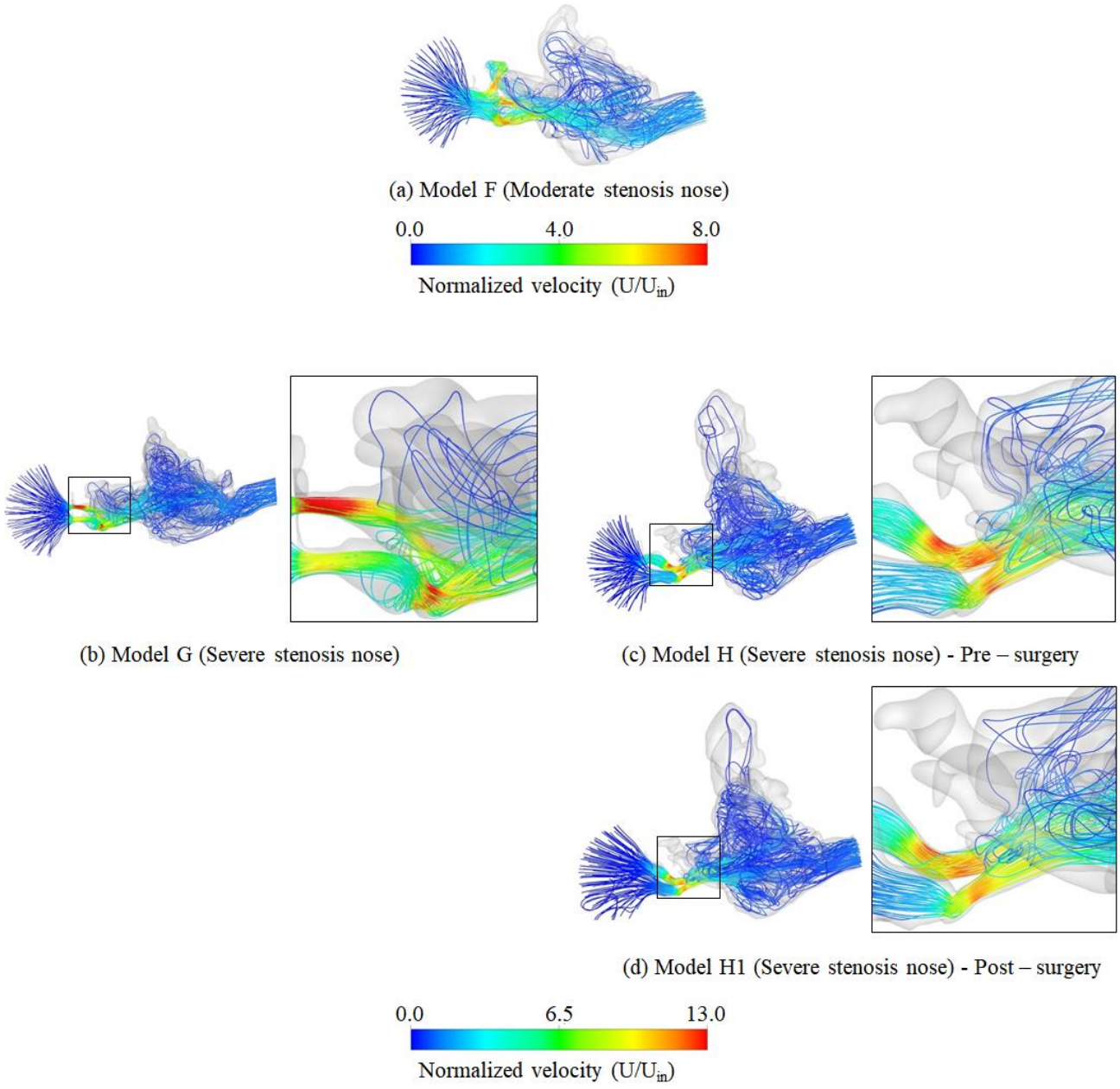

Figure 4.6: Velocity streamlines through the upper airway of moderate and severe stenosis French bulldogs. The velocity magnitude was normalized by each model's maximum velocity, where the colormap has red denoting high velocity and blue indicating low velocity.

Although the total peak velocity remained after the surgery, a change in velocity magnitude was observed in the surgical area, where the velocity was significantly reduced due to the nostril widening (Fig 4.7). Specifically, the averaged velocity magnitude decreased by approximately 46% in transverse plane 1 and up to 51% in transverse plane 2, and then 19% at transverse plane 5 (Table 4.4). In transverse plane 6, the averaged velocity levels were comparable between pre-and post-surgery. These results indicate that the surgery appeared to have failed to enhance ventilation via the nasal passages, especially at the constricted site. Nonetheless, the surgical enlargement of the external nostrils showed considerable improvement in the operative region by increasing the accessibility of the external nares region to the ambient air; therefore, mitigating the high velocity at the nostril inlet region. This improvement can reduce the potential development of secondary lesions in the airways and decrease snoring volume (Aron & Crowe 1985).

Table 4.4. Normalized averaged velocities pre and postoperatively during light breathing conditions

	Normalized averaged velocity	
	Pre-surgery (Model H)	**Post-surgery (Model H1)**
Transverse plane 1	0.93	0.50
Transverse plane 2	1.65	0.81
Transverse plane 3	1.77	1.11
Transverse plane 4	1.85	1.44
Transverse plane 5	1.74	1.41
Transverse plane 6	1.48	1.53

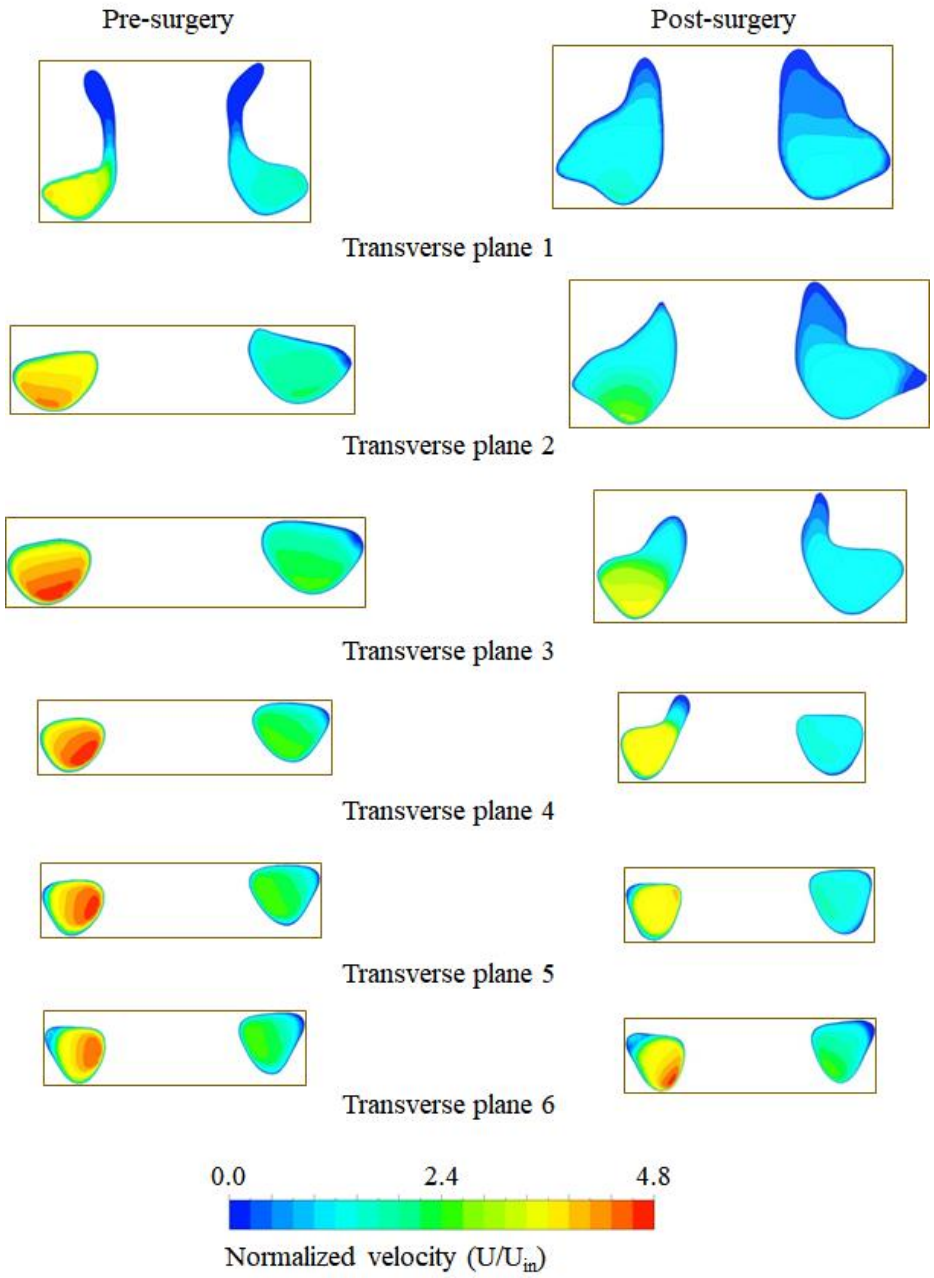

Figure 4.7: Normalized contour velocity in the transverse planes in the pre and postoperative models (H, H1). The representative planes describe the airflow characteristics in the surgical region. The color represents the velocity magnitude, where red indicates high velocity and blue indicates low velocity. The contours also indicate airflow distribution through the airway passages.

4.4.3. Pressure distributions along the upper airways of the French bulldogs

The pressure distribution through the upper airway models was evaluated by calculating the mean static pressure at each transverse plane at 4-mm intervals from the nostril inlet shown in Fig 4.8 for all inhalation flow rates (light and moderate conditions). The five main regions (1-External nares, 2-Maxillo-turbinate, 3-Ethmoid-turbinate, 4-Frontal sinuses, and 5-Nasopharynx) defined in Fig 4.2 were labeled 1 to 5 in the figure with respect to the distance from the nostrils.

In general, the mean pressure in healthy bulldogs (models A and B) was lower than in those with mild stenosis (models C and E). At the nostril inlets (x = 0 mm), the pressure values of models A and B were 8.1 and 10.5 Pa, while those of models C, D, and E were 13.9, 7.5, and 15.1 Pa, respectively, during light breathing. Meanwhile, the mean pressure values at the nostril inlet during moderate breathing were 28.5 and 36.7 Pa in models A and B and 41.4, 16.1, and 45.9 Pa in models C, D, and E, respectively. Figures 4.8a-b show the pressure change was similar in the open and mild stenosis cases where high pressure was observed at the nostril inlets and gradually decreased as air passed through the external nares region. The mean pressure was relatively constant in region 2 and the anterior part of region 3 before reducing slightly toward the end of regions 3 and 5. The high pressure in the nostril inlet region can be attributed to the stagnation of airstream at this region before passing through the narrow external nares in open and mild stenosis bulldogs.

Figures 4.8c-d depict the pressure distributions in the upper airways of bulldogs with moderate and severe stenosis. The exceptionally high pressures at the nostril inlet decreased significantly in the external nares regions. Thereafter, the pressure was almost constant for the moderate and severe cases (after 20 mm in Figs 4.8c-d), which differed from the healthy and mild stenosis cases (after 20 mm in Figure 4.8a-b), and this was observed for both inlet flow rates. Pressure at the nostril inlet varied considerably between the bulldogs. The highest pressure values were observed in model H at approximately 351 Pa and 1,398 Pa under light and moderate breathing conditions, followed by model G with peak pressure values of 236 Pa and 941 Pa, respectively. For the moderate stenosis case (model

F), the peak pressure was much lower at 75 Pa and 297 Pa for light and moderate breathing conditions, respectively. The high pressure exhibited in the moderately and severely affected bulldogs can be attributed to the obstructed position. The data showed the negative pressure and non-uniform pressure distribution at the constriction point in severely affected stenosis bulldogs. In contrast, the pressure in the anterior part of the congested area was remarkably higher than in the posterior region. These results indicate that the local pressure rapidly increases at the anterior region of the congested site. To reduce this pressure build-up, enlargement of the congested site is necessary. The pressure distribution plots demonstrate the ability to locate the effective surgical sites that would facilitate surgical intervention.

In the post-op model (model H1), the peak pressure decreased by 4% and 7% (to approximately 337 Pa and 1,300 Pa) for light and moderate breathing, respectively, compared to the pre-op model (model H). The pressure distribution for the pre-and post-op models was similar after the nostril inlet region.

Figure 4.9 shows the surface pressure contour in the upper airway under light breathing conditions. The red and blue colors represent high and low pressure, respectively. The results correlate with the mean pressure profiles, given in Fig 4.8. The high-pressure region was observed at the ventral meatus of the external nares region in models A – E (Figs 4.9a-e), while extremely high pressure was recorded over the entire external nares just before the obstruction position (Figs 4.9f-h). The pressure distribution of the postoperative case was similar to the preoperative case (Fig 4.9i).

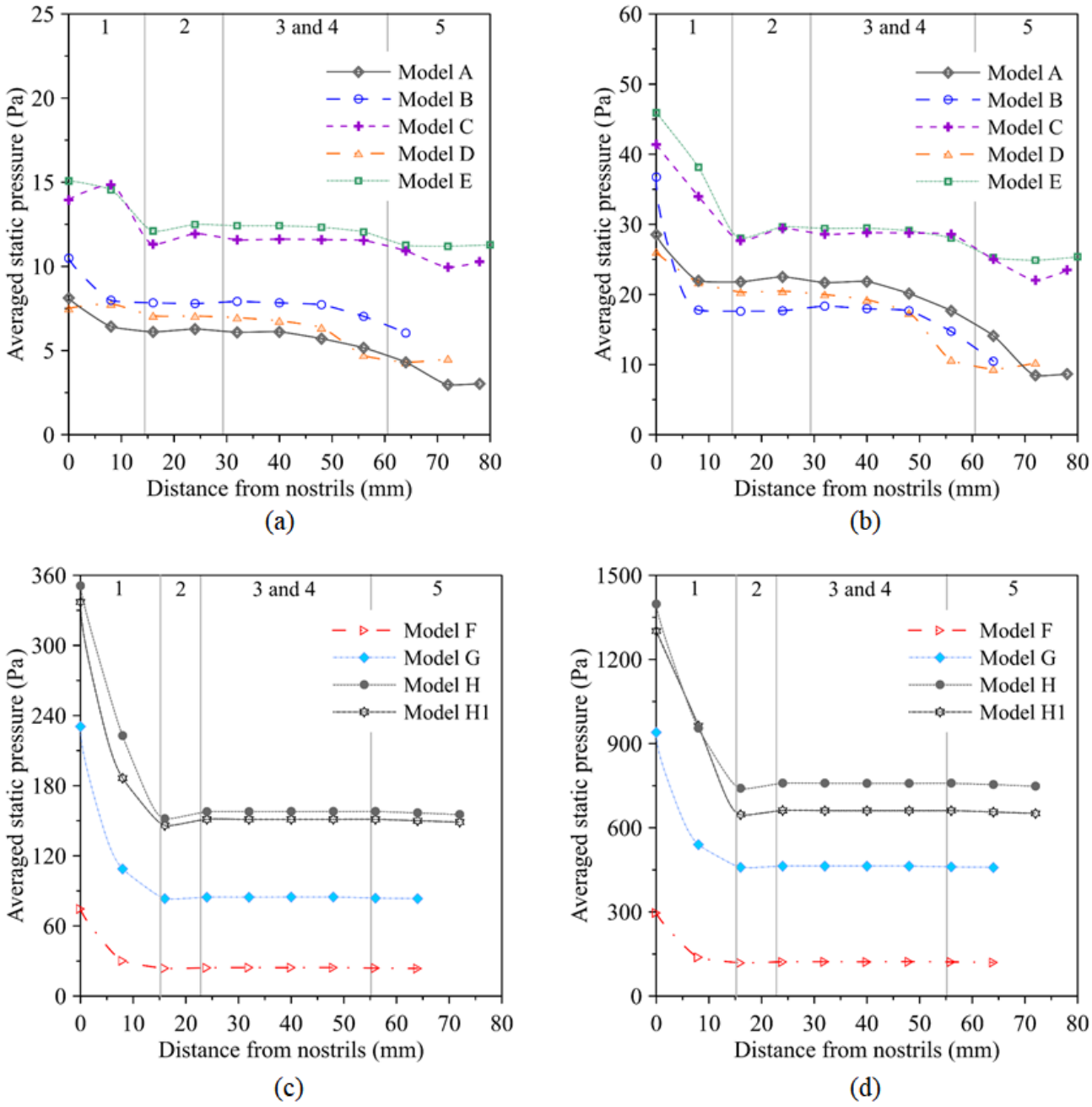

Figure 4.8: Averaged static pressure fluctuation in French bulldog upper airways. The pressure variation in healthy and mild stenosis nose at (a) light breathing and (b) moderate breathing conditions, and the pressure distribution along the upper airway of moderate and severe stenosis bulldogs at (c) light breathing and (d) moderate breathing conditions. The numbers 1 to 5 at the top of each figure denote the sub-regions classified in Fig 4.2. The scattered lines indicate the average static pressure at each transverse plane along the upper airways with a distance of 4 mm.

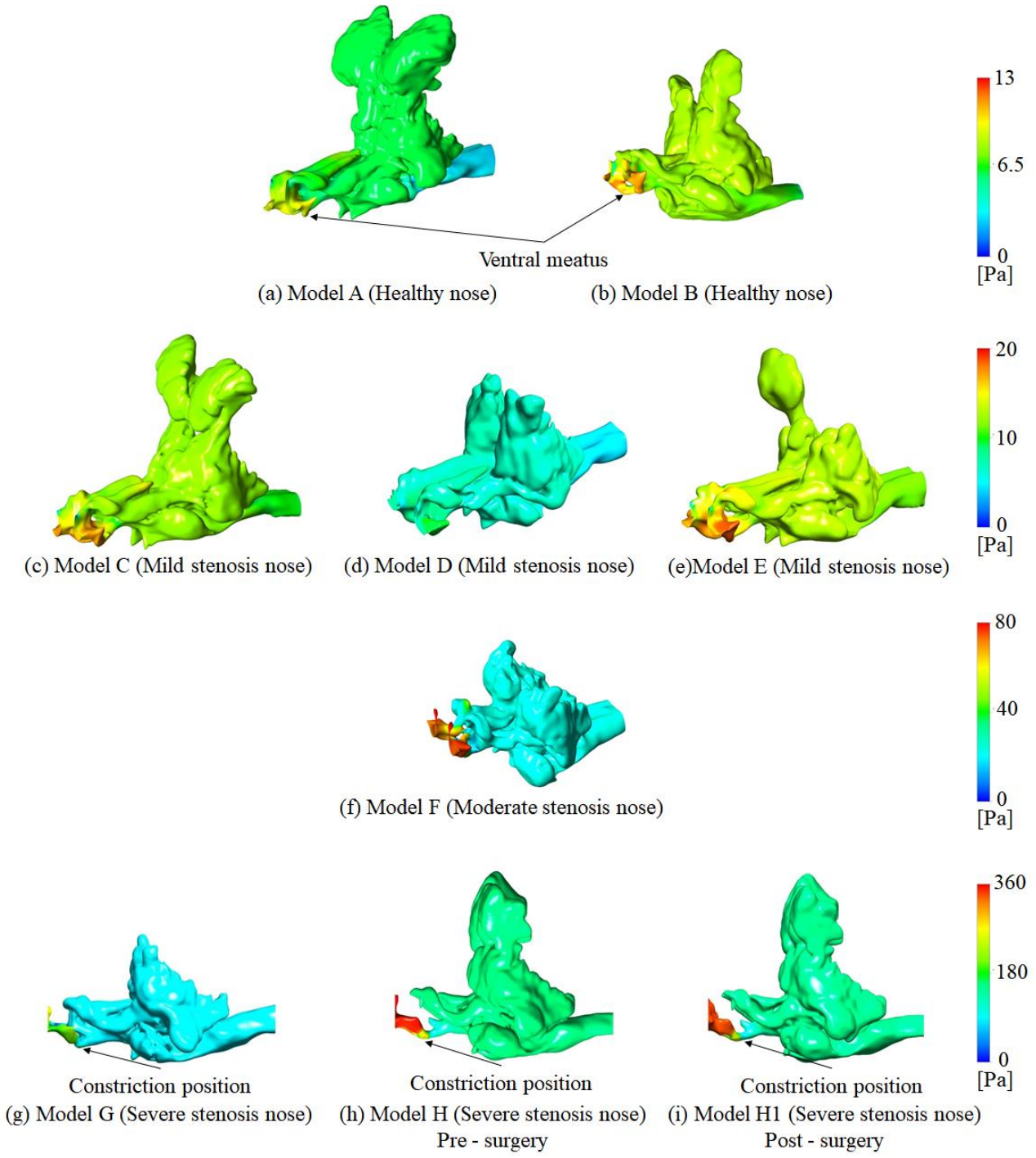

Figure 4.9: Static pressure distribution in the French bulldog upper airway models at light breathing conditions. The contours represent the static pressure distributing on the upper airway wall of healthy to severe stenosis bulldogs.

4.4.4. Calculations of pressure drop and airflow resistance

The pressure drop and airflow resistance in the eight French bulldog models (model A-H) and one postoperative model (model H1) are shown in Figs 4.10a-b. The transparent and solid symbols represent light and moderate breathing conditions, respectively. The pressure drop was calculated as the mean static pressure difference between the nostril inlet and the airway models' outlet, while the airflow resistance was defined as the pressure drop divided by the inlet flow rate. The pressure drop of the open and mild stenosis cases (models A–E) was relatively low, ranging from 3.4 – 5.1 Pa for light breathing and 15.8 – 20.5 Pa for moderate breathing conditions. The mean pressure drop increased significantly to approximately 51 Pa for the moderate stenosis (model F) and to 147.5 Pa (model G) and peaking at 195.6 Pa (model H) for the severe stenosis under light breathing.

For the moderate breathing flow rate, the pressure drop increased further for the moderate and severe stenosis cases, at 178, 483, and 651 Pa in models F, G, and H, respectively. After the surgical intervention (model H1), the pressure drop was reduced from model H, by approximately 3.7% and 0.3% in light and moderate breathing conditions. The airflow resistance, the best-quantified parameter for airway obstruction (Hoffman 2007), was calculated for all models. The airflow resistance profiles among the models were dependent on the pressure drop profiles (Fig 4.10b), and therefore both profiles shared similar trends. For example, extremely high airflow resistance was observed for moderate and severe stenosis. The resistance values between light and moderate breathing were closer than the pressure values, owing to the normalization of the inlet flow rates. The nasal cavity has been reported to account for most of the total airway resistance (Ohnishi & Ogura 1969); thus, nasal obstruction exacerbates airflow resistance in the nasal passages. This excessive increase in airflow resistance often manifests as respiratory noise, with the magnitude varying according to the obstruction's severity (Packer et al. 2012). As expected, the airflow resistance of bulldogs with moderate and severe stenosis was much higher than the healthy or mild stenosis cases. The simulation results showed that the postoperative model involving exclusive wedge resection (model H1) had a slight effect on reducing the airflow resistance. These

results imply that the simple widening of the external nostril partially contributed to the decrease of airflow resistance, but this reduction was insufficient to improve airflow resistance compared to healthy bulldogs.

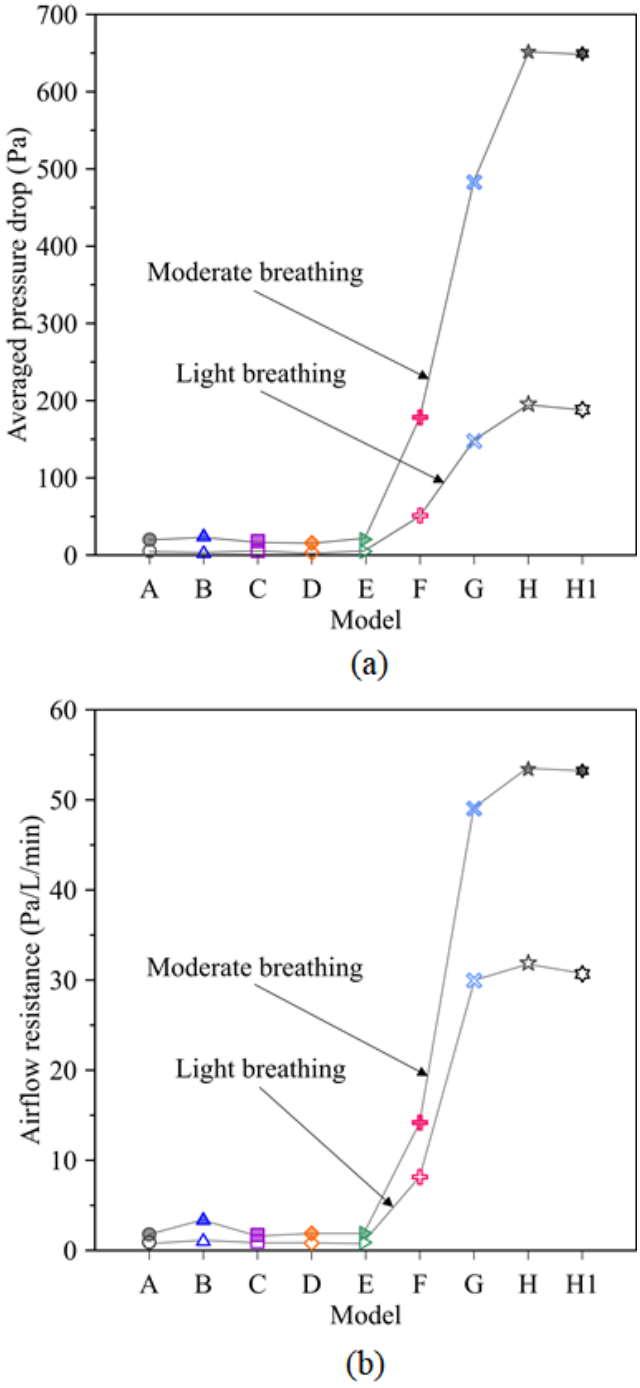

Figure 4.10: Comparison of the (a) averaged pressure drop and (b) airflow resistance between the nine bulldog upper airway models (labeled A to H, and H1 along the *x*-axis) for light and moderate breathing conditions. The pressure drop was calculated by the difference in average static pressure of transverse planes at the nostril inlet and outlet of individual bulldogs. The airflow resistance was defined by the ratio between the pressure drop and the inlet flow rates of each bulldog.

4.4.5. Distributions of wall shear stress in the upper airways of French bulldogs

Excessive turbulent shear stress on the airway wall may damage epithelial cells during airway collapse and reopening (Bilek et al. 2003). Therefore, it was essential to quantify the wall shear stress (WSS) during respiration, especially in moderate and severe stenosis cases. This may be challenging to achieve with experiments; thus, the application of CFD in this context can facilitate a deeper understanding of WSS profiles in the upper airways of bulldogs.

The wall shear stress (WSS) distribution on the airway wall surface is given in Fig 4.11, under light breathing conditions, where the high and low WSS values are indicated by red and white, respectively. The WSS describes the tangential shearing force exerted on the walls by the inhaled airflow; therefore, high WSS coincided with high velocities depicted by streamlines in Figs 4.5 and 4.6. In healthy bulldogs or those with mild stenosis, the WSS was mainly detected in the external nares region and was negligible in the nasopharynx region. Maximum WSS values in models A–E were <1.0 Pa during light breathing and 3.50 Pa for moderate breathing conditions (Table 4.5). From the results, the low WSS was recorded in healthy and mild stenosis bulldogs. As revealed in the previous research work, the existence of low-level WSS ranging from 0.1-1 Pa in mouse airways and cell cultures of humans might enhance the epithelial barrier function with an increase in intracellular calcium and activate the transient receptor potential vanilloid (TRPV) 4 and L-type voltage-gated calcium channel (VGCC) (Sidhaye et al. 2008). To our knowledge, the effect of low WSS values has not been thoroughly investigated in dogs; therefore, the impact of low WSS profiles on epithelial cells should be investigated. Although low-level WSS showed no profound effects on French bulldogs who were healthy and those with mild stenosis, owners should pay attention when their bulldogs perform moderate or intense activities.

For the moderate stenosis (model F) case, the maximum WSS was 4.82 Pa at the constriction sites in the external nares region during light breathing and 13.65 Pa during moderate breathing (Table 4.5). Apart from the external nares region, the WSS was negligible in the posterior regions (Fig 4.11f). Similarly, for the severe stenosis cases, maximum WSS was observed at the locally constricted passages where jet-

like flows developed (Figs 4.11g-h). The maximum WSS values were over 2-fold higher than those in the moderate stenosis cases (9.91-11.01 and 28.51-40.82 Pa for light and moderate breathing, see Table 4.5. The results confirm that the extremely high WSS was observed at the obstruction sites in the French bulldogs with moderate and severe stenosis, even under light breathing conditions; thus, it may exert the epithelial cells damage and inflammation.

Table 4.5. Maximum wall shear stresses in the upper airways of French bulldogs during light and moderate breathing conditions

Model	Maximum wall shear stress (Pa)	
	Light breathing condition	**Moderate breathing condition**
A	0.52	1.89
B	0.77	3.33
C	0.73	3.44
D	0.49	2.87
E	0.88	3.49
F	4.82	13.65
G	11.01	40.82
H	9.91	28.51
H1	10.07	30.37

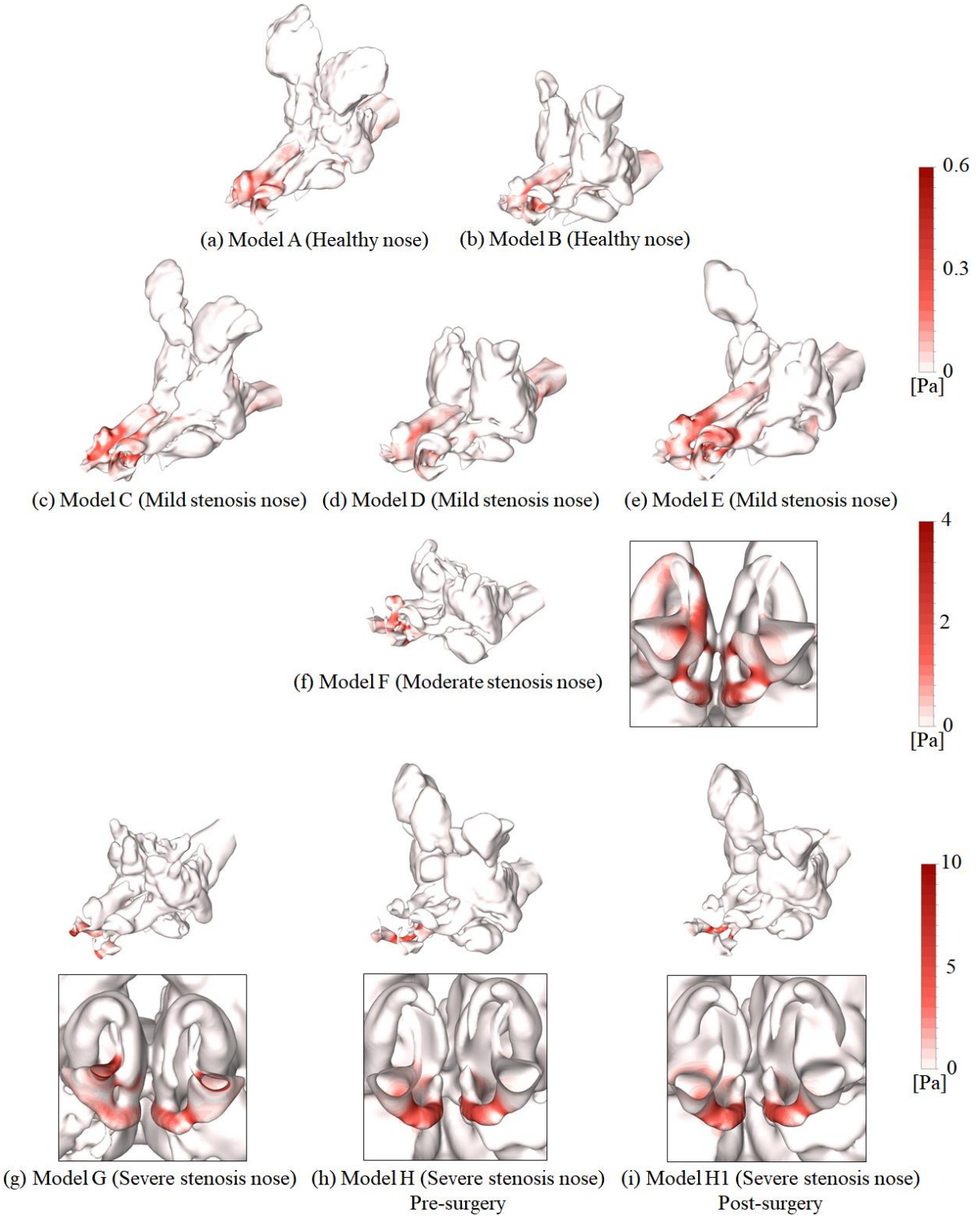

Figure 4.11: Wall shear stress (WSS) distribution contours in the nine bulldog upper airways at light breathing conditions. The location of maximum WSS of moderate and severe stenosis is shown in the front view.

The WSS was homogeneously distributed in the postoperative case compared to the preoperative case due to the similar airflow distributions at the congested position, as discussed above (Fig 4.6). Peak WSS was higher in the postoperative case than the preoperative case for both breathing conditions (Table 4.5). The effects of surgery led to different airflow profiles in the nostril inlet region of the pre-and postoperative models, and therefore, different WSS profiles were observed at this location (Fig 4.12). The WSS profile along the perimeter of cross-section plane 1 was plotted against a normalized distance for the two models (Figs 4.12b-c). The dashed line denotes the WSS profile in the preoperative case, while the solid line represents the postoperative. The WSS profile in the preoperative model fluctuated significantly compared to that postoperative model. The WSS magnitude decreased markedly after the surgical intervention. Peak WSS at this location occurred at points C1 and C'1 in the right nostril and C2 and B'2 in the left nostril (Figs 4.12b-c). Moreover, the WSS level was higher in the right nostril than in the left nostril for both pre-and postoperative cases. The surgical intervention showed promising effects in reducing high WSS in the surgical region that can mitigate the damage to epithelial cells in this region. However, it seems to be insufficient for attenuating the high WSS occurring at the constricted sites. Therefore, locally obstructed sites are the primary causes of high WSS production in the upper airway. The adverse impact of high WSS on epithelial cells of French bulldogs should be accounted for in future studies.

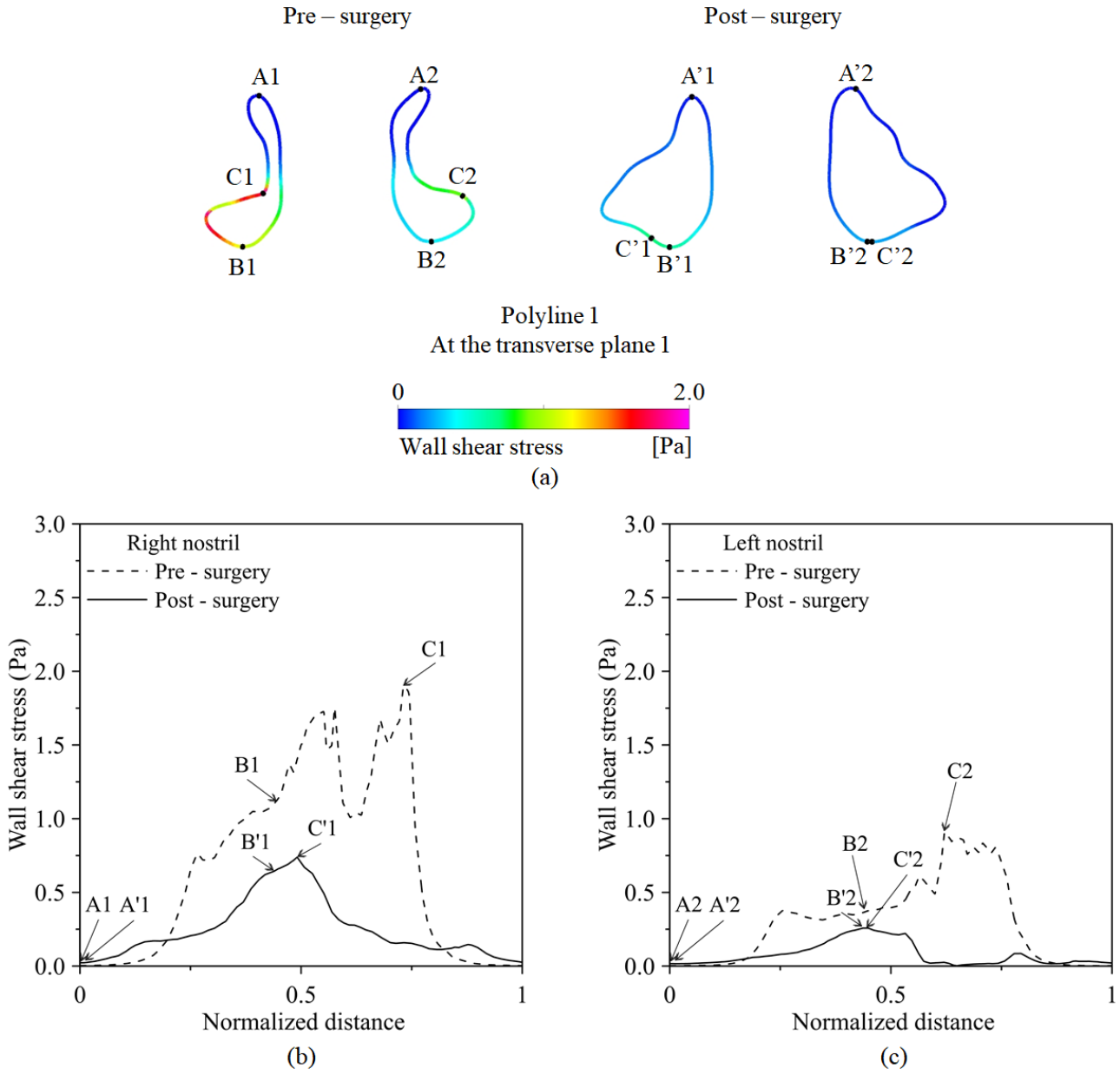

Figure 4.12: Distribution of the wall shear stress at the nostril inlet pre and postoperative at light breathing condition. (a) The wall shear stress profile was extracted from the perimeter of the left and right nostrils at plane-1. The perimeter length was normalized by the distance between data points which started from point A1, A'1 in the right nostril (b), and A2, A'2 in the left nostril (c).

Chapter 4: Numerical comparison of breathing function in nostril stenosis French bulldog and an examination of the efficacy of rhinoplasty

---

The previous published paper related to this chapter

Dang Khoa N, Lu Phuong N, Tani K, Inthavong K, Ito K. 2021. Computational fluid dynamics comparison of impaired breathing function in French bulldogs with nostril stenosis and an examination of the efficacy of rhinoplasty. Comput Biol Med [Internet]. 134(February):104398. https://doi.org/10.1016/j.compbiomed.2021.104398

CHAPTER 5
CONCLUSIONS AND RECOMMENDATIONS FOR FUTURE WORK

5.1. CONCLUSIONS

The main discussion in this thesis relates to airflow characteristics and ultrafine particle transportation/deposition in human and monkey airways under different breathing conditions; and the impaired breathing function and the efficacy of surgery in the upper airway of BOAS-related French bulldogs with different nostril stenosis levels. The task covered herein only focused on the simulation work by applying the *in silico*-based CFD method.

The CFD technique has successfully characterized the airflow distribution, total deposition fraction, and regional deposition fraction of ultrafine particles in the monkey and human airway models. The Eulerian approach was used to simulate the fluid flow and the Lagrangian was applied to track the ultrafine particle trajectories and deposition. The simulation results showed the quantitative and qualitative similarities and discrepancies in the airflow distribution between both species. The numerical deposition results were concurrent with the *in vivo* and *in vitro* measurements, as a shred of evidence for the high accuracy of the CFD method. The acceleration of ultrafine particles was confirmed that significantly relies on the involvement of Brownian motion, which reflects that the primary deposition mechanism of ultrafine particles is Brownian motion. The CFD technique quantitatively elucidated the total deposition in human and monkey airways; expressly, the deposition results indicated that the highest deposition fraction was associated with the particles of size 5 nm in both airway models. Also, the deposition fraction of the more diffusive particles (< 25 nm in diameter) in the monkey airway model was much higher than in the human airway model. To promote the extrapolation from monkey to human, the modified parameters have been developed that show the proficiency in converging the deposition fractions of both models into a single curve. The application of the CFD method better assists the toxicology studies by clearly exhibiting the hot-spot of ultrafine particles in the airway system, which

has been limited by means of experimental works. The CFD results showed that the deposition sites of ultrafine particles have been demonstrated, revealing the dominant sites in the vestibule and the valve and the nasal turbinate region of the monkey and human airway, respectively. These results imply that the epithelium lesion is more likely to occur in the anterior part of the upper respiratory tract, and the deposited particles in this region are possibly drained via the blood veins that travel to other organs and the central nervous system after a period of time. In taking full advantage of the CFD method, not only for the ultrafine particles, the filtration mechanism of human and monkey airways responding to a wide range of particle size could be described. At either high diffusive particles (< 25 nm in diameter) or high inertial particles (> 2.5 μm in diameter), the upper airway is adversely affected by the toxic substances; meanwhile, the lower airway is the main susceptible region for the particles in the remaining size range. Within these obtained results, the application of the CFD technique in the field of human and mammalian toxicology studies is feasible and reliable.

Besides, by coupling the medical imaging process and CFD method, the decline in respiratory function of BOAS-affected French bulldogs was quantitatively and qualitatively demonstrated, which may not be achievable by experiment. As a prerequisite of the CFD process, the 3D numerical reconstruction of investigated models proceeded for healthy and patient French bulldogs. The medical imaging process, which transforms the respiratory morphometric structures from 2D to 3D, provided clear and specific observations of geometric features of the serious airway malformation in moderately and severely BOAS-affected bulldogs compared with mild stenosis and healthy bulldogs. Furthermore, the 3D numerical models are accessible for casual readers, who are not specialized in reading medical images as a radiologist. Moreover, the reconstruction of deformed airways associated with the external nostril shape could offer the bulldog’s owners an ability to detect their dogs' health status by only physically observing the external nostril shape.

The CFD simulation was performed in the 3D reconstructed airway models of patients and healthy French bulldogs to describe the airflow patterns and calculate the airflow resistance. The CFD results

indicated that the airflow characteristics between healthy and mild stenosis bulldogs were trivially different compared to each other, obviating the need for surgical intervention. However, the results of airflow distribution and airflow resistance analysis indicated the urgent need for medical intervention in dogs with severe stenosis. The quantitative airflow resistance obtained by the CFD method confirmed the labored breathing in moderate and severe stenosis bulldogs under the light breathing conditions, and it became worse when these dogs breathe moderately. The CT-based CFD method also examined an improvement of recent surgery in a patient bulldog, which was still ambiguous until now. From the comparison between pre-and postoperative, the rhinoplasty successfully improved the ventilation in the external nares region; however, postoperative total airflow acceleration and airflow resistance were still high compared to healthy cases. As can be seen, the use of the CFD technique is extensive in all fields, and the veterinary field is no exception. The results from this study facilitate surgery pre-planning and offer a promising monitoring tool for bulldogs for surgeons, and deliver awareness to the bulldog's owners about the riskiness of BOAS disease and the simple technique to detect it as early stage.

5.2. RECOMMENDATIONS FOR FUTURE WORK

The use of the CFD method in predicting the behavior of an ultrafine particle in human and monkey airways delivered a high accuracy. Therefore, this technique needs to be applied to predict the behavior of non-spherical particles in the human airway (asbestos fiber, carbon fiber,…). Furthermore, the virus-laden droplets coupling with unsteady simulation should be conducted to investigate the cross-infection risks between an infected and susceptible person.

The CFD results obtained in this thesis stated the low efficacy of rhinoplasty in definitely treating the clinical signs of BOAS-affected French bulldogs. Therefore, further investigation, i.e., virtual surgery, needs to be taken into account to offer the surgical scenarios that can better improve patient dogs. Besides, the air-conditioning function also needs to be examined and improved in the upper airway of patient bulldogs. Further studies may also involve the simulation under transient flow, which can elucidate the impaired breathing function in a more realistic form.

REFERENCES

Abe K, Kondoh T, Nagano Y. 1994. A new turbulence model for predicting fluid flow and heat transfer in separating and reattaching Flow field calculations. Int J Heat Mass Transf. 37(1):139–151.

Abe K, Kondoh T, Nagano Y. 1995. A new turbulence model for predicting fluid flow and heat transfer in separating and reattaching flows-II. Thermal field calculations. Int J Heat Mass Transf. 38(8):1467–1481.

Anjilvel S, Asgharian B. 1995. A multiple-path model of particle deposition in the rat lung. Toxicol Sci. 28(1):41–50.

Aron DN, Crowe DT. 1985. Upper airway obstruction. General principles and selected conditions in the dog and cat. Vet Clin North Am Small Anim Pract. 15(5):891–917.

Asgharian B, Hofmann W, Bergmann R. 2001. Particle deposition in a multiple-path model of the human lung. Aerosol Sci Technol. 34(4):332–339.

Asgharian B, Price O, McClellan G, Corley R, Einstein DR, Jacob RE, Harkema J, Carey SA, Schelegle E, Hyde D, et al. 2012. Development of a rhesus monkey lung geometry model and application to particle deposition in comparison to humans. Inhal Toxicol. 24(13):869–899.

Asgharian B, Price OT, Oldham M, Chen LC, Saunders EL, Gordon T, Mikheev VB, Minard KR, Teeguarden JG. 2014. Computational modeling of nanoscale and microscale particle deposition, retention and dosimetry in the mouse respiratory tract. Inhal Toxicol. 26(14):829–842.

Asher L, Diesel G, Summers JF, McGreevy PD, Collins LM. 2009. Inherited defects in pedigree dogs. Part 1: Disorders related to breed standards. Vet J. 182(3):402–411.

Bakhtiary M. 2014. Medical Imaging Technology (Springer Briefs in Physics). [place unknown].

Bernaerts F, Talavera J, Leemans J, Hamaide A, Claeys S, Kirschvink N, Clercx C. 2010. Description of original endoscopic findings and respiratory functional assessment using barometric whole-body plethysmography in dogs suffering from brachycephalic airway obstruction syndrome. Vet J. 183(1):95–102.

Bilek AM, Dee KC, Gaver DP. 2003. Mechanisms of surface-tension-induced epithelial cell damage in a model of pulmonary airway reopening. J Appl Physiol. 94(2):770–783.

Calderón-Garcidueña L, Maronpot RR, Torres-Jardon R, Henríquez-Roldán C, Schoonhoven R, Acuña-Ayala H, Villarreal-Calderón A, Nakamura J, Fernando R, Reed W, et al. 2003. DNA Damage in Nasal

and Brain Tissues of Canines Exposed to Air Pollutants Is Associated with Evidence of Chronic Brain Inflammation and Neurodegeneration. Toxicol Pathol. 31(5):524–538.

Cheng KH, Cheng YS, Yeh HC, Swift DL. 1995. Deposition of ultrafine aerosols in the head airways during natural breathing and during simulated breath holding using replicate human upper airway casts. Aerosol Sci Technol. 23(3):465–474.

Cheng YS. 2003. Aerosol deposition in the extrathoracic region. Aerosol Sci Technol. 37(8):659–671.

Cheng YS, Irshad H, Kuehl P, Holmes TD, Sherwood R, Hobbs CH. 2008. Lung deposition of droplet aerosols in monkeys. Inhal Toxicol. 20(11):1029–1036.

Cheng YS, Yeh HC, Guilmette RA, Simpson SQ, Cheng KH, Swift DL. 1996. Nasal Deposition of Ultrafine Particles in Human Volunteers and Its Relationship to Airway Geometry. Aerosol Sci Technol. 25(3):274–291.

Craven BA, Paterson EG, Settles GS. 2010. The Fluid Dynamics of Canine Olfaction: A New Explanation for Macrosmia. J R Soc Interface. 7:933–943.

Díaz D del O, Hinz DF. 2015. Performance of eddy-viscosity turbulence models for predicting swirling pipe-flow: Simulations and laser-Doppler velocimetry. arXiv Fluid Dyn [Internet]. http://arxiv.org/abs/1507.04648

Doi K. 2006. Diagnostic imaging over the last 50 years: Research and development in medical imaging science and technology. Phys Med Biol. 51(13).

Donaldson K, Li XY, MacNee W. 1998. Ultrafine (nanometre) particle mediated lung injury. J Aerosol Sci. 29(5–6):553–560.

Dong J, Shang Y, Inthavong K, Chan HK, Tu J. 2018. Partitioning of dispersed nanoparticles in a realistic nasal passage for targeted drug delivery. Int J Pharm. 543(1–2):83–95.

Doorly DJ, Taylor DJ, Schroter RC. 2008. Mechanics of airflow in the human nasal airways. Respir Physiol Neurobiol. 163(1–3):100–10.

Dosimetry C, Panel H, Affecting DA, Estimates RR, Isbn C, Pdf T, Press NA, Press NA, Academy N, Academy N, Press NA. 1991. Comparative Dosimetry of Radon in Mines and Homes. [place unknown].

Dougherty G. 2009. Digital image processing for medical applications. New York: Cambridge University Press.

Dupré G, Heidenreich D. 2016. Brachycephalic Syndrome. Vet Clin North Am - Small Anim Pract. 46(4):691–707.

Ellison GW. 2004. Alapexy: An alternative technique for repair of stenotic nares in dogs. J Am Anim

Hosp Assoc. 40(6):484–489.

Emmerson T. 2014. Brachycephalic obstructive airway syndrome: A growing problem. J Small Anim Pract. 55(11):543–544.

Fasanella FJ, Shivley JM, Wardlaw JL, Givaruangsawat S. 2010. Brachycephalic airway obstructive syndrome in dogs: 90 Cases (1991-2008). J Am Vet Med Assoc. 237(9):1048–1051.

Fedorov A, Beichel R, Kalpathy-Cramer J, Finet J, Fillion-Robin JC, Pujol S, Bauer C, Jennings D, Fennessy F, Sonka M, et al. 2012. 3D Slicer as an image computing platform for the Quantitative Imaging Network. Magn Reson Imaging [Internet]. 30(9):1323–1341. http://dx.doi.org/10.1016/j.mri.2012.05.001

Fernández-Parra R, Pey P, Zilberstein L, Malvè M. 2019. Use of computational fluid dynamics to compare upper airway pressures and airflow resistance in brachycephalic, mesocephalic, and dolichocephalic dogs. Vet J. 253.

Frampton MW. 2001. Systemic and cardiovascular effects of airway injury and inflammation: Ultrafine particle exposure in humans. Environ Health Perspect. 109(SUPPL. 4):529–532.

Ge QJ, Inthavong K, Tu JY. 2012. Local deposition fractions of ultrafine particles in a human nasal-sinus cavity CFD model. Inhal Toxicol. 24(8):492–505.

Guytons AC. 1947. Measurement of the respiratory volume of laboratory animals. Am J Physiol.(150):70–77.

Haimel G, Dupré G. 2015. Brachycephalic airway syndrome: A comparative study between pugs and French bulldogs. J Small Anim Pract. 56(12):714–719.

Harkema JR, Plopper CG, Hyde DM, St George JA, Dungworth DL. 1987. Effects of an ambient level of ozone on primate nasal epithelial mucosubstances: quantitative histochemistry. Am J Pathol. 127(1):90–96.

Harvey CE. 1989. Inherited and congenital airway conditions. J Small Anim Pract. 30(3):184–187.

Hendricks JC. 1992. Brachycephalic airway syndrome. Vet Clin North Am - Small Anim Pract. 22(5):1145–1153.

Hinds WC. 1999. Aerosol technology : properties, behavior, and measurement of airborne particles. New York: Wiley.

Hoffman AM. 2007. Airway Physiology and Clinical Function Testing. Vet Clin North Am - Small Anim Pract. 37(5):829–843.

Hopkins LE, Patchin ES, Chiu PL, Brandenberger C, Smiley-Jewell S, Pinkerton KE. 2014. Nose-to-

brain transport of aerosolised quantum dots following acute exposure. Nanotoxicology [Internet]. 8(8):885–893. http://dx.doi.org/10.3109/17435390.2013.842267

Hostnik ET, Scansen BA, Zielinski R, Ghadiali SN. 2017. Quantification of nasal airflow resistance in English bulldogs using computed tomography and computational fluid dynamics. Vet Radiol Ultrasound. 58(5):542–551.

Inthavong K, Ge QJ, Li X, Tu JY. 2013. Source and trajectories of inhaled particles from a surrounding environment and its deposition in the respiratory airway. Inhal Toxicol. 25(5):280–291.

Ito K. 2014. Integrated numerical approach of computational fluid dynamics and epidemiological model for multi-scale transmission analysis in indoor spaces. Indoor Built Environ. 23(7):1029–1049.

Ito K, Inthavong K, Kurabuchi T, Ueda T, Endo T, Omori T, Ono H, Kato S, Sakai K, Suwa Y, et al. 2015a. CFD Benchmark Tests for Indoor Environmental Problems: Part 1 Isothermal/Non-Isothermal Flow in 2D and 3D Room Model. Int J Archit Eng Technol. 2(1):01–22.

Ito K, Inthavong K, Kurabuchi T, Ueda T, Endo T, Omori T, Ono H, Kato S, Sakai K, Suwa Y, et al. 2015b. CFD Benchmark Tests for Indoor Environmental Problems: Part 2 Cross-Ventilation Airflows and Floor Heating Systems. Int J Archit Eng Technol. 2(1):23–49.

Ito K, Inthavong K, Kurabuchi T, Ueda T, Endo T, Omori T, Ono H, Kato S, Sakai K, Suwa Y, et al. 2015c. CFD Benchmark Tests for Indoor Environmental Problems: Part 3 Numerical Thermal Manikins. Int J Archit Eng Technol. 2(1):50–75.

Ito K, Mitsumune K, Kuga K, Phuong NL, Tani K, Inthavong K. 2017. Prediction of convective heat transfer coefficients for the upper respiratory tracts of rat, dog, monkey, and humans. Indoor Built Environ. 26(6):828–840.

Kelly JT, Asgharian B, Kimbell JS, Wong BA. 2004. Particle Deposition in Human Nasal Airway Replicas Manufactured by Different Methods. Part II: Ultrafine Particles. Aerosol Sci Technol. 38(11):1072–1079.

Kelly JT, Asgharian B, Wong BA. 2005. Inertial particle deposition in a monkey nasal mold compared with that in human nasal replicas. Inhal Toxicol. 17(14):823–830.

Kim JW, Phuong NL, Aramaki S ichiro, Ito K. 2018. Flow visualization through particle image velocimetry in realistic model of rhesus monkey's upper airway. Respir Physiol Neurobiol [Internet]. 251(January):16–27. https://doi.org/10.1016/j.resp.2018.02.007

Kurt OK, Zhang J, Pinkerton K. 2016. Pulmonary Health Effects of Air Pollution. Curr Opin Pulm Med [Internet]. 22(2):139–143. file:///C:/Users/Carla Carolina/Desktop/Artigos para acrescentar na qualificação/The impact of birth weight on cardiovascular disease risk in the.pdf

Ladlow J, Liu NC, Kalmar L, Sargan D. 2018. Brachycephalic obstructive airway syndrome. Vet Rec. 182(13):375–378.

Liu NC, Sargan DR, Adams VJ, Ladlow JF. 2015. Characterisation of brachycephalic obstructive airway syndrome in French bulldogs using whole-body barometric plethysmography. PLoS One [Internet]. 10(6). http://dx.doi.org/10.1371/journal.pone.0130741

Liu NC, Troconis EL, Kalmar L, Price DJ, Wright HE, Adams VJ, Sargan DR, Ladlow JF. 2017. Conformational risk factors of brachycephalic obstructive airway syndrome (BOAS) in pugs, French bulldogs, and bulldogs. PLoS One. 12(8):1–24.

Lodato DL, Hedlund CS. 2012a. Brachycephalic airway syndrome: Pathophysiology and diagnosis. Compend Contin Educ Vet. 34(7):3–7.

Lodato DL, Hedlund CS. 2012b. Brachycephalic Airway Syndrome: management. Compend Contin Educ Vet. 34(8):167–183.

Longest PW, Xi J. 2007. Computational investigation of particle inertia effects on submicron aerosol deposition in the respiratory tract. J Aerosol Sci. 38(1):111–130.

Manisalidis I, Stavropoulou E, Stavropoulos A, Bezirtzoglou E. 2020. Environmental and Health Impacts of Air Pollution: A Review. Front Public Heal. 8(February):1–13.

Manojkumar N, Srimuruganandam B, Shiva Nagendra SM. 2019. Application of multiple-path particle dosimetry model for quantifying age specified deposition of particulate matter in human airway. Ecotoxicol Environ Saf [Internet]. 168(July 2018):241–248. https://doi.org/10.1016/j.ecoenv.2018.10.091

Martonen TB, Katz IM, Musante C. 2001. A Nonhuman Primate Aerosol Deposition Model for Toxicological and Pharmaceutical Studies. Inhal Toxicol. 13(4):307–356.

Meola SD. 2013. Brachycephalic Airway Syndrome. Top Companion Anim Med. 28(3):91–96.

Michell AR. 1999. Longevity of British breeds of dog and its relationships with sex, size, cardiovascular variables and disease. Vet Rec. 145(22):625–629.

Mildenberger P, Eichelberg M, Martin E. 2002. Introduction to the DICOM standard. Eur Radiol. 12(4):920–927.

Morgan KT, Kimbell JS, Monticello TM, Patra AL, Fleishman A. 1991. Studies of inspiratory airflow patterns in the nasal passages of the F344 rat and rhesus monkey using nasal molds: Relevance to formaldehyde toxicity. Toxicol Appl Pharmacol. 110(2):223–240.

Mujika KM, Méndez JAJ, de Miguel AF. 2018. Advantages and Disadvantages in Image Processing

with Free Software in Radiology. J Med Syst. 42(3):1–7.

Mullen NA, Liu C, Zhang Y, Wang S, Nazaroff WW. 2011. Ultrafine particle concentrations and exposures in four high-rise beijing apartments. Atmos Environ. 45(40):7574–7582.

Mutlu Z, Demİrutku A, Li MKĞ. 2015. Brachycephalic Airway Syndrome in Dogs Brachycephalic Airway Syndrome in Dogs K ö peklerde Brahisefalik Hava Y olu Sendromu. (September).

Nikić D, Stanković A. 2005. Air pollution as a risk factor for lung cancer. Arch Oncol. 13(2):79–82.

O'Neill DG, Church DB, McGreevy PD, Thomson PC, Brodbelt DC. 2013. Longevity and mortality of owned dogs in England. Vet J. 198(3):638–643.

O'Neill DG, Jackson C, Guy JH, Church DB, McGreevy PD, Thomson PC, Brodbelt DC. 2015. Epidemiological associations between brachycephaly and upper respiratory tract disorders in dogs attending veterinary practices in England. Canine Genet Epidemiol. 2(1):1–10.

Oberdörster G, Sharp Z, Atudorei V, Elder A, Gelein R, Kreyling W, Cox C. 2004. Translocation of inhaled ultrafine particles to the brain. Inhal Toxicol. 16(6–7):437–445.

Ohnishi T, Ogura JH. 1969. Partitioning of pulmonary resistance in the dog. Laryngoscope. 79(11):1847–1878.

Packer RMA, Hendricks A, Burn CC. 2012. Do dog owners perceive the clinical signs related to conformational inherited disorders as "normal" for the breed? A potential constraint to improving canine welfare. Anim Welf. 21(SUPPL. 1):81–93.

Packer RMA, Hendricks A, Tivers MS, Burn CC. 2015. Impact of facial conformation on canine health: Brachycephalic obstructive airway syndrome. PLoS One. 10(10):1–21.

Pardali D, Rallis TS, Raptopoulos D, Gioulekas D. 2010. Tidal Breathing Flow-Volume Loop Analysis for the Diagnosis and Staging of Tracheal Collapse in Dogs. J Vet Intern Med. 24:832–842.

Phuong N, Khoa N, Inthavong K, Ito K. 2019. Particle and inhalation exposure in human and monkey computational airway models. Inhal Toxicol.

Phuong NL, Ito K. 2013. Experimental and numerical study of airflow pattern and particle dispersion in a vertical ventilation duct. Build Environ. 59:466–481.

Phuong NL, Ito K. 2015. Investigation of flow pattern in upper human airway including oral and nasal inhalation by PIV and CFD. Build Environ [Internet]. 94:504–515. http://dx.doi.org/10.1016/j.buildenv.2015.10.002

Phuong NL, Quang T Van, Khoa ND, Kim JW, Ito K. 2020. CFD analysis of the flow structure in a monkey upper airway validated by PIV experiments. Respir Physiol Neurobiol. 271(September

2019):103304.

Poncet CM, Dupre GP, Freiche VG, Estrada MM, Poubanne YA, Bouvy BM. 2005. Prevalence of gastrointestinal tract lesions in 73 brachycephalic dogs with upper respiratory syndrome. J Small Anim Pract. 46(6):273–279.

Riecks TW, Birchard SJ, Stephens JA. 2007. in Dogs : 62 Cases (1991 – 2004). Javma. 230(9).

Riggs J, Liu NC, Sutton DR, Sargan D, Ladlow JF. 2019. Validation of exercise testing and laryngeal auscultation for grading brachycephalic obstructive airway syndrome in pugs, French bulldogs, and English bulldogs by using whole-body barometric plethysmography. Vet Surg. 48(4):488–496.

Roedler FS, Pohl S, Oechtering GU. 2013. How does severe brachycephaly affect dog's lives? Results of a structured preoperative owner questionnaire. Vet J. 198(3):606–610.

Rygg AD, Van Valkenburgh B, Craven BA. 2017. The influence of sniffing on airflow and odorant deposition in the canine nasal cavity. Chem Senses. 42(8):683–698.

Saha PK, Robinson ES, Shah RU, Zimmerman N, Apte JS, Robinson AL, Presto AA. 2018. Reduced Ultrafine Particle Concentration in Urban Air: Changes in Nucleation and Anthropogenic Emissions. Environ Sci Technol. 52(12):6798–6806.

Schmidt-Nielsen K, Bretz WL, Taylor CR. 1970. Panting in dogs: Unidirectional air flow over evaporative surfaces. Science (80-). 169(3950):1102–1104.

Schreider JP, Raabe OG. 1981. Anatomy of the nasal-pharyngeal airway of experimental animals. Anat Rec. 200(2):195–205.

Schroeter JD, Asgharian B, Price OT, McClellan GE. 2013. Computational fluid dynamics simulations of inhaled nano- and microparticle deposition in the rhesus monkey nasal passages. Inhal Toxicol. 25(12):691–701.

Sidhaye VK, Schweitzer KS, Caterina MJ, Shimoda L, King LS. 2008. Shear stress regulates aquaporin-5 and airway epithelial barrier function. Proc Natl Acad Sci U S A. 105(9):3345–3350.

Suetens P. 2009. Fundamentals of Medical Imaging, Second Edition. New York.

Tian L, Shang Y, Dong J, Inthavong K, Tu J. 2017. Human nasal olfactory deposition of inhaled nanoparticles at low to moderate breathing rate. J Aerosol Sci. 113:189–200.

Tu J, Inthavong K, Ahmadi G. 2013. Computational fluid and particle dynamics in the human respiratory system. New York: Springer.

Versteeg HK, Malalasekera W. 2007. An introduction to Computational Fluid Dynamics: The finite volume method. England.

Wah-Yen T, Asako Y, Azwadi N, Sidik C, Rui-Zher G. 2017. Governing Equations in Computational Fluid Dynamics: Derivations and A Recent Review. Prog Energy Environ. 1(June):1–19.

Wallace L. 1996. Indoor Particles: A Review. J Air Waste Manag Assoc. 46(2):98–126.

Wallace L. 2006. Indoor sources of ultrafine and accumulation mode particles: Size distributions, size-resolved concentrations, and source strengths. Aerosol Sci Technol. 40(5):348–360.

Wang SM, Inthavong K, Wen J, Tu JY, Xue CL. 2009. Comparison of micron- and nanoparticle deposition patterns in a realistic human nasal cavity. Respir Physiol Neurobiol. 166(3):142–151.

Waring MS, Siegel JA. 2007. An evaluation of the indoor air quality in bars before and after a smoking ban in Austin, Texas. J Expo Sci Environ Epidemiol. 17(3):260–268.

WHO. 2006. WHO Air quality guidelines for particulate matter, ozone, nitrogen dioxide and sulfur dioxide: global update 2005: summary of risk assessment.

Wiestner TS, Koch DA, Nad N, Balli A, Roos M, Weilenmann R, Michel E, Arnold S. 2007. Evalualtion of the repeatability of rhinomanometry and its use in assessing transnasal resistance and pressure in dogs. Am J Vet Res. 68(2):178–184.

William Sunderman F. J. 2001. Review: Nasal toxicity, carcinogenicity, and olfactory uptake of metals. Ann Clin Lab Sci. 31(1):3–24.

Xi J, Longest PW. 2008. Numerical predictions of submicrometer aerosol deposition in the nasal cavity using a novel drift flux approach. Int J Heat Mass Transf. 51(23–24):5562–5577.

Yeh HC, Cheng YS, Morgan KT. 1992. Deposition of radon progeny in nonhuman primate nasal airways.

Yeh HC, Muggenburg BA, Harkema JR. 1997. In vivo deposition of inhaled ultrafine particles in the respiratory tract of rhesus monkeys. Aerosol Sci Technol. 27(4):465–470.

Yoon JY, Lee JD, Joo SW, Kang DR. 2016. Indoor radon exposure and lung cancer: A review of ecological studies. Ann Occup Environ Med. 28(1):1–9.

Young MT, Sandler DP, DeRoo LA, Vedal S, Kaufman JD, London SJ. 2014. Ambient air pollution exposure and incident adult asthma in a nationwide cohort of U.S. women. Am J Respir Crit Care Med. 190(8):914–921.

Zhang Z, Kleinstreuer C. 2004. Airflow structures and nano-particle deposition in a human upper airway model. [place unknown].

Zhang Z, Kleinstreuer C. 2011. Computational analysis of airflow and nanoparticle deposition in a combined nasal–oral–tracheobronchial airway model. J Aerosol Sci. 42(3):174–194.

APPENDIX

A.1. The UDF macro defining the DPM times step for particle transportation/deposition analysis

```
#include "udf.h"
#include "dpm.h"
DEFINE_DPM_TIMESTEP(limit_to_e_minus_sixth,p, dt)
{
   if (dt > 1.e-6)
     {
/*       p->next_time_step = 1.e-6; */
   return 1.e-6;
     }

   return dt;
}
```

A.2. The UDF macro calculating the acceleration of ultrafine particles exerted by body force

```
# include "udf.h"
int n=0;
DEFINE_DPM_BODY_FORCE(particle_body_force,p,i)
{
Thread *t=P_CELL_THREAD(p);
cell_t c=P_CELL(p);
real bforce;
if(n==0) p->user[0]=0.0;
if (CURRENT_TIME>1.5*CURRENT_TIMESTEP)
{
bforce=((P_VEL(p)[1]-p->user[0])/CURRENT_TIMESTEP);
}
else
{
bforce=0.0;
}
p->user[0]=P_VEL(p)[1];
n+=1;
return bforce;
}
```